2016

Structural behaviour of FRP tube reinforced concrete (FTRC) columns

Weiqiang Wang
University of Wollongong

UNIVERSITY OF WOLLONGONG

School of Civil, Mining and Environmental Engineering

Structural Behaviour of FRP Tube Reinforced Concrete (FTRC) Columns

Weiqiang Wang

BEng, MSc

This thesis is presented as part of the requirements for the Award of the Degree of Doctor of Philosophy from the University of Wollongong

March 2016

THESIS DECLARATION

I, Weiqiang Wang, hereby declare that all material in this thesis, submitted in fulfilment of the requirements of the award of Doctor of Philosophy, in the School of Civil, Mining and Environmental Engineering, University of Wollongong, Australia, is wholly my own work unless otherwise referenced or acknowledged. This document has not been submitted for qualifications at any other academic institution.

Weiqiang Wang
March 2016

ABSTRACT

FRP tube reinforced concrete (FTRC) column is a novel hybrid concrete column proposed in this thesis. In the FTRC column, FRP tube is placed into the concrete to act as internal reinforcement of the column. Two types of FTRC columns have been investigated. Type I FTRC column is reinforced with perforated FRP tube. Type II FTRC column is reinforced with intact FRP tube, and polymer grid is embedded into the concrete cover to prevent the premature spalling of concrete cover. Both types of FTRC columns are expected to achieve excellent durability under harsh environments as well as superior performance under different loading conditions. This thesis presents experimental and theoretical investigations on the structural behaviour of the proposed FRTC column.

The first part of the research program is concerned with the behaviour of Type I FTRC column under axial compression. Different FRP tube configurations (intact tube, axially perforated tube and diagonally perforated tube) have been chosen to provide internal reinforcement of FTRC columns. The experimental results show that Type I FTRC column can obtain a considerable amount of strength and ductility under axial compression. Axially perforated tube performed better than diagonally perforated tube in improving the strength and ductility of Type I FTRC columns. Numerical simulations have also been carried out to assess the influence of tube perforations on the performance of Type I FTRC columns. In addition, the axial compressive behaviour of perforated FRP tube has been investigated. Different parameters that influence the performance of perforated FRP tube under axial compression have been investigated. Design-oriented equations have been proposed to predict the performance of perforated FRP tube under axial compression.

The second part of the research program is concerned with the behaviour of Type II FTRC column under axial compression. In addition to Type II FTRC columns, FRP confined concrete columns have also been tested for comparison. The experimental results indicate that, if properly designed, Type II FTRC columns can perform better than FRP confined concrete columns in terms of strength and ductility. Based on the test results, an analytical model has been developed. The analytical model has been verified by the test results. The model has been subsequently adopted to investigate

the influences of various parameters on the axial compressive behaviour of Type II FTRC column. In addition, the behaviour of concrete confined solely by polymer grid under axial compression has been studied. Based on the test results in this study as well as previous studies, an analytical model has been developed for the axial compressive behaviour of polymer grid confined concrete with strain-softening response.

The last part of the research program is focused on the behaviour of both types of FTRC specimens under different loading conditions. Four groups of 16 specimens have been tested under concentric, 25 mm eccentric, 50 mm eccentric, and four-point loadings. All specimens were 240 mm in diameter and 800 mm in height. In addition to FTRC specimens, specimens reinforced with longitudinal steel bars and steel helices have also been tested for comparison. Results from the experimental investigations show that FRP tubes significantly increase the load carrying capacity and ductility of FTRC specimens. Type II FTRC specimens performed better than Type I FTRC specimens as well as specimens reinforced with longitudinal steel bars and helices in terms of strength and ductility. In addition, an analytical procedure has been developed for the performance of FTRC specimens under different loading conditions. The results of the developed analytical procedure have been found to be in good agreements with the experimental results.

LIST OF PUBLICATIONS

Refereed Journal Papers:

1. Hadi, M. N. S., Wang, W., and Sheikh, M. N. (2015). "Axial compressive behaviour of GFRP tube reinforced concrete columns." *Construction and Building Materials*, 81, 198-207.
2. Wang, W., Sheikh, M. N., and Hadi, M. N. S. (2015). "Behaviour of perforated GFRP tubes under axial compression." *Thin-Walled Structures*, 95, 88-100.
3. Wang, W., Sheikh, M. N., and Hadi, M. N. S. (2015). "Axial compressive behaviour of concrete confined with polymer grid." *Materials and Structures/Materiaux et Constructions*, 1-16.
4. Wang, W., Sheikh, M. N., and Hadi, M. N. S. (2015). "Experimental study on FRP tube reinforced concrete (FTRC) columns under different loading conditions." *Journal of Composites for Construction*, ASCE, in press.
5. Wang, W., Sheikh, M. N., and Hadi, M. N. S., Gao, D., Chen, G. (2016). "Behaviour of concrete-encased concrete-filled FRP tube (CCFT) columns under axial compression." *Engineering Structures.* (Under review).

Refereed Conference Papers:

1. Wang, W., Sheikh, M. N., Hadi, M. N. S., Lyons B. Behaviour of GFRP tube reinforced concrete columns under axial compression. Proceedings of the Seventh International Conference on FRP Composites in Civil Engineering (CICE 2014), August 20-22, 2014, Vancouver, Canada.
2. Wang, W., Al-baali AQ, Sheikh, M. N., Hadi, M. N. S. Behaviour of GFRP tube reinforced concrete columns under eccentric loading. The 12th International Symposium on Fiber Reinforced Polymers for Reinforced Concrete Structures & The 5th Asia-Pacific Conference on Fiber Reinforced Polymers in Structures Joint conference, December 14-16, 2015, Nanjing, China.
3. Wang, W., Sheikh, M. N., Hadi, M. N. S. Confining concrete cover of GFRP tube reinforced concrete columns with polymer grids. The 12th International Symposium on Fiber Reinforced Polymers for Reinforced Concrete Structures & The 5th Asia-Pacific Conference on Fiber Reinforced Polymers in Structures Joint conference, December 14-16, 2015, Nanjing, China.

ACKNOWLEDGEMENTS

I wish to express my gratitude to all those who helped me during my research and gave me the possibility to complete the thesis. This thesis is the end of my PhD journey and the beginning of my further research study.

I am extremely grateful to my principle supervisor, Associate Professor Muhammad N.S. Hadi for his encouragement, thoughtful guidance and invaluable support throughout my research.

I also wish to express my sincere thanks to my co-supervisor, Dr. Neaz Sheikh, for his guidance in training me in critical thinking and academic writing, and for all his continuous advice and encouragement.

I would like to give my sincere thanks to Dr. Tao Yu and Dr. Lip Teh for their valuable discussions with me during my research.

I am also very grateful to all the technical staff at the High Bay Civil Engineering Laboratory at the University of Wollongong, especially Messrs Ritchie Mclean, Alan Grant, Colin Devinish, and Fernando Escribano, for their support and assistance during the experimental program.

I am grateful to the University of Wollongong and the China Scholarship Council for supporting my PhD scholarship, without the scholarship I wouldn't have the opportunity to start my PhD study.

Last but not the least, I give my heartfelt thanks to my parents, for their everlasting love, support and unconditional trust. I also wish to express my gratitude to my wife for her understanding and continuous encouragement. They are the persons to whom this thesis is dedicated.

TABLE OF CONTENTS

LIST OF FIGURES

LIST OF TABLES

ABBREVIATIONS

a	shear span
A_{cover}	cross sectional area of concrete cover
A_f	cross sectional area of FRP tube
A_g	cross sectional area of polymer grid
A_{ic}	cross sectional area of inner concrete
A_{ls}	cross sectional area of longitudinal steel bars
A_{oc}	cross section area of outer confined concrete
A_{ts}	cross section area of transverse steel bars
b_g	width of transverse polymer grid
C_j	confinement modulus
d	hole diameter
d_g	diameter of tubular polymer grid
d_s	diameter of steel helices
D	diameter of confined concrete
D_i	inner diameter of FRP tube
D_o	outer diameter of FRP tube
e	eccentricity
E_2	slope of the linear second portion of the stress-strain curve of FRP confined concrete under concentric compression
E_{2ec}	slope of the second linear portion of the concrete stress-strain curve of FRP confined concrete to the load eccentricity e
E_c	elastic modulus of concrete
$E_{f,l}$	longitudinal compressive elastic modulus of FRP tube
$E_{f,t}$	transverse tensile modulus of FRP tube
E_s	elastic modulus of longitudinal bars
f'_{cc}	peak axial stress of confined concrete
f'^{*}_{cc}	peak axial stress of concrete under a specific constant confining pressure σ_R
$\overline{f}_{cc}$	ultimate compressive strength of concrete for a given eccentricity e

f_{cco}	axial compressive stress of unconfined concrete corresponding to ε_{cco}
$f_{co}^{'}$	peak axial stress of unconfined concrete
$f_{l,c}$	longitudinal compressive strength of FRP tube
$f_{l,t}$	longitudinal tensile strength of FRP tube
$f_{lu,a}$	actual lateral confining pressure at ε_{cu}
f_o	intercept of the stress axis by the linear second portion of the stress-strain curve of FRP confined concrete
$f_{t,c}$	transverse compressive strength of FRP tube
$f_{t,t}$	transverse tensile strength of FRP tube
f_{yh}	yield strength of transverse bars
f_{yl}	yield strength of longitudinal bars
I	area of moment of inertia of FRP tube
k_f	axial stiffness of FRP tube
k_s	axial stiffness of longitudinal bars
k_e	confinement effective coefficient
M_{cfst}	bending moment carried by the CFST component in concrete-encased CFST column
M_y	bending moment at the maximum load before cover spalling in FTRC column
$M_{y,CFFTs}$	bending moment carried by the inner CFFTs at the maximum load before cover spalling in FTRC column
$M_{y,cover}$	bending moment carried by the concrete cover at the maximum load before cover spalling P_y in FTRC column
M_u	bending moment at ultimate load
$M_{u,CFFTs}$	bending moment carried by the inner CFFTs at ultimate load in FTRC column
$M_{u,cover}$	bending moment carried by the concrete cover at ultimate load in FTRC column
N_{cfst}	load carried by CFST component in concrete-encased CFST column
N_u	total load carried by concrete-encased CFST column
P	peak load of concrete specimens

P_{c0}	unconfined concrete strength times the area of concrete core
P_{cover}	axial load carried by concrete cover
P_f	ultimate load of FRP tube
P_{ic}	axial load carried by inner concrete
P_{oc}	axial load carried by outer confined concrete
P_u	ultimate load of concrete column
P_y	yield load of concrete column
R	radius of confined concrete
R_i	inner radius of CFFTs with a central hole
R_o	outer radius of FRP tube
s	centre to centre spacing of neighbouring helices
s_g	spacing between transverse polymer grid
s'	clear spacing between neighbouring helices
t_{eq}	equivalent thickness
t_f	thickness of FRP
W	whole absorbed energy before failure
$W_{0.85P}$	absorbed energy before 85% post-peak load
$W_{0.50P}$	absorbed energy before 50% post-peak load
α	ratio between the inner diameter and outer diameter of FRP tube
δ_u	axial deformation at ultimate load P_u
δ_y	axial deformation at yield load P_y
δ_p	axial deformation at peak load P
$\delta_{0.85p}$	axial deformation at 85% post peak load
$\delta_{0.50p}$	axial deformation at 50% post peak load
δ	lateral deflection at ultimate load
Δf_{le}	increment of confining pressure
$\Delta\varepsilon_r$	increment of transverse strain
Δf_g	increment of tensile strength of polymer grid
ε_c	axial strain of concrete
$\varepsilon_{cc}^{'}$	corresponding axial compressive strain at $f_{cc}^{'}$

$\varepsilon_{cc}^{'*}$	corresponding axial strain of concrete under a specific constant confining pressure σ_R
$\overline{\varepsilon}_{cc}$	axial compressive strain corresponding to $\overline{f}_{cc}$
ε_{cco}	ultimate axial strain of unconfined concrete at f_{cco}
ε_{co}	axial strain of unconfined concrete at $f_{co}^{'}$
ε_{cu}	ultimate axial strain of confined concrete under concentric compression
$\varepsilon_{f,l}$	longitudinal strain at $\sigma_{f,l}$
$\varepsilon_{f,t}$	transverse strain at $\sigma_{f,t}$
ε_h	hoop strain of FRP
$\varepsilon_{h,rup}$	actual tensile rupture strain of FRP
$\varepsilon_{l,rup}$	longitudinal compressive strain of FRP tube at failure
ε_t	transition axial strain in which the parabolic first portion meets the linear second portion
ε_v	volumetric strain
η	axial critical load ratio
κ	axial stiffness ratio
λ	axial deformation ratio
μ	ductility
ξ	perforation parameter
ν	perforation ratio
ν_1	longitudinal Poisson's ratio of FRP tube
ν_2	transverse Poisson's ratio of FRP tube
υ_c	Poisson's ratio of concrete
ρ_{cc}	ratio of total area of longitudinal reinforcement to the area of concrete core
ρ_K	confinement stiffness ratio
ρ_ε	strain ratio
σ_c	axial stress of concrete
$\sigma_{f,l}$	longitudinal compressive stress of FRP tube
$\sigma_{f,t}$	transverse tensile stress of FRP tube

σ_R	lateral confining pressure
σ_t	maximum tensile stress of concrete
τ	shear strength of FRP tube

1 INTRODUCTION

1.1 General

In the past two decades, a significant number of studies were carried out on the use of fibre reinforced polymer (FRP) composites in civil engineering construction. One major application is the use of FRP jacket for strengthening existing concrete columns. Many studies reported the effectiveness of FRP jacket to enhance the performance of concrete columns by providing confinement to the concrete. More recently, several studies have been focussed on the use of FRP composites for the construction of new concrete structures, such as concrete-filled FRP tubes (CFFTs) and FRP bars reinforced concrete (RC) members (Fam and Rizkalla 2001a; Yost et al. 2001; Fam and Rizkalla 2002; Fam et al. 2003; Fam et al. 2005; De Luca et al. 2010; Ozbakkaloglu 2013a; Hadi et al. 2016).

The CFFTs was firstly proposed by Mirmiran and Shahawy (1997). In CFFTs, the FRP tube acts as stay-in-place formwork and provides lateral confinement to concrete core. At the same time, the concrete core prevents the FRP tube from local buckling. A significant number of studies have been conducted to demonstrate the ability of CFFTs to develop considerable strength, stiffness and ductility, making FRP tube an attractive alternative to steel tube and steel bars (Fam and Rizkalla 2001b, 2002; Fam et al. 2005; Ozbakkaloglu 2013c). With the increasing popularity of the construction of CFFTs column in China, a national technical code was developed for the rational design of CFFTs (GB 50608 2012). Despite many advantages of CFFTs, some disadvantages are still evident, which includes poor fire resistance (Ji et al. 2008), brittle failure mode, and difficulty to create moment resisting connection to other structural components (Sadeghian et al. 2011). Due to these limitations, the application of CFFTs has been limited. At present, CFFTs is mostly used as bridge columns and piles where the above disadvantages can be reasonably avoided (GB 50608 2012).

The behaviour of concrete members internally reinforced with FRP bars has been investigated in recent years (ACI 440.1R 2006). These studies reported that FRP bars could be successfully used to replace traditional steel bars in RC beams

(Benmokrane et al. 1996; Yost et al. 2001). Nevertheless, the use of FRP bars as longitudinal reinforcement has not been considered a suitable option for RC compression members and not yet covered by ACI 440.1R (2006). The main reasons for not using the FRP bars in concrete columns are: (a) the strength of FRP bars in compression are less than those in tension (Deitz et al. 2003); (b) a tensile strength reduction of more than 40% can occur for transverse FRP bars with bends compared to the tensile strength of straight FRP bars due to fibre bending and stress concentration (Nanni et al. 1998; ACI 440.1R 2006); and (c) the longitudinal FRP bars are vulnerable to local bucking (De Luca et al. 2010). Therefore, ACI 440.1R (2006) does not recommend the use of FRP bars as longitudinal reinforcement in concrete columns.

In order to address the apparent disadvantages of CFFTs and FRP bars RC columns, a new type of hybrid concrete column, the FRP tube reinforced concrete (FTRC) column, is proposed in this study. The FTRC column is proposed by following the concepts of two relevant hybrid concrete columns: Prefabricated cage system (PCS) (Shamsai and Sezen 2005), and concrete-encased concrete-filled steel tube (CFST) columns (Lin et al. 2001). Therefore, for a better understanding of the FTRC columns, a brief description of these two relevant hybrid concrete columns is introduced in the following section.

1.2 Relevant hybrid concrete columns

Prefabricated cage system (PCS) has been used to provide both the longitudinal and transverse reinforcement for concrete columns (Figure 1.1). PCS is fabricated by perforating steel tubes or plates using punching, casting, or different cutting method. Column reinforced with PCS has better fire performance and corrosion resistance than concrete-filled steel tube (CFST) since the PCS reinforcement is protected by the concrete cover. PCS was firstly proposed by Shamsai and Sezen (2005). Since then, several studies have been conducted on PCS RC columns (Shamsai and Sezen 2005; Sezen and Shamsai 2006; Shamsai et al. 2007; Sezen and Shamsai 2008; Fisher and Sezen 2011; Sezen and Miller 2011; Shamsai and Sezen 2011; Rethnasamy et al. 2013).

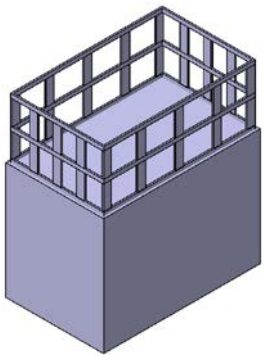

Figure 1.1 Prefabricated cage system (PCS) (Shamsai 2006)

Concrete-encased CFST columns are a new form of composite columns which have been proposed and investigated in recent years (Lin et al. 2001; Nie et al. 2008; Han et al. 2009; An et al. 2013; Xu and Liu 2013; An and Han 2014; An et al. 2014; Han and An 2014; Han et al. 2014; Ji et al. 2014; Liao et al. 2014; Han et al. 2015). Concrete-encased CFST columns consist of an inner CFST and an outer RC component, as shown in Figure 1.2. Compared to CFST columns, concrete-encased CFST columns have higher fire resistance and better durability under corrosive environment due to the protection from the outer RC component (Xu and Liu 2013). Concrete-encased CFST columns have easier connections with RC beams since longitudinal bars in RC beams can pass through or be anchored in the outer RC component (Nie et al. 2008; Liao et al. 2014). Also, due to the confinement provided by the outer RC component, the outward buckling of the steel tube could be restrained effectively.

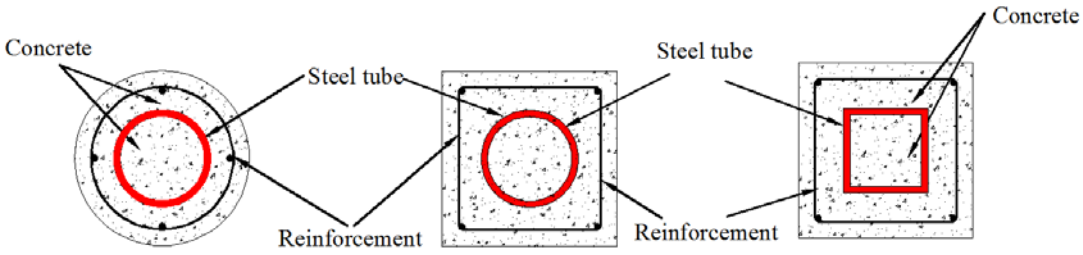

Figure 1.2 Concrete-encased CFST columns (Han et al. 2014)

1.3 FRP tube reinforced concrete (FTRC) column

Based on the above background, two types of FTRC columns have been proposed and investigated in this study. Type I FTRC column is reinforced with perforated FRP tube, as shown in Figure 1.3. While Type II FTRC column is composed of an inner concrete-filled FRP tube and an outer concrete component. The outer concrete component can be divided into two parts: outer confined concrete and concrete cover. Polymer grid has been used to provide confinement to outer confined concrete (Hadi and Zhao 2011; Wang et al. 2015a). Longitudinal reinforcement (e.g., FRP bars) can also be used for the outer concrete in order to improve the performance of FTRC column (Figure 1.4 (c)).

Figure 1.3 Perforated FRP tube

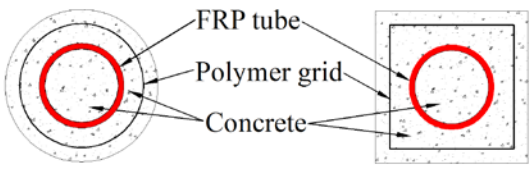

(a) With circular inner CFFT

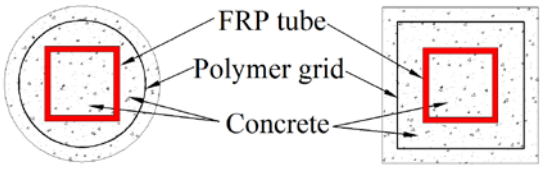

(b) With square inner CFFT

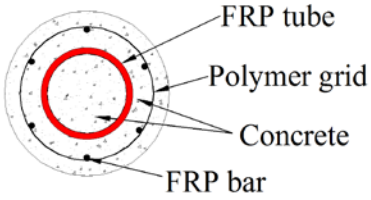

(c) Outer concrete with additional FRP bars

Figure 1.4 Type II FTRC column

Both types of FTRC columns are expected to provide several advantages that are not available in other types of concrete columns. Compared to steel bars RC column and CFST column, FTRC column possesses the advantages of being lightweight as well as good corrosion resistance. Compared to CFFTs, the fire resistance of FTRC column is significantly improved because of the presence of outer concrete component. Also, the spalling of concrete cover can be used as a suitable indication before sudden failure. Compared to FRP bars RC column, the local buckling of FRP bars will not happen since FRP bars are replaced by FRP tube. Moreover, the FRP tube can provide higher confinement to the concrete core than FRP bars. Hence, the strength and ductility of the FTRC column will be higher. Consequently, the cross-sectional dimension of the FTRC column can be reduced.

1.4 Research objectives

The main objectives of this thesis are to investigate the basic structural behaviour of the newly proposed FTRC columns. Therefore, the research work presented in this thesis has been carried out with the following specific objectives:

(1) To investigate the behaviour of Type I FTRC columns (reinforced with perforated FRP tube) under axial compression;
(2) To investigate the behaviour of perforated FRP tube under axial compression;
(3) To investigate the behaviour of Type II FTRC columns (reinforced with FRP tube and polymer grid) under axial compression;
(4) To investigate the behaviour of concrete confined with polymer grid under axial compression;
(5) To investigate the behaviour of FTRC columns under concentric, eccentric, and four-point loading conditions.

1.5 Thesis layout

The above specific objectives have been achieved and the details of current research are presented in the following chapters:

Chapter 2 presents an extensive literature review of previous studies which are related to the current study. Existing research on CFFTs, PCS RC columns, and concrete-encased CFST columns have been critically reviewed in this chapter.

Chapter 3 presents an experimental study on the behaviour of Type I FTRC columns (reinforced with perforated FRP tubes) under axial compression. In addition, numerical simulations have been carried out to assess the influence of tube perforations on the axial compressive behaviour of Type I FTRC columns.

Chapter 4 presents an experimental investigation on the influences of various parameters on the behaviour of perforated FRP tubes under axial compression. Also, design-oriented equations for the prediction of the axial stiffness, axial critical load and axial deformation capacity of perforated FRP tubes under axial compression have been proposed.

Chapter 5 presents the experimental study on the axial compressive behaviour of Type II FTRC columns (reinforced with FRP tube and polymer grid). An analytical model has been developed, and parametric analyses have been carried out by using the developed analytical model for better understanding the behaviour of Type II FTRC columns.

Chapter 6 presents an experimental study on the behaviour of concrete confined with polymer grid under axial compression. Based on the analysis of test results in this chapter as well as test results from previous studies, an analytical model for the polymer grid confined concrete was developed.

Chapter 7 presents an extensive experimental investigation on the behaviour of FTRC columns under different loading conditions (concentric, eccentric, and four-point loadings). Moreover, an incremental analytical procedure has been developed to predict the load carrying capacity and bending moment capacity of FTRC columns under different loading conditions.

Chapter 8 presents the summary and conclusions of this thesis. In addition, recommendations for further research are also given.

2 LITERATURE REVIEW

2.1 Introduction

This chapter presents a review of existing knowledge related to the newly proposed FRP tube reinforced concrete (FTRC) columns. As pointed out in Chapter 1, existing structural forms that are related to this new hybrid column are concrete-filled FRP tubes (CFFTs), prefabricated cage system (PCS) reinforced concrete columns, and concrete-encased concrete-filled steel tube (CFST) columns. Therefore, existing knowledge of these structural forms, including both experimental and theoretical investigations, are reviewed in this chapter.

2.2 Concrete-filled FRP tubes (CFFTs)

Concrete confined with prefabricated FRP tube is named concrete-filled FRP tubes (CFFTs). In CFFTs, the FRP tube acts as a stay-in-place structural formwork for the concrete and provides lateral confinement to concrete under compression. Moreover, the concrete can increase the stiffness of the members and prevent the FRP tube from local buckling. In addition to providing lateral confinement to concrete, the FRP tube can also be designed to sustain axial load. For FRP tube with all the fibres in the hoop direction and the axial stiffness can be neglected, the failure of CFFTs is controlled by the hoop rupture of FRP tube (Ozbakkaloglu 2013a, b; Vincent 2014; Xie and Ozbakkaloglu 2015). While for FRP tube with fibres oriented in different directions where the axial stiffness cannot be neglected, the failure of CFFTs is more complicated and more complex failure criterion should be considered (Mirmiran and Shahawy 1997; Mirmiran et al. 1998; Fam and Rizkalla 2001a; Mirmiran et al. 2001; Fam et al. 2003; Li et al. 2005; Zhu et al. 2005; Mohamed and Masmoudi 2010a).

2.2.1 Properties of FRP tubes

The mechanical properties of FRP tube are essential for the prediction of the behaviour of CFFTs under different loading conditions. FRP tube can be considered as a curved FRP laminate which is composed of two or more unidirectional laminas which are stacked together at different orientations. The lamina is an orthotropic

material with different properties in the three principal material axes. The properties of FRP laminate can be estimated based on the classical lamination theory (Daniel and Ishai 1994). In the classical lamination theory, a common fixed system of coordinates is used and the properties of a unidirectional lamina in this coordinate can be transformed from the principal material axes of this lamina. Afterwards, the mechanical properties of FRP laminate can be calculated by integration of the properties all layers of laminas in the common fixed system of coordinates. Even though reasonable prediction results can be obtained, the prediction error can be as large as 40%, 25%, and 50%, respectively, for the ultimate strength, elastic modulus, and Poisson's ratios of FRP tube (Fam 2000). Moreover, the basic properties of a unidirectional lamina are sometimes unavailable to researchers due to the difficulty of obtaining these properties. Therefore, other methods should be used in order to obtain more accurate properties of FRP tubes.

In addition to theoretical prediction, material property tests have been widely accepted and a series of standards have been developed for the determination of mechanical properties of FRP materials (ASTM D3039/D3039M 2000; ASTM D695 2002; ASTM D2290 2012; GB 50608 2012). The hoop tensile properties and longitudinal compressive properties of FRP tubes are considered to be the most important properties for the analysis of CFFTs under various loading conditions. The tensile properties of FRP composites can be obtained by two types of test: flat coupon test and ring splitting test. The ultimate strength and ultimate strain obtained from flat coupon test is always higher than the actual hoop tensile strain of FRP tube, and ring splitting test has been proved to be more accurate (Lam and Teng 2003; Chen et al. 2013). As for the longitudinal compressive properties of FRP tubes, a simple method is suggested by GB/T 5350-2005 (GB/T 5350 2005) by testing short FRP tubes under axial compression, and the compressive strength, compressive strain, the Young's modulus, and Poisson's ratio can be determined.

2.2.2 CFFTs under axial compression

A number of studies have been conducted on the behaviour of CFFTs under axial compression (Mirmiran and Shahawy 1996, 1997; Saafi et al. 1999; Fam and Rizkalla 2001a, b; Becque et al. 2003; Cho et al. 2005; Li et al. 2005; Zhu et al. 2005; Mohamed and Masmoudi 2010a; Ozbakkaloglu 2013a, b; Vincent 2014; Xie and Ozbakkaloglu 2015).

Fam and Rizkalla (2001a) investigated the behaviour of CFFTs (totally filled, partially filled with a central hole, and tube-in-tube system with concrete filling between two FRP tubes) under axial compression. The strength and ductility of concrete columns were improved due to the confinement provided by FRP tubes, and higher confinement can be achieved for totally filled CFFTs. Using central hole reduces the confinement effect; however, using inner tube can enhance the confinement for this type of members. Test results indicated that loading of the GFRP tubes reduces the confinement effectiveness. Filament-wound GFRP tubes are superior to pultruded tubes in confinement. Stress-strain curve of concrete confined with FRP tube is bilinear with the transition zone near the peak strength of the unconfined concrete, and the slope of the second branch is governed by the axial stiffness of the tube as well as the inner hole size.

An analytical model was proposed by Fam and Rizkalla (2001b) to predict the behaviour of CFFTs (totally filled and partially filled with a central hole) under axial compression. Due to the existence of axial stiffness of FRP tube, the Tsai-Wu failure criteria were used to consider the biaxial stress state of FRP tube (Tsai and Wu 1971). The following equation was proposed based on the linear elasticity theory for the first two steps of the proposed incremental calculation procedure:

$$\sigma_R = \frac{(R_o - R_i)\upsilon_c}{\dfrac{R_o^2}{E_{f,t}t} + \dfrac{R_o\left(\dfrac{R_o^2 + R_i^2}{R_o^2 - R_i^2} - \upsilon_c\right)}{E_c}}\varepsilon_c \qquad 2.1$$

where σ_R indicates the lateral confining pressure, R_o and R_i are the outer and inner radii of column section, υ_c is the Poisson's ratio of concrete, ε_c is the general axial

strain of concrete, $E_{f,t}$ is the transverse tensile elastic modulus of FRP tube, and E_c is the elastic modulus of concrete.

Fam and Rizkalla (2001b) model is an extension of the confinement model proposed by Mander et al. (1988), which is actually an analysis-oriented stress-strain model which adopts the same incremental procedure as that for FRP-wrapped concrete (Jiang and Teng 2007). Even though reasonable prediction results can be obtained, it was assumed that the confining stress and the axial stress are uniform over the column section. This assumption is reasonable for totally filled CFFTs, while it is not consistent with the observation from columns with hollow section (Wong et al. 2008). In addition, the equation for the Poisson's ratio of concrete υ_c is based on the test results for actively-confined concrete, which may not be proper for FRP-confined concrete. Jiang and Teng (2007) concluded that Fam and Rizkalla (2001b) model cannot provide reasonable predictions of the results of FRP-confined concrete.

Ozbakkaloglu (2013c) conducted a comprehensive study on the behaviour of CFFTs under axial compression. The majority of the FRP tubes used in this study were manufactured by wet lay-up method. All the FRP materials were impregnated with epoxy resin and were wrapped around a high-density styrofoam template in the hoop direction. FRP-wrapped concrete were also tested to investigate the difference between CFFTs and FRP-wrapped concrete. The results indicated that for FRP tubes manufactured by wet lay-up method with all the fibres in the hoop direction, the performance of CFFTs was found to be almost the same with companion FRP-wrapped concrete. The concrete strength, cross-sectional shape, and the type of FRP material significantly affect the behaviour of CFFTs. The influence of specimen size was found to be insignificant.

2.2.3 Stress-strain relationship of FRP-confined concrete

Many stress-strain models have been proposed for FRP-confined concrete under axial compression. The proposed stress-strain models can be classified into two categories: (a) design-oriented models; and (b) analysis-oriented models. When FRP

tube only provides lateral confinement and does not sustain axial load (or the axial stiffness of FRP tube can be neglected), all the stress-strain models for FRP-wrapped concrete are theoretically applicable for concrete confined by FRP tubes. In the present study, the stress-strain models of FRP confined concrete are summarized below since these models successfully interpret the confinement mechanism provided by the FRP composites.

2.2.3.1 Design-oriented stress-strain models

In design-oriented stress-strain models, the ultimate compressive strength, the ultimate axial strain as well as the stress-strain curve of FRP-confined concrete are predicted using closed-form equations based directly on the interpretation and regression analysis of experimental results (Lam and Teng 2003; Ozbakkaloglu et al. 2013; Pham and Hadi 2013). Therefore, the accuracy of design-oriented models depends heavily on the reliability and the size of the experimental database, as well as the variables or parameters selected for inclusion in the closed-form equations. Among these models, the stress-strain model proposed by Lam and Teng (2003) has been proved to be one of the most accurate stress-strain models (Ozbakkaloglu et al. 2013) and has been adopted in ACI 440.2R (2008).

In Lam and Teng (2003) model, a parabolic first portion together with a linear second portion was proposed to describe the stress-strain curve of FRP-confined concrete. The stress-strain model proposed by Lam and Teng (2003) is expressed by the following expressions:

$$\sigma_c = E_c\varepsilon_c - \frac{(E_c - E_2)^2}{4f_o}\varepsilon_c^2 \quad \text{for } 0 \le \varepsilon_c \le \varepsilon_t \tag{2.2}$$

$$\sigma_c = f_o + E_2\varepsilon_c \quad \text{for } \varepsilon_t \le \varepsilon_c \le \varepsilon_{cu} \tag{2.3}$$

where σ_c and ε_c are the axial stress and axial strain, respectively; E_c is the elastic modulus of unconfined concrete; E_2 is the slope of the linear second portion of the stress-strain curve; f_o is the intercept of the stress axis by the linear second portion; and ε_{cu} is the ultimate axial strain of confined concrete. The parabolic first portion meets the linear second portion with a smooth transition at ε_t, which is given by

$$\varepsilon_t = \frac{2 f_o}{\left(E_c - E_2\right)} \tag{2.4}$$

The slope of the linear second portion E_2 is given by

$$E_2 = \frac{f_{cc}^{'} - f_o}{\varepsilon_{cu}} \tag{2.5}$$

where $f_{cc}^{'}$ is the compressive strength of confined concrete. The value of f_o is assumed to be the compressive strength of unconfined concrete $f_{co}^{'}$.

The equations to calculate the ultimate compressive strength and ultimate axial strain of FRP-confined concrete are given by:

$$\frac{f_{cc}^{'}}{f_{co}^{'}} = \begin{cases} 1 + 3.3\dfrac{f_{lu,a}}{f_{co}^{'}} & f_{lu,a} / f_{co}^{'} \geq 0.07 \\ 1 & f_{lu,a} / f_{co}^{'} < 0.07 \end{cases} \tag{2.6}$$

$$\frac{\varepsilon_{cu}}{\varepsilon_{co}} = 1.75 + 12\left(\frac{f_{lu,a}}{f_{co}^{'}}\right)\left(\frac{\varepsilon_{h,rup}}{\varepsilon_{co}}\right)^{0.45} \tag{2.7}$$

where $f_{lu,a}$ is the actual lateral confining pressure at ε_{cu}; ε_{co} is the axial strain of unconfined concrete at peak strength $f_{co}^{'}$; and $\varepsilon_{h,rup}$ is the actual tensile rupture strain of FRP.

Even though satisfactory prediction results can be obtained by using Lam and Teng (2003) model, there are some deficiencies in this model. Experimental observations reported by Teng et al. (2009) confirmed that the confinement stiffness can significantly influence the ultimate compressive strength and ultimate axial strain of FRP-confined concrete. Nevertheless, the influence of confinement stiffness on the ultimate conditions of FRP-confined concrete cannot be reflected in Lam and Teng (2003) model. Teng et al. (2009) refined Lam and Teng (2003) model and proposed new equations for the prediction of ultimate compressive strength and ultimate axial strain of FRP-confined concrete:

$$\frac{f_{cc}^{'}}{f_{co}^{'}} = \begin{cases} 1 + 3.5\left(\rho_K - 0.01\right)\rho_\varepsilon & \rho_K \geq 0.01 \\ 1 & \rho_K < 0.01 \end{cases} \tag{2.8}$$

$$\frac{\varepsilon_{cu}}{\varepsilon_{co}} = 1.75 + 6.5\rho_K^{0.8}\rho_\varepsilon^{1.45} \quad 2.9$$

The confinement ratio $f_{lu,a} / f_{co}^{'}$, the confinement stiffness ratio ρ_K, and the strain ratio ρ_ε can be calculated by the following equations:

$$\frac{f_{lu,a}}{f_{co}^{'}} = \frac{E_{f,t}t_f\varepsilon_{h,rup}}{f_{co}^{'}R} = \rho_K\rho_\varepsilon \quad 2.10$$

$$\rho_K = \frac{E_{f,t}t_f}{\left(f_{co}^{'} / \varepsilon_{co}\right)R} \quad 2.11$$

where t_f is the thickness of FRP, and R is the radius of confined concrete.

Moreover, Lam and Teng (2003) model failed to predict the descending branch of FRP-confined concrete with strain softening response. In order to solve this deficiency, Teng et al. (2009) proposed a refinement model which caters for both stress-strain curves with a descending branch and stress-strain curves with an ascending branch.

2.2.3.2 Analysis-oriented stress-strain models

In analysis-oriented stress-strain models, the stress-strain curves of FRP-confined concrete are generated via an incremental numerical procedure. Analysis-oriented models are capable of predicting not only the response of sufficiently FRP-confined concrete with a strain hardening response, but also that of insufficiently FRP-confined concrete with a strain softening response. The analysis-oriented models are usually built on the path-independence assumption, which indicates that the axial stress and the axial strain of concrete confined with FRP at a given lateral strain are the same as those of the same concrete actively confined with a constant confining pressure equal to that supplied by the FRP jacket (Jiang and Teng 2007). The stress–strain curve of FRP–confined concrete can be obtained through the following procedure: (1) for a given axial strain, find the corresponding lateral strain of effectively confined concrete according to the lateral-to axial strain relationship; (2) calculate the corresponding lateral confining pressure provided by the FRP jacket based on force equilibrium and radial displacement compatibility between the

concrete core and the FRP jacket; (3) use the axial strain and the confining pressure obtained from Steps (1) and (2), together with an active-confinement stress-strain model to evaluate the corresponding axial stress, therefore, one point on the stress–strain curve of FRP-confined concrete can be obtained; (4) repeat the above steps to develop the full stress–strain curve of FRP-confined concrete.

Compared to a large number of design-oriented models, only a few models can be categorized into analysis-oriented models (Ozbakkaloglu et al. 2013). Among these models, the model proposed by Jiang and Teng (2007) has been shown to be one of the most satisfactory models. The stress-strain model firstly proposed by Popovics (1973) was adopted by Jiang and Teng (2007) as active-confinement stress-strain model, which is given by the following equations:

$$\frac{\sigma_c}{f_{cc}^{'*}} = \frac{(\varepsilon_c / \varepsilon_{cc}^*)r}{r - 1 + (\varepsilon_c / \varepsilon_{cc}^*)^r} \tag{2.12}$$

$$r = \frac{E_c}{E_c - f_{cc}^{'*} / \varepsilon_{cc}^*} \tag{2.13}$$

$$\frac{f_{cc}^{'*}}{f_{co}^{'}} = 1 + 3.5\frac{\sigma_R}{f_{co}^{'}} \tag{2.14}$$

$$\frac{\varepsilon_{cc}^{'*}}{\varepsilon_{co}} = 1 + 17.5\left(\frac{\sigma_R}{f_{co}^{'}}\right)^{1.2} \tag{2.15}$$

where σ_c and ε_c = axial stress and axial strain of concrete, respectively; E_c = elastic modulus of concrete; $f_{co}^{'}$ = compressive strength of unconfined concrete; σ_R = lateral confining pressure from FRP; ε_{co} = axial strain at peak strength of unconfined concrete; $f_{cc}^{'*}$ and $\varepsilon_{cc}^{'*}$ are, respectively, the peak axial stress and the corresponding axial strain of concrete under a specific constant confining pressure σ_R.

The success of an analysis-oriented model depends mainly on the close representation of the lateral deformation characteristics of FRP-confined concrete (Jiang and Teng 2007). The following equation was adopted by Jiang and Teng (2007) for the axial strain-hoop strain relationship:

$$\frac{\varepsilon_c}{\varepsilon_{co}} = 0.85\left(1+8\frac{\sigma_R}{f'_{co}}\right)\left(\left[1+0.75\left(\frac{\varepsilon_h}{\varepsilon_{co}}\right)\right]^{0.7} - exp\left[-7\left(\frac{\varepsilon_h}{\varepsilon_{co}}\right)\right]\right) \quad 2.16$$

Based on force equilibrium, the confining pressure σ_R can be related to the hoop strain ε_h by:

$$\sigma_R = \frac{E_{f,h} t_f \varepsilon_h}{R} \quad 2.17$$

where $E_{f,h}$, t_f, ε_h = tensile elastic modulus, thickness and hoop strain of the FRP jacket, respectively.

2.2.4 CFFTs under flexural loading

Studies on the flexural behaviour of CFFTs have been conducted by Fam et al. (Fam and Rizkalla 2002; Fam et al. 2003; Fam and Rizkalla 2003; Fam et al. 2005; Cole and Fam 2006; Fam et al. 2007), Mirmiran et al. (Mirmiran et al. 1999; Mirmiran et al. 2000), and Mohamed et al. (Mohamed and Masmoudi 2010b, 2011). For CFFTs under flexural loading, the FRP tube carries the tensile forces in the tension zone, and it provides partial confinement of concrete in the compression zone. Moreover, the concrete mainly provides compressive strength and prevents local buckling of the FRP tube.

Fam and Rizkalla (2002) conducted a large-scale bending test of circular CFFTs. The influences of concrete filling, cross-sectional shapes, and laminate structures of the FRP tube on the flexural behaviour of CFFTs were investigated. The main conclusions include: (1) the confinement effect of concrete provided by FRP tube in the compression zone is insignificant; however, the ductility of the concrete can be increased due to the existence of FRP tube; (2) the failure of CFFTs was dominated by FRP tube. CFFTs with thicker FRP tube for a given laminate structure or higher percentage of fibres in the axial direction tend to fail in compression, while CFFTs with thin FRP tube for a given laminate structure or lower percentage of fibres in the axial direction tend to fail in tension; (3) partial concrete filling inside the FRP tube can result in a higher flexural strength-to-weight ratio, and higher strength and

stiffness can be obtained by providing an inner FRP tube; (4) the load-deflection behaviour of CFFTs is almost linear, and the stiffness after cracking is mainly governed by the laminate structure of the FRP tube; (5) slip could happen between the concrete core and FRP tube, and a shear transfer mechanism may be used in flexural members.

In order to predict the moment-curvature response of CFFTs, an analytical model was adopted by Fam and Rizkalla (2002). In this model, the stress-strain curve of unconfined concrete proposed by Popovics (1973) with extended strain softening was adopted as the stress-strain curve of concrete in CFFTs under flexure, and a linear stress-strain curve is used for the FRP tube in both tension and compression. A layer-by-layer approach, which has been widely used for the prediction of flexural capacity of concrete beams (Fam and Rizkalla 2002; Fam et al. 2003; Fam et al. 2005; Cole and Fam 2006; Yu et al. 2006; Yazici and Hadi 2009; Mohamed and Masmoudi 2010b; Hadi et al. 2013), was used for the calculation. In the layer-by-layer approach, the cross section of CFFTs is divided into a number of strips. The properties of concrete and FRP tube in each strip can be calculated based on the plane section assumption. The calculated stresses are then integrated over the cross-sectional area to obtain the resultant force and the resultant moment. The prediction results were found to be satisfactory when compared to the experimental results.

Cole and Fam (2006) investigated the flexural performance of CFFTs with internal reinforcement. Steel, GFRP, or CFRP rebar of various reinforcement ratios were placed into CFFTs to act as longitudinal reinforcement. Test results showed that CFFTs with steel rebar failed in a ductile manner. However, CFFTs with FRP rebar had a significantly lower ductility than CFFTs with steel rebar. The flexural performance of CFFTs with steel rebar can be significantly improved by increasing the steel reinforcement ratios. Cole and Fam (2006) also developed an analytical model to predict the flexural behaviour of CFFTs. Two concrete stress-strain models were examined in the analytical model. The first concrete model is the unconfined concrete model suggested by Popovics (1973) with extended strain softening stage (Fam and Rizkalla 2002). The second concrete model is called partially confined

concrete model, which is similar to Popovics (1973) model before the unconfined concrete strength. After the unconfined concrete strength is reached, the concrete strength kept constant until the ultimate axial strain was reached. The reason to use the partially confined concrete model is due to the experimental observations that concrete in the compression zone of reinforced CFFTs experienced a higher confinement level than unreinforced CFFTs. The results indicated that the unconfined concrete model underestimated the performance of reinforced CFFTs, and better predictions can be obtained by using the partially confined concrete model.

Studies by Yu et al. (2006) further indicated that by using the stress-strain relationship of unconfined concrete to simulate the behaviour of CFFTs under pure bending, conservative prediction results can be obtained. Based on the experimental results on the flexural performance of hybrid FRP-concrete-steel double-skin tubular members, the following equations were adopted to predict the stress-strain curves of concrete in the compression region of hybrid FRP-concrete-steel double-skin tubular flexural members:

$$\sigma_c = f_{co}^{'}\left[\frac{2\varepsilon_c}{\varepsilon_{co}} - \left(\frac{\varepsilon_c}{\varepsilon_{co}}\right)^2\right] \text{ when } \varepsilon_c \le \varepsilon_{co} \qquad 2.18$$

$$\sigma_c = f_{co}^{'} \text{ when } \varepsilon_c > \varepsilon_{co} \qquad 2.19$$

Due to the simplicity and accuracy of this concrete model, the Chinese national code GB 50608 (2012) adopted this model to predict the response of concrete in CFFTs under flexure.

2.2.5 CFFTs under eccentric compression

The behaviour of CFFTs under eccentric loading has been studied in several literatures (Mirmiran et al. 1999; Mirmiran et al. 2000; Fam et al. 2003; Fam and Rizkalla 2003; Li and Hadi 2003; Fam et al. 2005; Hadi 2006a, b).

Fam and Rizkalla (2003) experimentally investigated the behaviour of CFFTs under concentric, eccentric, and flexural loadings by testing a total of 23 CFFTs. Different loading eccentricities were applied. The interaction diagrams of CFFTs were established based on the test results. It can be seen that with the increase of eccentricity, the load carrying capacity of CFFTs decreased. The shapes of interaction diagram curves are similar between traditional steel RC and CFFTs, and the interaction diagram curves can be divided into two stages. At the first stage, the axial load increases with the increase of bending moment, which indicates the tension failure of FRP tube. At the second stage, the axial load increases with the decrease of bending moment, which indicates the crushing of fibres in the compression area of FRP tube. Moreover, the interaction diagram curves of CFFTs can be varied significantly with different laminate structures, and a reasonable laminate structure can result in better strength and stiffness in both the axial and hoop directions.

A variable confinement model was suggested by Fam et al. (2003) to predict the behaviour of CFFTs under eccentric compression. The stress-strain curves of concrete in CFFTs under eccentric compression lies between that for concrete in CFFTs under axial compression (Fam and Rizkalla 2001b) and that of unconfined concrete with extended strain softening stage (Fam and Rizkalla 2002). The proposed variable confinement model for the concrete under eccentric compression is represented by the following equation based on Popovics (1973) model:

$$\frac{\overline{f}_{cc}}{f_{co}^{'}} = \frac{\dfrac{\overline{\varepsilon}_{cc}}{\varepsilon_{co}}(\alpha r)}{(\alpha r) - 1 + \left(\dfrac{\overline{\varepsilon}_{cc}}{\varepsilon_{co}}\right)^{(\alpha r)}} \qquad 2.20$$

where $\overline{f}_{cc}$ = ultimate compressive strength of concrete for a given eccentricity e; $f_{co}^{'}$ = compressive strength of unconfined concrete; $\overline{\varepsilon}_{cc}$ = axial compressive strain corresponding to $\overline{f}_{cc}$; ε_{co} = corresponding axial strain of unconfined concrete at $f_{co}^{'}$; $r = E_c / (E_c - E_{sec})$, E_c = elastic modulus of unconfined concrete, and $E_{sec} = f_{co}^{'} / \varepsilon_{co}$; and the parameter α can be solved if $\overline{f}_{cc}$ and $\overline{\varepsilon}_{cc}$ are found.

The ultimate compressive strength $\overline{f}_{cc}$ and corresponding axial strain $\overline{\varepsilon}_{cc}$ for a given eccentricity e can be defined as follows:

$$\overline{f}_{cc} = \left(f'_{cc} - f_{cco}\right)\left[\frac{D_o}{D_o + e}\right] + f_{cco} \qquad 2.21$$

$$\overline{\varepsilon}_{cc} = \left(\varepsilon_{cco} - \varepsilon_{cu}\right)\sqrt{1 - \left(\frac{\overline{f}_{cc} - f_{cco}}{f'_{cc} - f_{cco}}\right)} + \varepsilon_{cu} \qquad 2.22$$

where D_o = the outer diameter of FRP tube; ε_{cco} = ultimate axial strain of unconfined concrete for beam specimens, which equals to ultimate axial strain of FRP tube in compression; f_{cco} = axial compressive stress corresponding to ε_{cco}; ε_{cu} = ultimate axial strain of CFFTs under concentric compression; f'_{cc} = ultimate compressive strength of CFFTs under concentric compression. For CFFTs under axial compression ($e = o$), $\overline{f}_{cc} = f'_{cc}$, and for CFFTs under pure bending ($e = \infty$), $\overline{f}_{cc} = f_{cco}$.

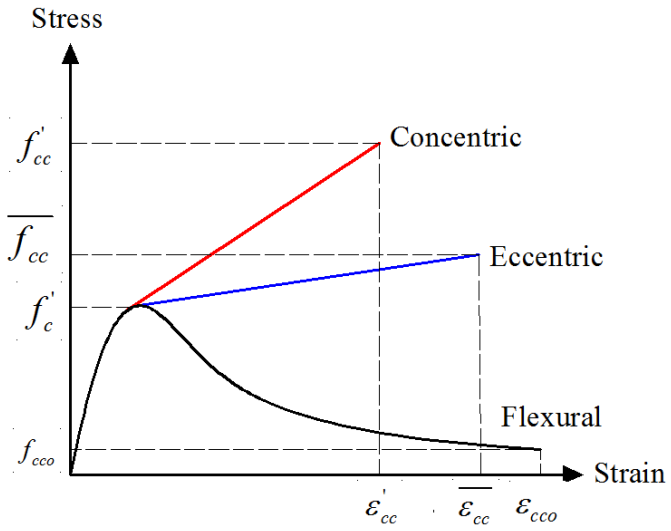

Figure 2.1 Variable confinement model (Fam et al. 2003)

Yu et al. (2010a) conducted eccentric compression tests for hybrid-concrete-steel double-skin tubular columns. Based on their experimental observations, a so-called "variable confinement model" was proposed for the confined concrete under eccentric compression. The equations for the model is an extension of Lam and Teng (2003) model. In this model, the effect of strain gradient on the confinement effectiveness is considered by relating the slope of the second linear portion of the

concrete stress-strain curve to the load eccentricity in a manner similar to that proposed by Fam et al. (2003):

$$E_{2ec} = E_2 \frac{D_o}{D_o + e} \tag{2.23}$$

where E_{2ec} = the slope of the second linear portion of the concrete stress-strain curve to the load eccentricity e; E_2 = the slope of the linear second portion of the concrete stress-strain curve under concentric compression; D_o = the outer diameter of FRP tube.

2.2.6 Fire performance

Ji et al. (2008) experimentally investigated the performance of CFFTs exposed to fire. CFFTs without fire exposure, under fire exposure without fireproof, and under fire exposure with fireproof additive were tested. The CFFTs were exposed to a jet fire of 982℃ for 4 minutes, 8 minutes and 12 minutes, respectively. After the fire test, all CFFTs were tested under axial compression. The test results showed that the load carrying capacities of CFFTs under fire exposure were significantly reduced. For CFFTs under 12 minutes of fire exposure, all the confinement was lost. Fire exposure resulted in a consumption of the resin, which was observed by the scanning electron microscope (SEM).

2.3 Relevant hybrid concrete columns

2.3.1 Prefabricated cage system

Prefabricated cage system (PCS) is fabricated by perforating steel tubes or plates using punching, casting, or different cutting method. PCS can be used to provide both the longitudinal and transverse reinforcement for concrete columns (Figure 1.1). Compared to traditional steel reinforcement, PCS reinforcement has the following advantages: (1) the total construction cost can be reduced (Shamsai et al. 2007); (2) improves the structural performance (Sezen and Shamsai 2008; Sezen and Miller 2011; Shamsai and Sezen 2011; Rethnasamy et al. 2013); (3) the PCS has better fire performance and corrosion resistance than CFST since the PCS reinforcement is

protected by the concrete cover. PCS was firstly proposed by Sezen and Shamsai (Shamsai and Sezen 2005; Sezen and Shamsai 2006; Shamsai 2006; Shamsai et al. 2007; Sezen and Shamsai 2008). Since then, several studies have been conducted to investigate the use of PCS as reinforcement of concrete columns (Shamsai and Sezen 2005; Sezen and Shamsai 2006; Shamsai 2006; Sezen and Shamsai 2008; Shamsai and Sezen 2011), beams (Chithra and Thenmozhi 2010; Chithra et al. 2011; Rethnasamy et al. 2013), and beam-column joints (Fisher and Sezen 2011).

Sezen and Shamsai (2008) investigated the axial compressive behaviour of high-strength concrete columns reinforced with PCS. Steel bars RC columns with equal amounts of transverse and longitudinal steel were also tested for comparison. The axial strength and deformation capacity were experimentally studied. The experimental results indicated that PCS reinforced concrete columns exhibited very similar axial load-axial deformation curves to steel bars RC columns. The load carrying capacities of both PCS reinforced concrete columns and steel bars RC columns were similar, while a higher post-peak strength and deformation capacity can be observed for PCS reinforced concrete columns. PCS reinforced concrete columns with thicker tube thickness can obtain slightly higher peak strength. If the amount of steel reinforcement was kept constant, varying the number of longitudinal strips and the transverse reinforcement spacing did not significantly affect the performance of PCS reinforced concrete columns. A new analytical model was proposed to predict the axial load-deformation behaviour of PCS reinforced concrete columns under axial compression, and the prediction results matched well with the experimental results. Shamsai and Sezen (2011) further investigated the behaviour of normal strength concrete columns reinforced with PCS. Similar conclusions can be drawn. Moreover, it was concluded that the existence of crossties helps prevent buckling of PCS reinforcement and therefore, improves the confinement efficiency, strength and deformation capacity.

Rethnasamy et al. (2013) experimentally and analytically investigated the flexural behaviour of concrete beams reinforced with PCS. A total of 18 PCS beam specimens were tested under four-point loading. In order to compare the behaviour of

PCS beam specimens and traditional steel RC beam specimens, three steel bars RC beams with the same amount of steel reinforcement were tested as well. The test results indicated that PCS beam specimens exhibited better flexural performance especially after the yielding of steel than that of traditional steel RC beams. The initiation and development of cracks were delayed by the PCS reinforcement. Also, the load carrying capacities of PCS beam specimens were higher than that of steel bars RC beams. PCS beam specimens behave in a more ductile manner under bending. In addition to experimental investigation, a section analysis method was adopted to predict the flexural strength of PCS beam specimens. The equivalent stress block was used to transfer non-uniform confined concrete stresses to rectangular distribution of stresses, as recommended by AS 3600 (2009). A close agreement with experimental results can be observed.

2.3.2 Concrete-encased concrete-filled steel tube (CFST) columns

Concrete-encased concrete-filled steel tube (CFST) columns are a new form of composite columns which have been proposed and investigated in recently years (Lin et al. 2001; Nie et al. 2008; Han et al. 2009; An et al. 2013; Xu and Liu 2013; An and Han 2014; An et al. 2014; Han and An 2014; Han et al. 2014; Ji et al. 2014; Liao et al. 2014; Han et al. 2015). Concrete-encased CFST columns consist of an inner CFST and outer RC, as shown in Figure 1.2. Compared to the conventional CFST columns, concrete-encased CFST columns have higher fire resistance and better durability under corrosive environment due to the protection from the outer RC (Xu and Liu 2013). Concrete-encased CFST columns have easier connections with RC beams since longitudinal bars in RC beams can pass through or be anchored in the outer RC (Nie et al. 2008; Liao et al. 2014). Also, due to the confinement provided by its outer RC, the outward buckling of the steel tube could be restrained effectively. Concrete-encased CFST columns have higher ductility due to the existence of CFST compared to conventional steel RC columns (Han and An 2014). Also, due to the possibility of using high strength concrete and thin-walled high strength steel tube in CFST, the column section size of concrete-encased CFST columns could also be reduced.

Han and An (2014) developed a three dimensional finite element model to investigate the behaviour of concrete-encased CFST columns under axial compression. Different stress-strain models have been selected for outer unconfined concrete, outer confined concrete, and core concrete. The interactions between different materials were also considered. The calculated axial load-axial strain curve of the concrete-encased CFST column can be divided into five stages. At the first stage, the column generally shows elastic behaviour. At the second stage, the outer unconfined concrete reaches the ultimate strength and begins to crush, and the steel tube and longitudinal bar have yielded at the end of this stage. At the third stage, even though the strength of the outer unconfined concrete decreases, the strength of the column increases, which is due to the improved strength of core concrete inside steel tube and outer confined concrete. At the end of this stage, the outer confined concrete reaches the ultimate strength. At the fourth stage, the load begins to decrease and the axial strain increases quickly. The strengths of outer confined concrete decrease, while the strength of core concrete increases slowly. At the end of this stage, the axial load becomes stable. The parametric study shows that by increasing the outer concrete strength, core concrete strength, longitudinal bar ratio, steel ratio of CFST, and diameter of inner CFST can significantly increase the ultimate strength. Also, by decreasing the spacing between steel stirrups, the ultimate strength can be increased.

An and Han (2014) numerically investigated the behaviour of concrete-encased CFST columns under combined compression and bending. The failure mode is similar to that of the conventional steel RC columns (compression-controlled failure and tension-controlled failure). For columns with compression controlled failure, the compressive concrete crushes before the yielding of longitudinal bar in the tension side, and the ratio between the bending moment carried by the CFST component M_{cfst} and bending moment of whole column M_u increases with the increase of eccentricity. While for columns with tension-controlled failure, the longitudinal bars in the tension side yields before the crushing of concrete in the compression side, and the influence of eccentricity on M_{cfst} / M_u is moderate. The influence of eccentricity

on the ratio between the load carried by CFST component N_{cfst} and the total load carried by the column N_u is moderate if e/B is less than 0.2 (B indicates the total section width of the columns). However, for columns with a larger e/B (>0.2), the increase of eccentricity can lead to a decrease of N_{cfst}/N_u.

An et al. (2014) further investigated the flexural behaviour of concrete-encased CFST columns. The RC beam and CFST beam were also designed and assessed for comparison purpose. The flexural capacity of concrete-encased CFST was found to be larger than that of the RC beam with the same amount of longitudinal steel. Due to the presence of outer RC, thin-walled steel tubes can be used in concrete-encased CFST and can develop full plastic strength without local buckling before reaching the ultimate state. The tension area of the inner CFST in the concrete-encased CFST is larger than that in the corresponding CFST due to the contribution of compressive outer RC, which indicates that the contribution of the inner CFST to flexural capacity is larger for the concrete-encased CFSTs than for the corresponding CFST. A strut-and-tie model was proposed for the load transfer of both outer and inner components. The shear force is mainly sustained by the inner CFST; therefore, the shear resistance capacity of the concrete-encased CFST is enhanced when compared to the RC beam.

2.4 Summary

This chapter has provided a review of existing research studies relevant to the proposed FRP tube reinforced concrete (FTRC) columns. A summary of both experimental results and theoretical models for predicting the behaviour of concrete-filled FRP tubes (CFFTs) under different loading conditions has been presented first, followed by the introduction of two relevant types of hybrid concrete columns. The advantages of these two types of hybrid concrete columns were examined, and their performance under various loading conditions was introduced. Against this background, this thesis presents a series of experimental and theoretical studies on the basic structural behaviour of FTRC columns.

In Chapter 3, an experimental program was firstly carried out to investigate the axial compressive behavior of Type I FTRC columns. Afterwards, the experimental results were presented. Finally, numerical simulations were conducted to investigate the influences of tube perforations on the performance of Type I FTRC columns under axial compression.

3 BEHAVIOUR OF TYPE I FTRC COLUMN UNDER AXIAL COMPRESSION

3.1 Introduction

Following the concept of Prefabricated cage system (PCS), Type I FTRC column was proposed in which the column was reinforced with perforated FRP tube. In order to have an in-depth understanding of the axial compressive behaviour of the proposed Type I FTRC column, an experimental programme was carried out. The axial load-axial deformation behaviour was investigated. The strength, ductility and failure modes were critically studied. Moreover, numerical simulations were conducted to investigate the influence of tube perforations on the axial compressive behaviour of Type I FTRC columns. For simplicity, the term “Type I FTRC column” was referred to as “FTRC column” in this chapter.

3.2 Experimental program

3.2.1 Materials and specimens

Glass fibre reinforced polymer (GFRP) tubes manufactured by Wagners CFT, Australia, were chosen as the reinforcement material (Wagners CFT 2015). The solid GFRP tubes (ST) were 260 mm long and 6 mm thick with 77 mm internal diameter. In addition to the solid GFRP tubes, perforated tubes were selected as well (Figure 3.1). The purpose of using perforated tubes is mainly to integrate the concrete core with concrete cover, which may prevent the concrete cover from premature spalling (Shamsai 2006). Moreover, mechanical interlocking can be developed between the perforated GFRP tube and concrete, forming a higher interfacial shear strength (Ji et al. 2009). 25 mm diameter circular holes were drilled to create perforations into the GFRP tubes. Two different perforation patterns (axial and diagonal) were studied. Axially perforated GFRP tubes have been designated as APT and diagonally perforated GFRP tubes have been specified as DPT in this study. Four rows of holes were drilled in each tube. The rows were symmetrically distributed along the tube circumference. The clear vertical spacing between the holes was 40 mm. 16 holes were drilled in APT and 14 holes were drilled in DPT. Moreover, in order to prevent the GFRP tubes from premature rupture and to improve the hoop tensile strength,

two layers of Carbon Fibre Reinforced Polymer (CFRP) sheet were wrapped onto the tubes (Figure 3.1). The laterally wrapped GFRP tubes were labelled ST-LW, APT-LW, and DPT-LW, in which "LW" means the tube was laterally wrapped with CFRP sheet. Figure 3.1 shows different GFRP tubes used in this study.

(a) ST tube (b) APT (c) DPT (d) ST-LW (e) APT-LW (f) DPT-LW

Figure 3.1 GFRP Tube configurations (Hadi et al. 2015)

A total of 14 concrete specimens were cast and tested under axial compression. The specimens were 150 mm in diameter and 300 mm in height. Concrete clear cover was 30 mm on the sides and 20 mm at the top and bottom of the specimens. The specimens were divided into seven groups. Each group contained two identical specimens. The specimens were made of normal strength concrete with a design compressive strength of 32 MPa. The maximum size of the coarse aggregate for concrete was 10 mm. Details of the specimens are shown in Figure 3.2.

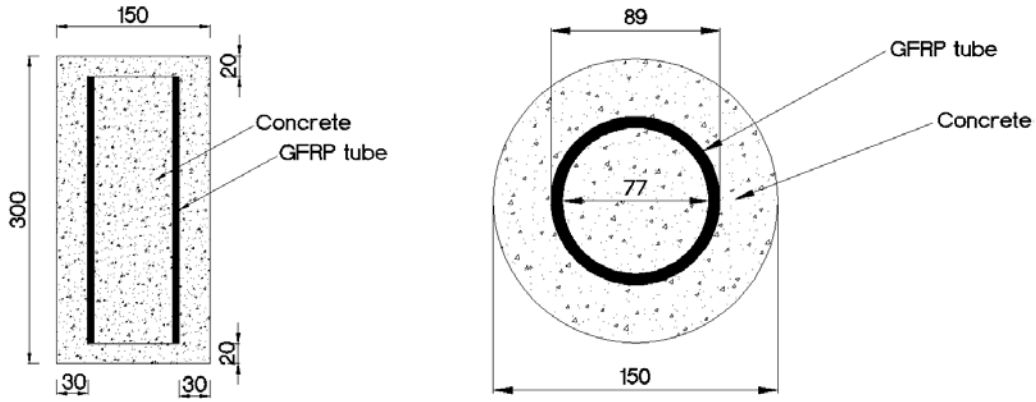

(a) elevation section (b) cross-section

Figure 3.2 FTRC specimens (dimensions are in mm) (Hadi et al. 2015)

Table 3.1 lists the specimens tested in this study. Group REF specimens were used as reference specimens which contain no reinforcement. Group ST specimens were reinforced with solid GFRP tube. Group APT and DPT specimens were reinforced with APT and DPT, respectively. For Group ST-LW, APT-LW, and DPT-LW specimens, laterally wrapped ST, APT, and DPT, respectively, were used as reinforcement. The number within the bracket indicates one of the two identical specimens in each group.

Table 3.1 Test matrix in Chapter 3

Specimens	Description	Reinforcement
REF-(1,2)	Plain specimens	None
ST-(1,2)	FTRC specimens	Solid GFRP tube
APT-(1,2)		Axially perforated GFRP tube
DPT-(1,2)		Diagonally perforated GFRP tube
ST-LW-(1,2)		CFRP wrapped solid GFRP tube
APT-LW-(1,2)		CFRP wrapped axially perforated GFRP tube
DPT-LW-(1,2)		CFRP wrapped diagonally perforated GFRP tube

3.2.2 Preparation of specimens

3.2.2.1 Tube perforation and CFRP attachment

For the perforated GFRP tubes, hole locations were marked before drilling. A drill press machine with a 25 mm circular drill bit was used to perforate the tubes. Gloves and a mask were worn to get protected from harmful fibres during the perforation operation. A water spray bottle was used to wash away any waste material. After perforation, GFRP tubes labelled ST-LW, APT-LW, and DPT-LW were laterally wrapped with two layers of CFRP sheets. A mixture of epoxy resin and hardener at 5:1 ratio was used. Before the application of the first layer of CFRP, the adhesive was spread onto the surface of the tube. After the first layer, the adhesive was spread onto the first layer of CFRP and the second layer was continuously bonded. 70 mm overlap was maintained. All wrapped GFRP tubes were left to dry for seven days.

3.2.2.2 Casting of specimens

Plastic moulds were used to cast the concrete specimens. The moulds were made of PVC pipes with 150 mm inner diameter and 300 mm height. GFRP tubes were placed into the mould first. In order to ensure a 20 mm concrete cover at the top and bottom, three tiny holes were drilled into the timber base as well as at the bottom of GFRP tubes. The holes were 10 mm in depth. Afterwards, three 40 mm long thin steel wires were inserted into the holes to support the GFRP tubes and to maintain 20 mm concrete cover. The steel wires were removed from the concrete specimens after curing of concrete. To ensure 30 mm cover at sides, four thin steel wires were aligned symmetrically around the top end of GFRP tube. The steel wires were removed after two thirds of the concrete had been cast. Each mould was stabilized vertically by three galvanized steel straps and two hose clips. Figure 3.3 shows the layout of GFRP tubes in the moulds.

(a) 20 mm cover at bottom (b) 30 mm cover on the sides

Figure 3.3 Layout of GFRP tubes (Hadi et al. 2015)

After GFRP tube was placed into the mould, concrete was mixed and cast. A wet hessian was placed over the specimen to prevent moisture loss. All the specimens were watered during weekdays until the test date. To prevent premature failure, the top and the bottom of the specimen were strengthened by two layers of CFRP sheets. 70 mm overlapping was applied at the top and the bottom of the specimen. Figure 3.4 shows the GFRP tube reinforced concrete specimen.

(a) before concrete casting

(b) after concrete casting

Figure 3.4 GFRP tube reinforced concrete (FTRC) specimen (Hadi et al. 2015)

3.2.3 Preliminary test

Concrete cylinders with 100 mm diameter and 200 mm height were tested for compressive strength at 28 days. The average compressive strength at 28 days was 35 MPa. The properties of CFRP sheet were determined by FRP coupon tests accordance to ASTM D7565/D7565M (2010). The average width of the coupons was 28.50 mm and the average maximum tensile force was 1200 N/mm. The average ultimate tensile strain was calculated as 0.0172 mm/mm.

Properties of GFRP tubes were determined by tube axial compression test. Six GFRP tubes, with one tube for each type, were tested under axial compression. Figure 3.5 shows the axial load-axial deformation diagram of GFRP tubes under axial compression. Table 3.2 lists the ultimate load and the corresponding axial deformation of GFRP tubes. For solid GFRP tube, the average ultimate axial compressive strength was 400 MPa and the corresponding axial strain was 0.014 mm/mm. The axial elastic modulus was 33 GPa, which was close to the value provided by the manufacturer (35.4 GPa). It is evident that perforations significantly reduce the axial stiffness and load carrying capacity of GFRP tubes. Even though less perforation was created for DPT, the ultimate load and the corresponding axial deformation were less than those of APT, which indicates that APT performs better than DPT under axial compression. Moreover, wrapping the CFRP sheet did not significantly improve the ultimate load and the corresponding deformation of the tubes. Figure 3.6 shows the failure modes of different GFRP tubes after axial compression test. Tubes ST and ST-LW failed due to stress concentration at the tube end, while perforated GFRP tubes failed due to the rupture around holes.

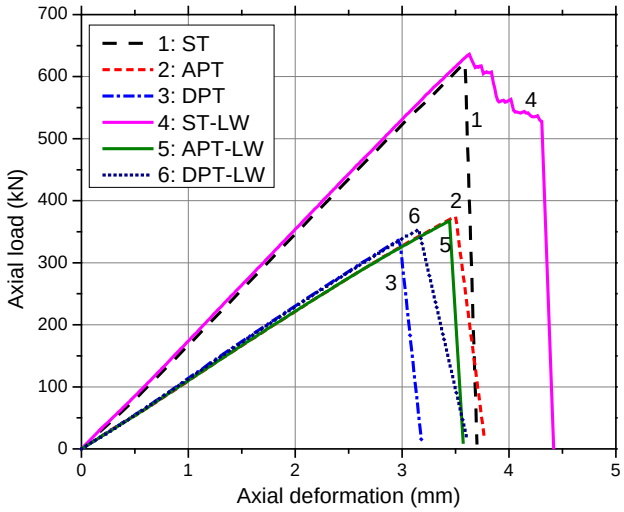

Figure 3.5 Axial load-axial deformation behaviour of GFRP tubes (Hadi et al. 2015)

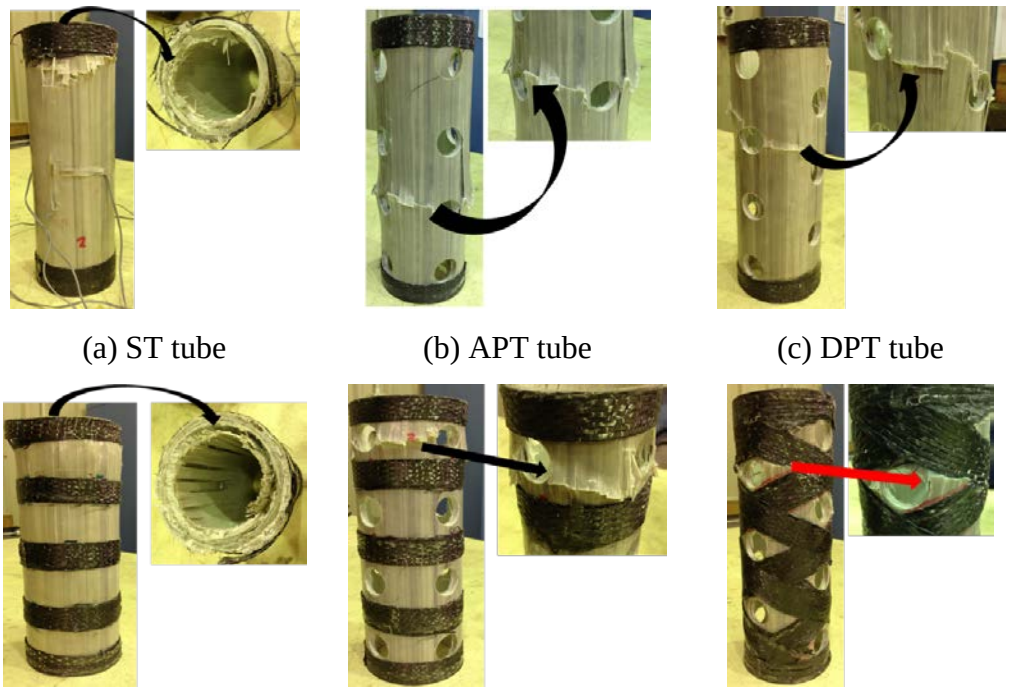

(a) ST tube (b) APT tube (c) DPT tube

(d) ST-LW tube (e) APT-LW tube (f) DPT-LW tube

Figure 3.6 Failure modes of GFRP tubes under axial compression (Hadi et al. 2015)

Table 3.2 Results of tube compression test

Tube type	ST	APT	DPT	ST-LW	APT-LW	DPT-LW
Ultimate load (kN)	624	375	337	636	367	353
Corresponding axial deformation (mm)	3.58	3.5	2.98	3.63	3.44	3.16

3.2.4 Instrumentation and test procedure

Strain gauges were longitudinally and transversely attached onto the GFRP tubes to investigate the actual strain at representative locations. Two pairs of strain gauges were used for each column in Groups ST, APT and DPT. Each pair contains two strain gauges attached at mid-height of the GFRP tube aligned in the longitudinal and transverse directions. Two representative locations were selected for perforated tubes. The first location (Point A) was in the middle of two neighbouring holes, and the second location (Point B) was in the intact part of GFRP tubes, as shown in Figure 3.7. For each column in Groups ST-LW, APT-LW, and DPT-LW, two strain gauges were attached onto the CFRP sheet to capture the tensile strains of CFRP sheet in the mid-height of GFRP tubes.

(a) ST (b) APT (c) DPT (d) ST-LW (e) APT-LW (f) DPT-LW

Figure 3.7 Locations of strain gauges in GFRP tubes (Hadi et al. 2015)

The Denison 5000 kN testing machine in the High Bay laboratory at the University of Wollongong, Australia, was used for testing all the specimens. Before testing, all specimens were capped at the top end with high strength plaster to ensure uniform load application. The specimens were placed vertically on the steel plate. Adequate care was taken to ensure that the specimens were placed at the centre of the testing machine. Axial deformations were measured using two Linear Variable Differential Transformers (LVDTs), which were mounted at the corners between the loading plate and the supporting steel plate. The deformation readings from the two LVDTs were then averaged to obtain representative results. The load and deformation data

were recorded using an electronic data-logger connected to a computer for every two seconds. The displacement controlled tests were carried out at a rate of 0.5 mm/min. All specimens were tested until failure.

3.3 Experimental results and discussion

3.3.1 Failure modes

All reinforced specimens failed in a brittle manner with rupture of GFRP tubes. Typical failure modes of the specimens are shown in Figure 3.8. The failure modes depend largely on the configuration of GFRP tubes. Group ST and Group ST-LW specimens failed due to the transverse rupture and in-plane shear at the mid-height of the GFRP tubes. For specimens in Group APT and Group APT-LW, longitudinal rupture was observed around the holes. Group DPT specimens failed due to longitudinal rupture in the middle of three neighbouring holes, while Group DPT-LW specimens failed due to the rupture around the holes where CFRP was not attached.

(a) ST (b) APT (c) DPT (d) ST-LW (e) APT-LW (f) DPT-LW

Figure 3.8 Failure modes of FRTC specimens (Hadi et al. 2015)

3.3.2 Axial load-axial deformation behaviour

Figure 3.9 shows the axial load-axial deformation behaviour of Groups REF, ST, APT and DPT specimens. It can be seen that all specimens showed similar behaviour before yielding. Afterwards, specimens reinforced with GFRP tubes showed decrease in the strength with increase in the deformation. This behaviour is attributed to the spalling of concrete cover. It is noted that the concrete cover was 30 mm at the sides and hence significant decrease in the strength of the specimens was expected.

Afterwards, the strength of the specimens was increased with the increase in the axial deformation because of the confining effect provided by GFRP tubes. Eventually, all the specimens failed due to the rupture of the GFRP tubes, accompanied by very loud noises. It is evident from Figure 3.9 that several fluctuations occurred before total failure. These fluctuations suggest that even after the rupture of GFRP tubes, specimens can still sustain considerable amount of load because of the contribution of concrete. Figure 3.10 shows the axial load-axial deformation behaviour of Groups REF, ST-LW, APT-LW, and DPT-LW specimens. Groups ST-LW, APT-LW, and DPT-LW specimens show similar behaviour to those of Groups ST, APT, and DPT specimens, respectively. It is noted that for Column ST-LW-2, the deformation at ultimate load was 8.26 mm, which was even lower than that of Group ST specimens. However, from the tube compression test, it was predicted that ST-LW specimens should have a higher ultimate load and the corresponding axial deformation than those of Group ST specimens. This inconsistency may be attributed to operating error during the test. Therefore, the test result of Column ST-LW-2 has not been considered for further analyses.

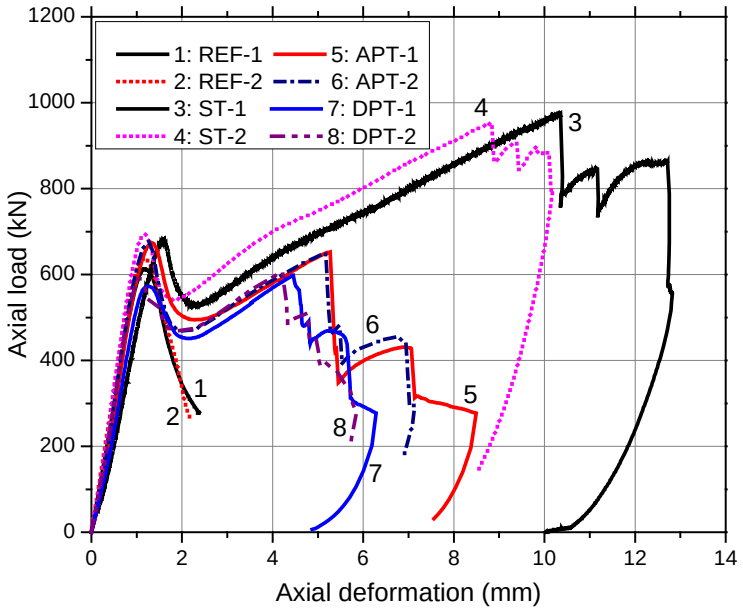

Figure 3.9 Axial load-axial deformation behaviour of REF, ST, APT and DPT specimens (Hadi et al. 2015)

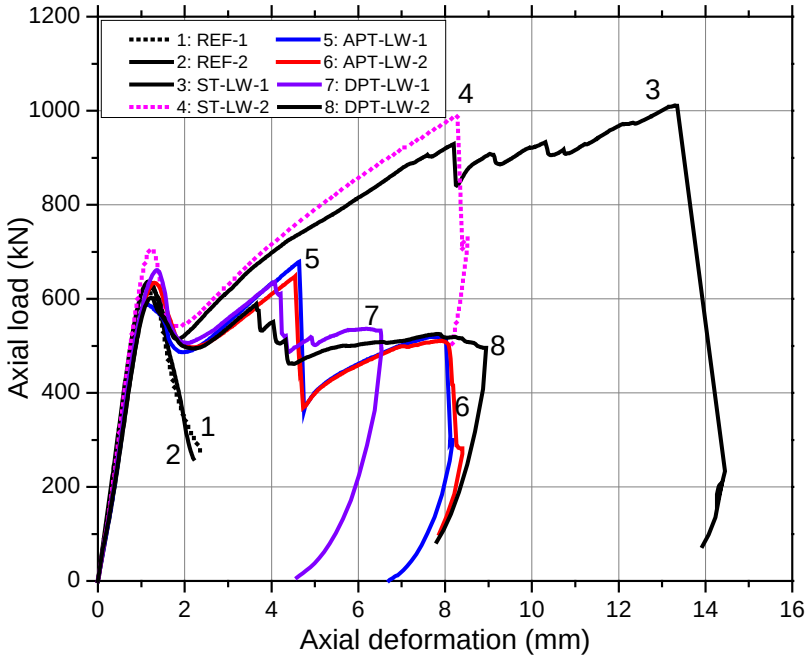

Figure 3.10 Axial load- axial deformation behaviour of REF, ST-LW, APT-LW and DPT-LW specimens (Hadi et al. 2015)

The test results of all specimens are summarized in Table 3.3. The yield load (P_y), the ultimate load (P_u) as well as the corresponding axial deformations have been presented. In this study, the ultimate load is defined as the load at the rupture of FRP tube. The ductility of the specimens has been calculated as:

$$\mu = \frac{\delta_u}{\delta_y} \qquad 3.1$$

where μ is the ductility of the specimen, δ_u is the deformation at the ultimate load, and δ_y is the deformation at the yield load.

It can be seen from Table 3.3 that Groups ST and ST-LW specimens show significant increase in both the load carrying capacity and the ductility. Group ST-LW specimens achieved the highest load carrying capacity and ductility. For perforated GFRP tube reinforced concrete specimens in Groups APT, APT-LW, DPT, and DPT-LW, the ultimate load and ductility increased while the increase was less than those of Groups ST and ST-LW specimens. There might be two reasons for such behaviour. First, compared to 77 mm diameter concrete core, the spalling of 30

mm concrete cover would obviously result in a significant strength loss. Second, the perforation produced a strength reduction for the GFRP tubes, as explained above. For Groups APT and APT-LW specimens, the ultimate load and the ductility were higher than those of Groups DPT and DPT-LW specimens, respectively. The lowest ultimate loads and ductility capacities were observed for Group DPT-LW specimens. The results indicate that the axially perforated GFRP tube (APT) performs better than the diagonally perforated GFRP tube (DPT) in reinforcing the specimens.

Table 3.3 Summary of test results

Specimen	P_y (kN)	δ_y (mm)	P_u (kN)	δ_u (mm)	μ
REF-1	613	1.18	613	1.18	1.00
REF-2	637	1.19	637	1.19	1.00
ST-1	680	1.59	975	10.34	6.50
ST-2	694	1.19	953	8.84	7.43
APT-1	674	1.32	653	5.27	4.00
APT-2	677	1.26	651	5.17	4.10
DPT-1	573	1.26	598	4.45	3.53
DPT-2	592	1.04	607	4.22	4.06
ST-LW-1	624	1.24	1011	13.33	10.75
APT-LW-1	588	1.15	679	4.64	4.03
APT-LW-2	634	1.29	648	4.54	3.52
DPT-LW-1	661	1.37	636	4.07	2.97
DPT-LW-2	602	1.23	589	3.65	2.97

It is also important to note that the axial deformation at ultimate load for Group APT-LW specimens is lower than that of Group APT specimens. This can be explained by the fact that the wrapping of CFRP sheet onto the intact part of APT tubes might have resulted in the development of more minor cracks around the holes. Hence, APT-LW tube experienced a premature rupture around the holes than APT tube. Similarly, for Group DPT-LW specimens, though a majority of the tube was wrapped with CFRP sheet, there were still areas around the holes that were not protected by CFRP sheet, and the rupture occurred around the unwrapped areas.

Therefore, the attachment of CFRP sheet was insignificant in improving the load carrying capacity and the ductility of Group DPT-LW specimens. Nevertheless, the comparison between Group ST specimens and Group ST-LW specimens shows that the attachment of CFRP sheet onto solid GFRP tube may improve the load carrying capacity and the ductility of Group ST-LW specimens, because the CFRP sheet could potentially confine the lateral expansion of solid GFRP tube.

Table 3.4 shows the confinement effects of GFRP tubes. P_u indicates the ultimate load of the specimens, P_{c0} indicates the unconfined concrete strength times the area of the concrete core, P_f indicates the ultimate load of the GFRP tubes. The $(P_{c0} + P_f)$ represents the ultimate load of the specimens without confinement. It can be seen that the load carrying capacity of FTRC specimens exceed the load carrying capacity of the two individual materials. The GFRP tubes significantly improved the load carrying capacity of the specimens. Even though the perforation adversely reduced the axial elastic modulus and strength of GFRP tubes, the confinement effect did not show significant difference.

Table 3.4 Confinement effects of GFRP tubes

Specimens	P_u	P_f	P_{c0}	$\frac{P_c}{P_{c0}+P_f}$
ST	964	624	156	1.24
APT	652	375		1.23
DPT	605	337		1.23
ST-LW	1011	636		1.27
APT-LW	664	367		1.27
DPT-LW	613	353		1.20

3.3.3 Axial deformation-volumetric strain behaviour

In order to understand the dilatation behaviour of concrete core, the axial deformation-volumetric strain response was calculated from the recorded strain gauge data. The volumetric strain ε_v is determined from (Samaan et al. 1998):

$$\varepsilon_v = \varepsilon_c + \varepsilon_h \quad (3.2)$$

where ε_c and ε_h are the axial strain and hoop strain, respectively. In this study, the axial compressive strains are considered negative and the hoop tensile strains are considered positive. Hence, a positive ε_v means dilation and a negative ε_v means volume contraction.

It has been reported that the volumetric change of FRP confined concrete depends significantly on the amount of FRP (Teng and Lam 2004). If the concrete was confined by a relatively less amount of FRP, the concrete may exhibit volumetric dilation at failure. However, if the concrete was confined by a sufficient amount of FRP, the concrete may not show dilation at all. Figure 3.11 shows the axial displacement-volumetric strain response for Groups ST, APT and DPT specimens. Group ST specimens exhibited a continuous contraction, which indicates the efficiency of confinement provided by GFRP tube. For Group APT specimens, the strain gauges measurement at the intact part (Point B) as well as around the hole area (Point A) were used to calculate the volumetric strain. The locations of Point A and Point B are shown in Figure 3.7. It can be seen that the volumetric strain at the intact part (Point B) of APT exhibited a slight contraction initially followed by a slight dilation. Finally the specimen failed with a large volumetric contraction at Point B. On the contrary, the volumetric strain around hole area (Point A) experienced a continuously increasing volume dilation until failure after slight volume contraction at the beginning. For Group DPT specimens, the volumetric strain at the intact part (Point B) experienced a continuous volumetric contraction until the final failure, while the volumetric strain around the hole area (Point A) was subjected to contraction first and continuous dilation afterwards. The difference in volumetric strains between different parts of perforated GFRP tube indicates that the intact part is more effective in confining the concrete.

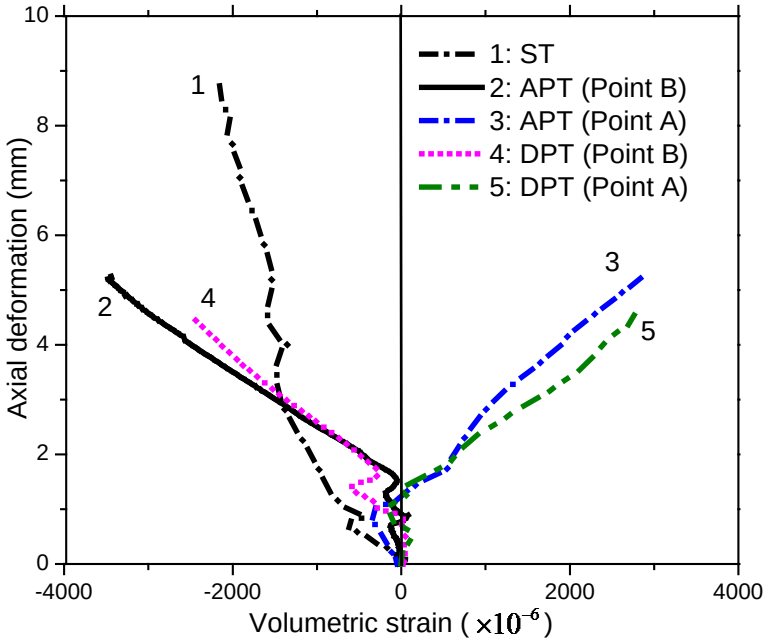

Figure 3.11 Axial deformation-volumetric strain behaviour of FTRC specimens (Hadi et al. 2015)

3.4 Numerical simulations

Finite element simulations of FTRC specimens under axial compression were carried out to investigate the effect of hole diameter and hole spacing on the strength and the ductility of specimens. The numerical simulation considers the complexities of the concrete nonlinearity, the orthotropic properties of the GFRP tubes, and the confinement effect of GFRP tubes. The simulation model has been validated with the experimental result presented in this chapter.

3.4.1 Modelling method

The nonlinear concrete model was used to simulate the concrete behaviour. In the concrete model, the stress-strain relationship of the concrete in compression exhibits nearly linear elastic response up to about 30% of the concrete compressive strength, which is followed by plastic behaviour until the compressive strength of concrete is reached. Beyond the compressive strength, the concrete stress-strain relationship exhibits strain softening until crushing. Figure 3.12 (a) shows the idealized uniaxial stress-strain curve for the concrete and Figure 3.12 (b) shows the biaxial failure

surface of the concrete. The stress-strain relationship for concrete in tension is assumed to follow a linear ascending branch with a slope that is equal to the concrete modulus of elasticity (E_c) until maximum tensile stress (σ_t) is reached. In this study, the smeared crack model, in which it is assumed that a plane of failure is developed perpendicular to the corresponding principal stress direction, is used. The normal and the shear stiffness across the plane of failure are reduced and plane stress conditions are assumed to exist at the plane of tensile failure. Poisson's ratio (v) is considered as 0.2. The tangent modulus of concrete at zero strain (E_0) is considered as 26 GPa. The unconfined concrete compressive strength is considered as 35 MPa with a corresponding strain of 0.002.

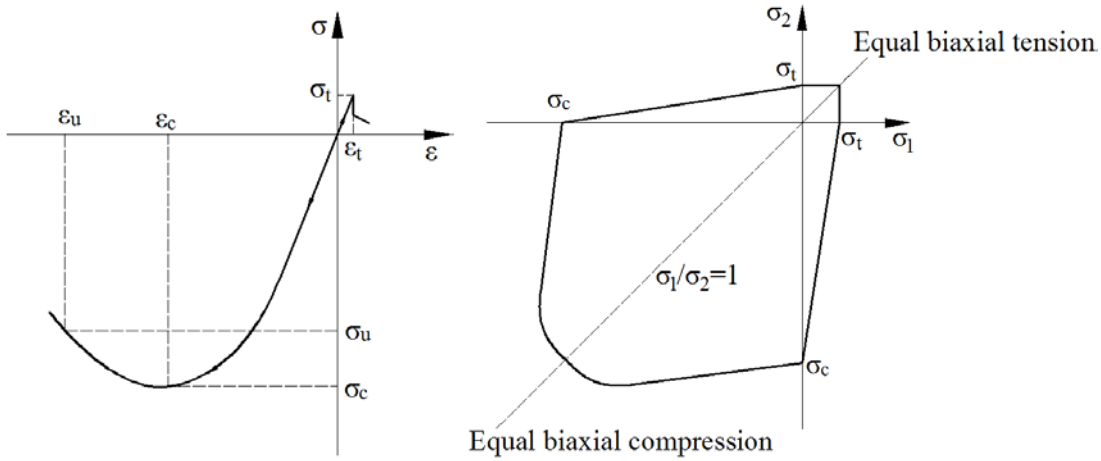

(a) Typical uniaxial stress-strain curve (b) Biaxial failure envelope

Figure 3.12 Constitutive model for concrete (Hadi et al. 2015)

The orthotropic material model was used to simulate GFRP tubes. Orthotropic material properties used in the simulation are shown in Table 3.5. It can be seen from Table 3.5 that the ultimate tensile strength, ultimate compressive strength, and elastic modulus in the longitudinal direction are much higher than the ultimate tensile strength, ultimate compressive strength and elastic modulus in transverse direction, respectively. The higher values in the longitudinal direction can be attributed to the manufacturing method of the GFRP tubes used in this study. During the pultrusion process, a vast proportion of the glass fibres were aligned along the longitudinal direction of the GFRP tubes.

3-D solid elements were used to represent the concrete and FRP tubes. Each element contains 10 nodes, and each node has three degrees of freedom. In order to improve the convergence, the modelling techniques adopted are: (a) application of compatible element mode, (b) selection of higher numerical integration order, (c) adoption of the displacement convergence criterion, and (d) application of automatic time stepping (ATS) method. The birth/death element was used to simulate the spalling of concrete cover. After the concrete cover element was set to death, the concrete cover was assumed to be spalled off and was not considered for subsequent calculations. Displacement was applied on the top end of the specimen, and the loading speed was set to 0.005 mm/s.

Table 3.5 Mechanical properties of GFRP tubes used in simulation (Wagners CFT 2015)

Property	Value
Longitudinal Tensile Strength (MPa)	650
Transverse Tensile Strength (MPa)	41
Longitudinal Compressive Strength (MPa)	550
Transverse Compressive Strength (MPa)	104
Shear Strength (MPa)	84
Longitudinal Elastic modulus (GPa)	35.4
Transverse Elastic modulus (GPa)	12.9

3.4.2 Validation of the model

The modelling method was validated with experimental results. Since it has been proven that APT specimens exhibit higher strength and ductility than DPT specimens, APT specimens were modelled. ST specimens were modelled as well.

Figure 3.13 (a, b) show the comparison of simulation result and experimental result of axial strain-axial load response of ST specimen and APT specimen, respectively. It is noted that the axial strain was obtained at the mid-height of GFRP tube. It can be seen that both the test and simulation results show very similar behaviour under axial compressive loading. The simulation results underestimate the load carrying capacity

of the specimen especially beyond the cover spalling, which indicates that the strength enhancement of concrete core may not have been fully reflected. Nonetheless, the finite element model predicts the ultimate load carrying capacity and the ultimate strain, which are the main parameters of investigation in this study, with a reasonable accuracy.

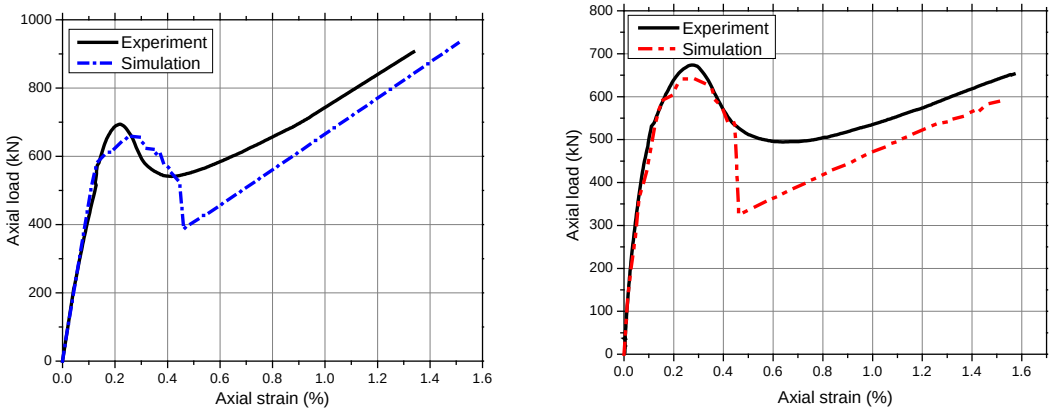

(a) Specimen ST (b) Specimen APT

Figure 3.13 Comparison between experimental results and simulation results (Hadi et al. 2015)

3.4.3 Effect of hole diameter

The effect of hole diameter on the strength and the ductility of specimens was investigated by using the developed finite element model. Four hole diameters (0 mm, 15 mm, 21 mm, 28 mm) were considered. The vertical hole spacing for all perforated GFRP tubes was 40 mm. Other simulation parameters were kept as before. Figure 3.14 shows the axial load-axial strain diagram of specimens reinforce by GFRP tubes with different hole diameters. It is evident that the reduction of hole diameter increases the load carrying capacity of concrete specimens, although axial strains at ultimate loads are very similar. Figure 3.15(a) represents GFRP tube with 15 mm hole diameter and Figure 3.15(b) represents GFRP tube with 28 mm hole diameter. It can be seen from Figure 3.15 that by reducing the hole diameter, more intact part of tube can be obtained, thus a higher load carrying capacity can be achieved. Also, by reducing the hole diameter, more concrete core can be effectively confined with GFRP tube, which can result in a higher strength improvement for concrete core. Therefore, it can be assumed that the strength of FTRC specimens is

highly dependent on the hole diameters of the perforated GFRP tubes. It is also evident that 25 mm hole diameter is very large for GFRP tube with 89 mm outer diameter to maintain the load carrying capacity of the specimens.

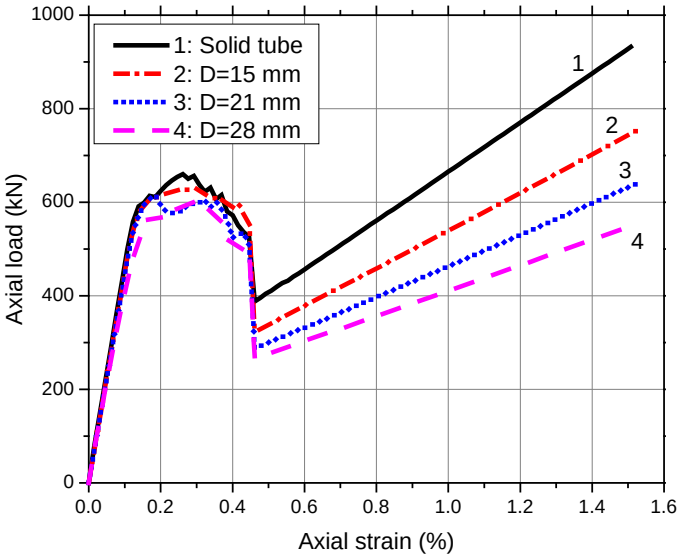

Figure 3.14 Effect of hole diameter on the axial load-axial strain behaviour of APT specimens (Hadi et al. 2015)

(a) hole diameter=15 mm (b) hole diameter=28 mm

Figure 3.15 Distribution of effective stress in perforated tubes: (a) hole diameter= 15 mm, and (b) hole diameter= 28 mm (Hadi et al. 2015)

3.4.4 Effect of vertical hole spacing

The effect of vertical hole spacing was investigated by simulating GFRP tube reinforced concrete specimens with three different vertical hole spacings (25 mm, 50

mm, 75 mm). The hole diameter for all perforated GFRP tubes was 15 mm. Other simulation parameters were kept as before. The axial strain - axial load responses of specimens are shown in Figure 3.16. It can be seen that the load carrying capacity increases with the increase in hole spacing, although axial strains at ultimate loads are very similar. By increasing the hole spacing, more concrete core can be effectively confined, which results in a higher strength improvement of concrete core. In addition, larger hole spacing means less perforation, which can also enable specimens to sustain higher load (Figure 3.17). Therefore, it can be assumed that the strength of FTRC specimens also depends on the vertical hole spacing of the perforated GFRP tubes. However, the influence of vertical hole spacing is less than the influence of hole diameter on the load carrying capacity of FTRC specimens.

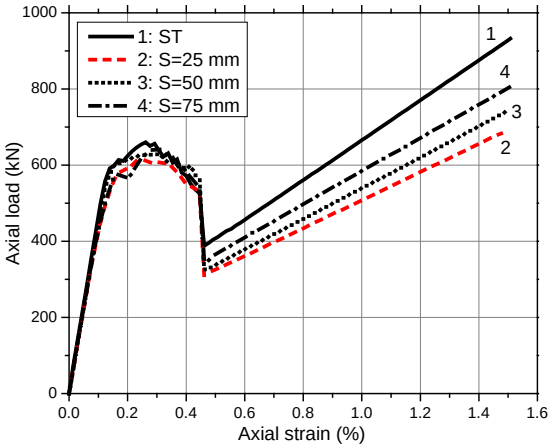

Figure 3.16 Effect of vertical hole spacing on the axial load-axial strain behaviour of APT specimens (Hadi et al. 2015)

Based on the simulation result, higher strength of FTRC specimens can be obtained by reducing the hole diameter instead of increasing the vertical hole spacing of perforated GFRP tubes. Similarly, the vertical hole spacing can be reduced without causing significant strength degradation of FTRC specimens where increased perforation area is required.

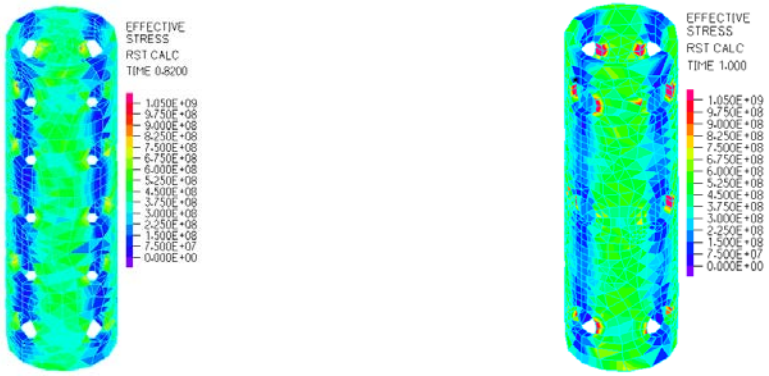

(a) hole spacing=25 mm (b) hole spacing=75 mm

Figure 3.17 Distribution of effective stress in perforated tubes: (a) hole spacing= 25 mm and (b) hole spacing= 75 mm (Hadi et al. 2015)

Even though perforation may influence the performance of FTRC specimens under axial compression, it is essential to prevent the premature cover spalling in the design of FTRC specimens. When FTRC specimens are exposed to high temperature, the concrete cover spalling may occur for specimens reinforced with intact FRP tubes because the bonding between concrete cover and FRP tube may decrease significantly due to the high pressure induced by water vapour inside concrete (Aydın et al. 2008). On the other hand, in presence of holes, even though the bonding between concrete cover and FRP tube may decrease under high temperature, the mechanical interlocking between concrete core and cover may remain highly effective in preventing the cover from spalling. Moreover, the presence of holes on the FRP tube increases the bonding strength between concrete core and FRP tube (Ji et al. 2009).

3.5 Conclusions

Experimental investigations and numerical finite element simulations were carried out to study the axial compressive behaviour of FRP tube (solid and perforated) reinforced concrete (FTRC) specimens. Based on the experimental and simulation results, the following conclusions can be drawn:

(1) FTRC specimens are effective in increasing the strength and the ductility of concrete specimens under axial compression. Concrete specimens reinforced with

laterally wrapped solid GFRP tubes (ST-LW) achieved the highest strength and ductility than the other groups of specimens in this study;

(2) The use of perforated GRRP tubes is mainly to integrate the concrete core and concrete cover, which is essential to protect the concrete cover from premature spalling (e.g., due to fire or impact loading). However, the perforation may result in the loss of strength and the ductility of FTRC specimens;

(3) The numerical simulation results show that reduction of the hole diameter or increase of vertical hole spacing can be effective in increasing the strength and the ductility of FTRC specimens. However, as the reduction of hole diameter is more effective, it is suggested that hole diameter be reduced rather than the vertical hole spacing be increased for the design of FTRC specimens; and

(4) FTRC specimens may be utilized in building and other applications where strict fire performance and impact load resistance are necessary and where traditional RC specimens are located in aggressive environment which may lead to corrosion of steel reinforcement.

The research results presented in this study indicate that tube perforations can significantly influence the performance of Type I FTRC columns. Therefore, before further understanding of the proposed Type I FTRC columns, the behaviour of perforated FRP tube should be fully understood. Chapter 4 thus presents detailed experimental and analytical investigations on the axial compressive behaviour of perforated FRP tubes.

4 BEHAVIOUR OF PERFORATED GFRP TUBES UNDER AXIAL COMPRESSION

4.1 Introduction

In Chapter 3, perforated FRP tubes have been used to provide both longitudinal and transverse reinforcements for Type I FTRC columns. Due to the presence of holes on FRP tubes, the continuous distributions of stress and strain are interrupted, which leads to the performance degradation of FRP tubes. Considering limited knowledge from previous investigations, an experimental program was carried out to investigate the axial compressive behaviour of perforated GFRP tubes. The influences of hole diameter, vertical hole spacing, tube diameter, perforation pattern, transverse hole spacing, and hole reinforcement on the axial compressive behaviour of perforated GFRP tubes were experimentally investigated. Moreover, design-oriented equations have been developed to predict the axial stiffness, axial critical load and axial deformation of perforated GFRP tubes under axial compression.

4.2 Experimental program

A total of 15 GFRP tubes with and without perforations were tested under axial compression in the High Bay Civil Engineering Laboratory at the University of Wollongong, Australia. The GFRP tubes were divided into two groups: Group A contains 12 GFRP tubes with 89 mm outer diameter and 6 mm wall thickness and Group B contains 3 GFRP tubes with 183 mm outer diameter and 8 mm wall thickness (Figure 4.1). The height of Group A GFRP tubes was 260 mm, while the height of Group B GFRP tubes was 185 mm. For Group A GFRP tubes, the influences of hole diameter, vertical hole spacing, perforation pattern, transverse hole spacing, and hole reinforcement on the axial compressive behaviour of perforated GFRP tubes were investigated. For Group B GFRP tubes, the influence of hole diameter was investigated. The influence of tube diameter was investigated by comparing test results of Group A and Group B GFRP tubes.

(a) Group A tube (b) Group B tube

Figure 4.1 Intact GFRP tubes (Wang et al. 2015b)

4.2.1 Properties of test materials

Group A GFRP tubes were manufactured by Wagners Composite Fibre Technology (CFT) based in Toowoomba, Queensland, Australia (Wagners CFT 2015). Group B GFRP tubes were manufactured by Exel Composites Australia based in Boronia, Victoria, Australia (Exel Composites Australia 2015). The GFRP tubes were pultruded tubes made from vinyl ester resin systems with E-glass fibre. According to the information provided by the manufacturer, Type A pultruded GFRP tubes had an overall E-glass fibre content of 76%. Starting from the exterior of the tube wall, the stacking sequence of the laminates was in the form of [0°/+45°/0°/-45°/0°/-45°/0°/45°/0°], where the 0° coincided with the longitudinal axis of the tube. The thickness of each ply was the same. The laminate stacking sequence of Type B pultruded GFRP tube was not available due to commercial confidentiality of the manufacturer. The mechanical properties of GFRP tubes provided by the manufacturers are listed in Table 4.1. It can be seen from Table 4.1 that the ultimate tensile strength, ultimate compressive strength, and elastic modulus in the longitudinal direction are much higher than the ultimate tensile strength, ultimate compressive strength and elastic modulus in the transverse direction, respectively. The higher values in the longitudinal direction can be explained by the fact that a large proportion of the glass fibres were aligned along the longitudinal direction of the GFRP tubes during the pultrusion process.

Table 4.1 Mechanical properties of GFRP tubes (Exel Composites Australia 2015; Wagners CFT 2015)

Property	Tube A	Tube B
Longitudinal Tensile Strength (MPa)	650	450
Transverse Tensile Strength (MPa)	41	50
Longitudinal Compressive Strength (MPa)	550	450
Transverse Compressive Strength (MPa)	104	80
Shear Strength (MPa)	84	25
Longitudinal Elastic modulus (GPa)	35.4	30
Transverse Elastic modulus (GPa)	12.9	10

4.2.2 Test parameters

The influences of hole diameter (15 mm and 25 mm), vertical hole spacing (40 mm, 60 mm and 100 mm), tube diameter (89 mm and 183 mm outer diameter), perforation patterns, transverse hole spacing, and hole reinforcement on the axial compressive behaviour of perforated GFRP tubes were investigated in this experimental program. Two different perforation patterns (axially perforated tubes have been designated as APT and diagonally perforated tubes have been designated as DPT) were investigated, as shown in Figure 4.2 (a) and (b). The transverse hole spacing was varied by changing the number of holes around the transverse direction of the tubes (3 and 4 holes). For perforated GFRP tubes with hole reinforcement, 3 layers of Carbon Fibre Reinforced Polymer (CFRP) sheet were wrapped around holes. Different reinforcement configurations were applied for APT and DPT tubes. The detailed configurations of the FRP tubes are shown in Figure 4.2 (c) and (d).

(a) APT (b) DPT (c) APT-LW (d) DPT-LW

Figure 4.2 Perforated GFRP tubes (Wang et al. 2015b)

4.2.3 Test specimens

4.2.3.1 Description of test specimens

The details of the GFRP tubes are given in Table 4.2. The labelling of GFRP tubes has been carried out as: (a) “A” and “B” are used to identify Group A GFRP tubes and Group B GFRP tubes, respectively; (b) “I” indicates intact GFRP tubes without perforation; (c) for perforated GFRP tubes, “D” and the number afterwards indicate the diameter of the hole in mm, “V” and the number afterwards indicate the vertical hole spacing in mm, “T” and the number afterwards indicate the number of holes around transverse direction; (d) “LW” represents that the GFRP tube was laterally wrapped with CFRP; (e) “APT” represents axially perforated GFRP tube and (f) “DPT” represents diagonally perforated GFRP tube.

4.2.3.2 Procedure of tube perforation

Before perforation, the exact locations of the holes were marked. Afterwards, a drill press machine with a circular drill bit was used to perforate the tubes. Gloves and mask were worn to get protected from harmful fibres during the perforation process. A water spray bottle was used to wash away any waste material. For GFRP tubes wrapped with CFRP, three layers of CFRP were laterally wrapped before tube perforation. Prior to the wrapping of CFRP, the surface of GFRP tube was cleaned to remove all the dust that may affect the wrapping quality. The 105 epoxy resin and 206 slow hardener manufactured by West System were used in this study

(WestSystem 2015). A mixture of epoxy resin and hardener at a ratio of 5:1 was used as the adhesive. The CFRP was wrapped onto the GFRP tube manually using a wet lay-up method. No tension force was applied during the wrapping process. Before wrapping of the first layer of CFRP, the adhesive was spread onto the surface of the GFRP tube. After the first layer of CFRP was wrapped, the adhesive was spread onto the first layer of CFRP and the second layer was continuously wrapped. The third layer of CFRP was wrapped in a similar manner. A 70 mm overlap was maintained to prevent the premature debonding of CFRP. The epoxy resin was then left to cure at room temperature for seven days.

4.2.4 Instrumentation and test procedure

The Denison 5000 kN testing machine was used for testing all the GFRP tubes. Before testing, a horizontal level was used to adjust the bottom steel plate to ensure that the surface of the bottom steel plate was horizontal. Afterwards, the tube was placed onto the bottom steel plate to check whether there was any misalignment between the tube end and the bottom steel plate. If no misalignment was observed, then the tube end was considered to be horizontal and parallel to the bottom steel plate. However, if a slight misalignment was observed, the tube end was slightly smoothed using a belt sander until the misalignment was removed. The same procedure was applied to the other tube end. Afterwards, a vertical level was used to ensure that both tube ends were perpendicular to the longitudinal axis of the tube. When the tube ends were horizontal and perpendicular to the longitudinal axis of the tube, and the surfaces of steel plates were horizontal, then the load can be considered to be applied in a purely axial manner. Axial deformations were measured using two Linear Variable Differential Transducers (LVDTs) mounted at the opposite corners of the steel plate. The load and deformation data were collected using an electronic data-logger at 2 second intervals. The test (displacement controlled) was conducted at a rate of 0.3 mm/min. All GFRP tubes were tested until failure. The test setup and instrumentation are shown in Figure 4.3.

Table 4.2 Details of GFRP tubes

GFRP tube	Hole diameter (mm)	Vertical hole spacing (mm)	Number of holes around transverse direction	Reinforcement
A-I	None	None	None	None
A-D25-V40-T4(APT)	25	40	4	None
A-D25-V40-T4 (DPT)	25	40	4	None
A-D25-V40-T4-LW (DPT)	25	40	4	Yes
A-D25-V60-T4 (APT)	25	60	4	None
A-D25-V60-T4-LW (APT)	25	60	4	Yes
A-D25-V100-T4 (APT)	25	100	4	None
A-D25-V60-T3 (APT)	25	60	3	None
A-D25-V60-T3 (DPT)	25	60	3	None
A-D15-V60-T4 (APT)	15	60	4	None
A-D15-V60-T3 (APT)	15	60	3	None
A-D15-V100-T3 (APT)	15	100	3	None

Table 4.2 Continued

B-I	None	None	None	None
B-D25-V60-T3 (APT)	25	60	3	None
B-D15-V60-T3 (APT)	15	60	3	None

Note: “A” and “B” are used to identify Group A GFRP tubes and Group B GFRP tubes, respectively; “I” indicates intact GFRP tubes without perforation; for perforated GFRP tubes, “D” and the number afterwards indicate the diameter of the hole in mm; “V” and the number afterwards indicate the vertical hole spacing in mm; “T” and the number afterwards indicate the number of holes around transverse direction; “LW” represents that the GFRP tube was laterally wrapped with CFRP sheet; “APT” indicates axially perforated GFRP tube; and “DPT” represents diagonally perforated GFRP tube.

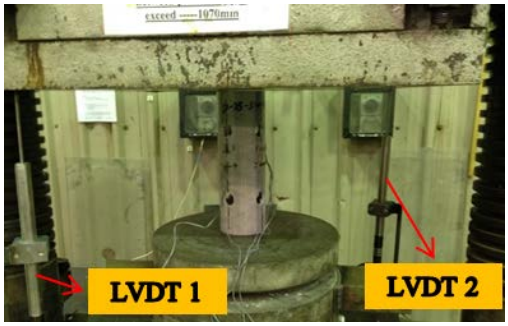

Figure 4.3 Test setup and instrumentation (Wang et al. 2015b)

In order to prevent the premature failure at the tube end, a specially designed test fixture was manufactured and used. The test fixture was composed of a steel flange and a steel sleeve, as shown in Figure 4.4 (a) and (b). By combining these two components together, a groove can be developed to constrain the tube ends (Figure 4.4 (c)). In order to prevent the upper steel sleeve from slippage, the upper steel sleeve was fixed onto the upper steel flange using three bolts (Figure 4.4 (d)). The engineering drawings of these two components are shown in Figure 4.5. After the test fixture was capped onto the tube ends, the same procedures mentioned above were followed to ensure that the load was applied in a purely axial manner.

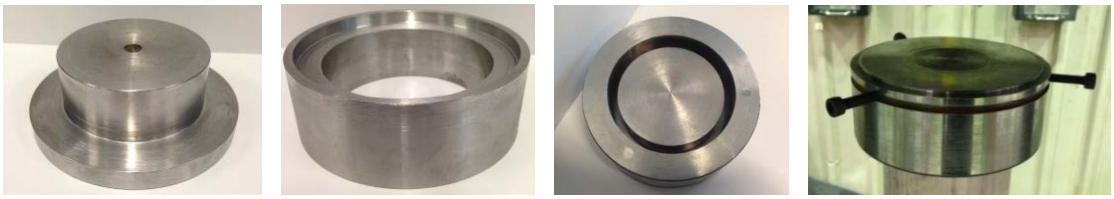

(a) steel flange (b) steel sleeve (c) combination (d) upper test fixture with bolts

Figure 4.4 Details of test fixture (Wang et al. 2015b)

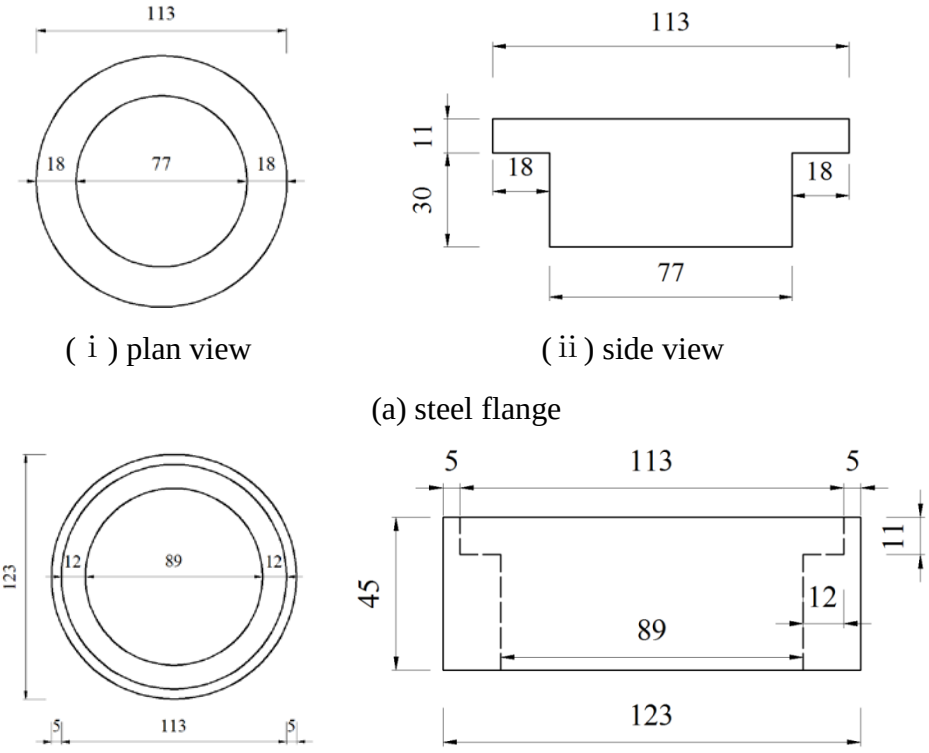

(i) plan view (ii) side view

(a) steel flange

(i) plan view (ii) side view

(b) steel sleeve

Figure 4.5 Engineering drawings of test fixture (Wang et al. 2015b)

4.3 Experimental results and discussion

4.3.1 Failure modes of GFRP tubes

All tested GFRP tubes failed in a brittle manner because of the non-ductile characteristics of the fibres and epoxy resin. For intact Group A GFRP Tube “A-I” without capping the test fixture, failure was caused due to the stress concentration phenomenon at the tube end, which resulted in a lower compressive strength than the actual compressive strength (Figure 4.6 (a)). However, by capping the test fixture onto the tube ends, a global collapse was observed for Tube “A-I” (Figure 4.6 (b)). Therefore, it is evident that by using the developed test fixture, the stress concentration at the tube ends can be effectively eliminated and the actual compressive strength can be obtained. For intact Group B GFRP Tube “B-I”, global collapse was observed after the axial compressive strength was reached. The failure of perforated GFRP tubes was initiated with crack formation around the holes due to severe local stress concentration. Initially cracking noise was heard. The cracking

noise increased with the increase of axial compressive load. The crack formation was followed by a sudden drop of the axial compressive load, with the splitting of the fibres around holes accompanied by a loud noise. After splitting, the fibres were bent and curled outwards, extensively delaminated, and fractured transversely and longitudinally around the holes. It is noted that longitudinal rupture was more serious than the transverse rupture. This is mainly because GFRP tubes were manufactured by pultrution with majority of fibres aligned in the longitudinal direction. The failure modes of perforated GFRP tubes depend largely on the perforation patterns. For axially perforated GFRP tubes, rupture was observed around holes at the same height (Figure 4.6 (c)). For diagonally perforated GFRP tubes, the tubes failed due to crack development in the middle of three neighbouring holes (Figure 4.6 (d)). For perforated GFRP tubes with reinforced holes, the failure modes were similar to those of perforated GFRP tubes without hole reinforcement (Figure 4.6 (e)).

4.3.2 Axial load-axial deformation behaviour of GFRP tubes

A summary of the test results which include axial stiffness ratio κ (axial stiffness ratio between perforated tubes and intact tubes), axial critical load ratio η (axial critical load ratio between perforated tubes and intact tubes), and axial deformation ratio λ (axial deformation ratio between perforated tubes and intact tubes) are given in Table 4.3. The axial stiffness for intact Group A GFRP tube was 166 kN/mm, while the axial stiffness for intact Group B GFRP tube was 700 kN/mm. The axial load-axial deformation diagrams of both intact and perforated GFRP tubes are presented in the following sections. Both intact and perforated GFRP tubes show linear axial load-axial deformation behaviour until the sudden collapse of the tubes. Considerable decreases in the axial stiffness, axial critical load, and axial deformation capacity were observed due to the perforation, as explained below.

(a) A-I (without capping test fixture)

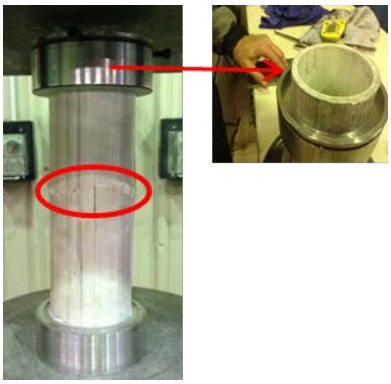

(b) A-I (with capping test fixture)

(c) A-D15-V100-T3 (APT)

(d) A-D25-V60-T3 (DPT)

(e) A-D25-V60-T4-LW (APT)

Figure 4.6 Failure modes of GFRP tubes (Wang et al. 2015b)

4.3.2.1 Influence of hole diameter

Figure 4.7 illustrates the axial load-axial deformation behaviour of intact GFRP tube and perforated GFRP tubes with different hole diameters. The effect of hole diameter was investigated by drilling 15 mm and 25 mm diameter holes while keeping the other parameters constant. In Figure 4.7 (a), for perforated GFRP Tube "A-D25-V60-T4 (APT) " (with 25 mm diameter holes), 29.1%, 49.1%, and 27.8% reductions in the axial stiffness, axial critical load, and corresponding deformation, respectively, were observed compared to those of intact GFRP tube. For perforated GFRP Tube "A-D15-V60-T4 (APT)" (with 15 mm diameter holes), 18.2%, 36.1%, and 21.6% reductions were observed in the axial stiffness, axial critical load, and corresponding deformation, respectively, compared to those of intact GFRP tube. In Figure 4.7 (b), the reductions of axial stiffness, axial critical load, and corresponding deformation

were 13.6%, 28.2%, and 17.1%, respectively, for perforated GFRP Tube “B-D25-V60-T3 (APT)” (with 25 mm diameter holes), while the corresponding reductions were 9.1%, 14.8%, and 6.3%, respectively, for perforated GFRP Tube “B-D15-V60-T3 (APT)” (with 15 mm diameter holes). Therefore, by reducing the hole diameter, the axial stiffness, axial critical load, and axial deformation capacity could be significantly increased. These results are slightly different from the results reported in Taheri-Behrooz et al. (2012). In Taheri-Behrooz et al. (2012), hole diameters of 2.5 mm, 10 mm, and 15 mm were used to numerically investigate the influence of hole diameter on the load carrying capacity of perforated tubes. Since the hole diameters in Taheri-Behrooz et al. (2012) were relatively small compared to the diameter of the tubes (107.3 mm inner diameter), the influence of the hole diameter was not significant. However, the influence of hole diameter on the performance of perforated GFRP tubes under axial compression cannot be neglected especially for perforated GFRP tubes with larger holes.

The variation of local deformation was analysed by investigating the strain distributions at representative locations for perforated GFRP Tube “A-D25-V60-T4 (APT)”. In this study, the strain gauges were attached onto locations away from the perforations to investigate how perforation can influence the strain distributions at locations away from the perforations. Two representative locations were selected. The first location (Point A) was in the middle of two vertical neighbouring holes and the second location (Point B) was in the intact part of GFRP tube, as shown in Figure 4.8 (a). Figure 4.8 (b) shows the distribution of strains. It can be seen from Figure 4.8 (b) that the axial strain at the intact part was two times of hoop strain at the intact part (Point B). The axial and hoop strains obtained at the intact part (Point B) were 10 and 5 times of those of axial and hoop strains obtained in between two vertical neighbouring holes (Point A), respectively. Therefore, it is evident that the major part of the tubes that carries the axial compressive load is the intact vertical segment of the tube without any holes. This observation can be used to explain that perforated tubes with smaller hole diameter have higher axial critical load under axial compression. Moreover, it is reasonable to expect that when the perforated tubes

were subject to internal pressure, the major parts in resisting the hoop tensile load are the intact segments in the hoop direction of the tube.

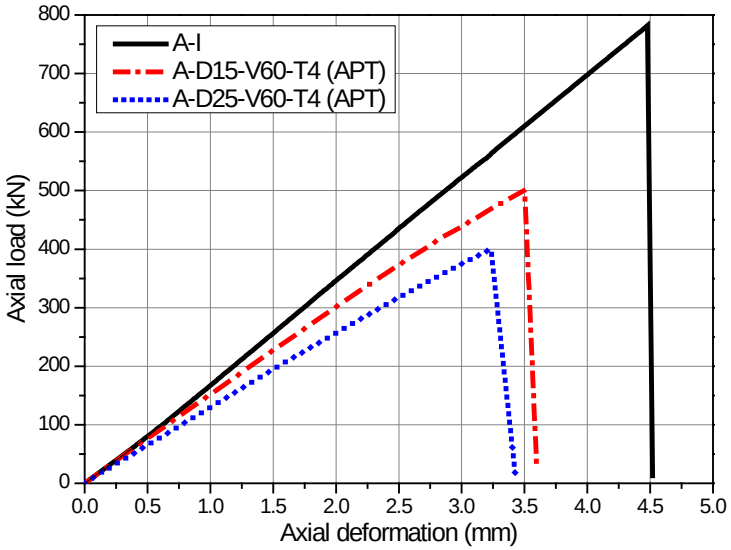

(a) Axial load-axial deformation behaviour of A-I, A-D15-V60-T4 (APT) and A-D25-V60-T4 (APT)

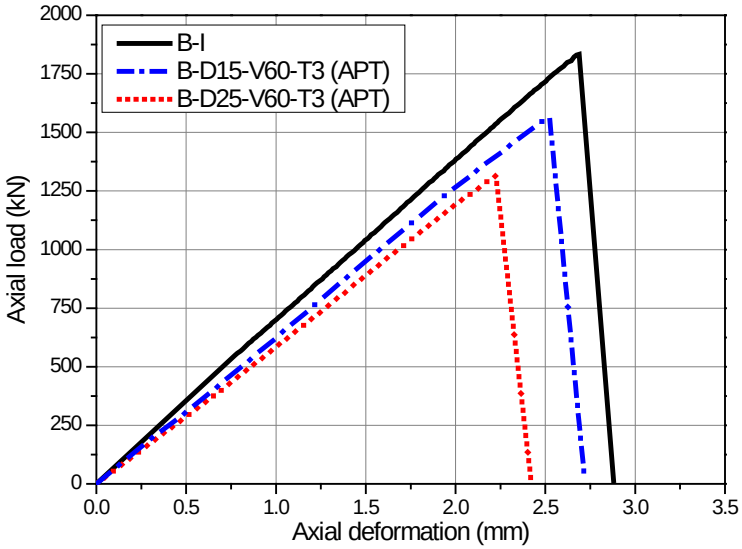

(b) Axial load-axial deformation behaviour of B-I, B-D15-V60-T3 (APT) and B-D25-V60-T3 (APT)

Figure 4.7 Influence of hole diameter on the axial compressive behaviour of perforated GFRP tubes (Wang et al. 2015b)

Table 4.3 Experimental results of perforated GFRP tubes

GFRP tube	Perforation ratio ν	ξ	Axial stiffness ratio κ	Axial deformation ratio λ	Axial critical load ratio η
A-I	0	0	1	1	1
A-D25-V40-T4 (DPT)	0.384	3.06	0.652	0.665	0.431
A-D25-V40-T4-LW (DPT)	0.384	3.06	0.652	0.694	0.452
A-D25-V40-T4 (APT)	0.384	3.06	0.6	0.799	0.479
A-D25-V40-T4-LW (APT)	0.384	3.06	0.6	0.779	0.469
A-D25-V60-T4 (APT)	0.384	3.06	0.709	0.722	0.509
A-D25-V60-T4-LW (APT)	0.384	3.06	0.688	0.734	0.504
A-D25-V100-T4 (APT)	0.384	3.06	0.758	0.717	0.541
A-D25-V60-T3 (APT)	0.288	2.295	0.767	0.741	0.566
A-D25-V60-T3 (DPT)	0.288	2.295	0.715	0.583	0.416

Table 4.3 Continued

A-D15-V60-T4 (APT)	0.230	1.836	0.818	0.784	0.639
A-D15-V60-T3 (APT)	0.173	1.377	0.885	0.794	0.699
A-D15-V100-T3 (APT)	0.173	1.377	0.921	0.799	0.733
B-I	0	0	1	1	1
B-D15-V60-T3 (APT)	0.082	0.832	0.909	0.937	0.852
B-D25-V60-T3 (APT)	0.136	1.386	0.864	0.829	0.718

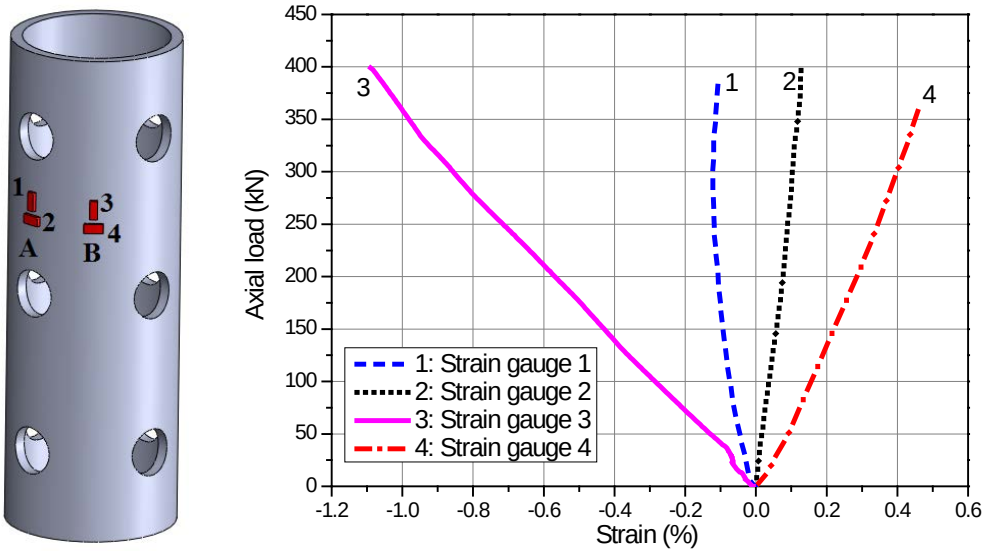

(a) Strain gauges location (b) Strain distribution

Figure 4.8 Strain distributions at different locations of GFRP Tube "A-D25-V60-T4 (APT)" (Wang et al. 2015b)

4.3.2.2 Influence of vertical hole spacing

The axial load-axial deformation diagrams shown in Figure 4.9 are used to illustrate the influence of vertical hole spacing on the axial compressive behaviour of perforated GFRP tubes. Vertical hole spacing of 60 mm and 100 mm were investigated. All other parameters were kept constant. In Figure 4.9, the increases in the axial stiffness, axial critical load, and corresponding axial deformation with the increase in the vertical hole spacing from 60 mm (A-D25-V60-T4 (APT)) to 100 mm (A-D25-V100-T4 (APT)) were 6.8%, 6.3%, and 6.2%, respectively. Similarly, in Figure 4.9 (b), the increases in the axial stiffness, axial critical load, and corresponding deformation with the increase in the vertical spacing from 60 mm (A-D15-V60-T3 (APT)) to 100 mm (A-D15-V100-T3 (APT)) were 4.1%, 4.8%, and 5.6%, respectively. Therefore, by increasing the vertical hole spacing, the axial stiffness, axial critical load, and axial deformation capacity can be increased. However, the increase is not highly significant (within 4%-7%).

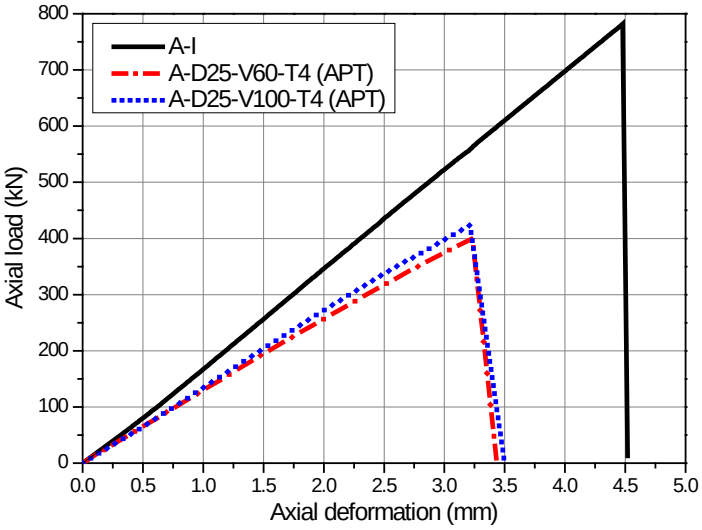

(a) Axial load-axial deformation behaviour of A-I, A-D25-V60-T4 (APT) and A-D25-V100-T4 (APT)

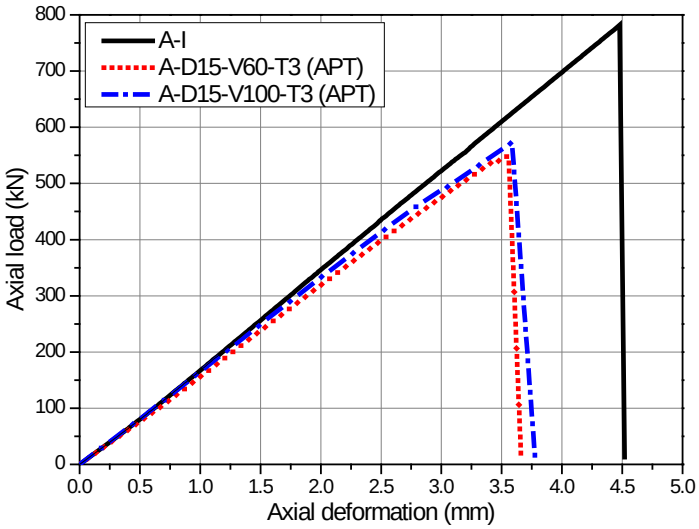

(b) Axial load-axial deformation behaviour of A-I, A-D15-V60-T3 (APT) and A-D15-V100-T3 (APT)

Figure 4.9 Influence of vertical hole spacing on the axial compressive behaviour of perforated GFRP tubes (Wang et al. 2015b)

The strain distributions between two vertical holes as well as at the intact part were investigated for perforated GFRP Tube "A-D25-V100-T4 (APT)". Figure 4.10 (a) shows the layout of strain gauge and Figure 4.10 (b) shows the axial strain distributions. It can be seen from Figure 4.10 (b) that the axial strain at Point B is only one third of the axial strain at Point A. This indicates that the closer the distance

between holes, the less the axial strain can be obtained. Both the axial strains between two vertical holes (Point A and Point B) are much less than the axial strain at the intact part (Point C). Therefore, the vertical part between two neighbouring vertical holes contributes little to the performance of perforated GFRP tube under axial compression. It is noted that the axial strains obtained between two vertical holes increase nonlinearly with the axial load. This nonlinear behaviour is more obvious for Point B which is closer to the holes. It might be due to the fact that the fibres around holes were cut and damaged because of the perforation, which disturbed the linear properties of fibre bundles. Therefore, it can be reasonably argued that perforated GFRP tubes with a relatively small vertical hole spacing may not cause significant performance degradation under axial compression. However, this argument may not be applicable for perforated GFRP tubes with very small vertical hole spacing because the minor cracks around closely spaced neighbouring vertical holes can easily develop into a fatal crack, which may result in an earlier tube failure.

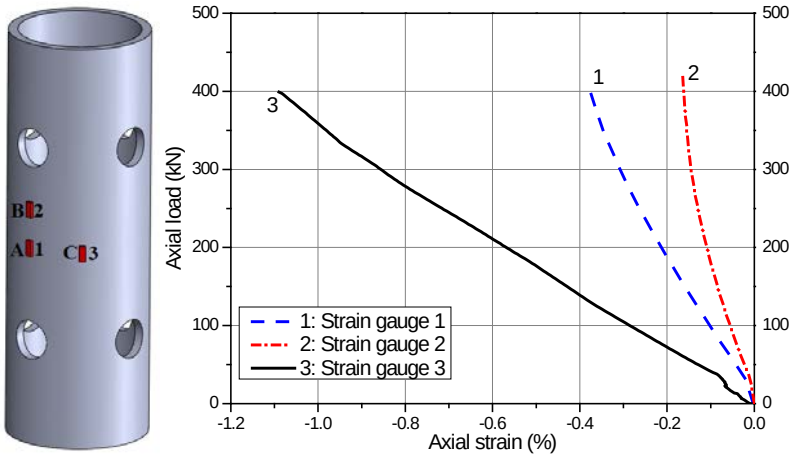

(a) Strain gauges layout (b) Strain distribution

Figure 4.10 Axial strains distributions at different locations of GFRP Tube "A-D25-V100-T4 (APT)" (Wang et al. 2015b)

4.3.2.3 Influence of tube diameter

The influence of tube diameter is investigated by comparing test results obtained from Group A and Group B GFRP tubes. The major difference between Group A and Group B tubes was the tube diameter (89 mm and 183 mm outer diameter). Figure

4.11 (a) and (b) illustrate axial load-axial deformation diagrams of perforated GFRP tubes with different tube diameters. For comparison purpose, the axial load and axial deformation of GFRP tubes are normalised with respect to the axial critical load and corresponding deformation of intact GFRP tubes, respectively. In Figure 4.11 (a), for Tube "A-D25-V60-T3 (APT)", the perforation leads to the reductions of 23.3%, 43.4%, and 25.9% in the axial stiffness, axial critical load, and corresponding deformation, respectively. However, the reductions were 13.6%, 28.2%, and 17.1%, respectively, for Tube "B-D25-V60-T3 (APT)". Similarly, in Figure 4.11 (b), reductions of 11.5%, 30.1%, and 20.6% in the axial stiffness, axial critical load, and corresponding deformation were observed for Tube "A-D15-V60-T3 (APT)", and the corresponding reductions for Tube "B-D15-V60-T3 (APT)" were 9.1%, 14.8%, and 5.3%. Therefore, it is clear that when other parameters are kept constant, increasing the tube diameter can improve the performance of perforated GFRP tubes under axial compression.

4.3.2.4 Influence of perforation pattern

Figure 4.12 presents a comparison of axial load-axial deformation behaviour between axially perforated GFRP tube (APT) and diagonally perforated GFRP tube (DPT). In Figure 4.12 (a), for diagonally perforated Tube "A-D25-V60-T3 (DPT)", the axial stiffness, axial critical load, and corresponding deformation were 93.3%, 73.4%, and 78.6%, respectively, of those of axially perforated Tube "A-D25-V60-T3 (APT)". Furthermore, for Tube "A-D25-V40-T4 (DPT)" in Figure 4.12 (b), the axial stiffness, axial critical load, and corresponding deformation were 108.6%, 89.9%, and 83.2%, respectively, compared to those of Tube "A-D25-V40-T4 (APT)". Interestingly, even though more holes were perforated on axially perforated tubes, better performance than diagonally perforated tubes under axial compression is observed. This may be explained that for diagonally perforated GFRP tubes, the cracks between neighbouring holes are easier to develop into a fatal crack, and hence the rupture is more likely to occur at an early stage. Based on the above investigation, it is recommended that perforated GFRP tubes with axial perforation pattern should be selected in order to improve the axial compressive behaviour.

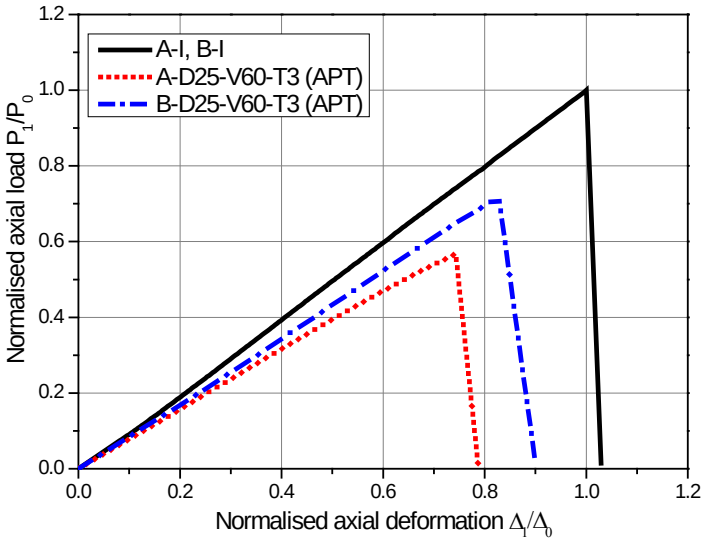

(a) Normalised axial load-axial deformation behaviour of A-I, B-I, A-D25-V60-T3 (APT) and B-D25-V60-T3 (APT)

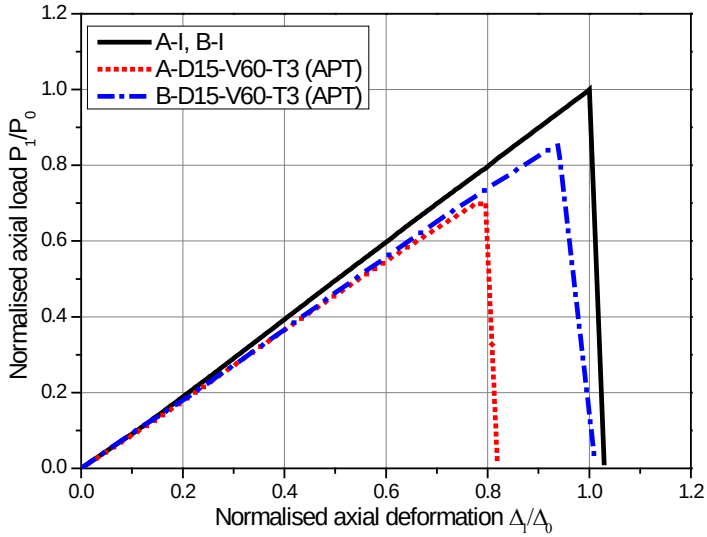

(b) Normalised axial load-axial deformation behaviour of A-I, B-I, A-D15-V60-T3 (APT) and B-D15-V60-T3 (APT)

Figure 4.11 Influence of tube diameter on the axial compressive behaviour of perforated GFRP tubes (Note: P_0 and P_1 indicate the axial loads of intact and perforated FRP tubes, respectively; Δ_0 and Δ_1 indicate the axial deformations of intact and perforated FRP tubes, respectively) (Wang et al. 2015b)

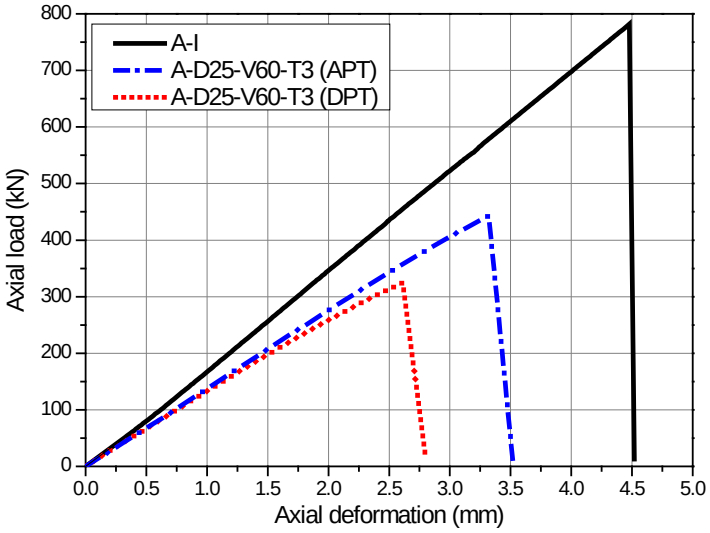

(a) Axial load-axial deformation behaviour of A-I, A-D25-V60-T3 (APT) and A-D25-V60-T3 (APT)

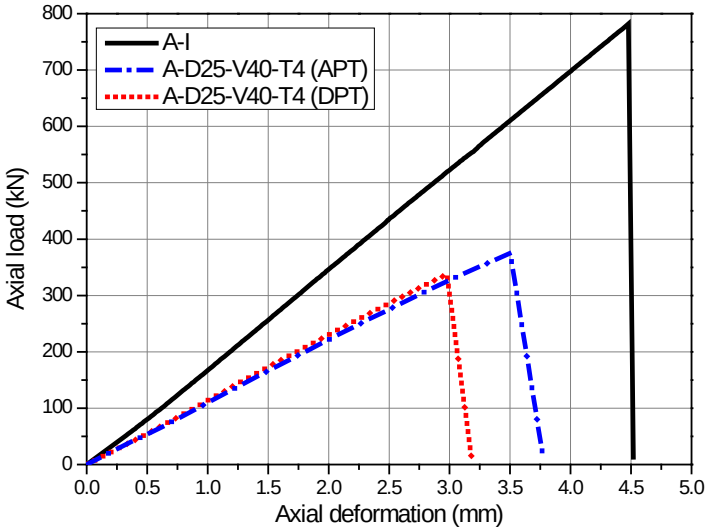

(b) Axial load-axial deformation behaviour of A-I, A-D25-V40-T4 (APT) and A-D25-V40-T4 (APT)

Figure 4.12 Influence of perforation pattern on the axial compressive behaviour of perforated GFRP tubes (Wang et al. 2015b)

4.3.2.5 Influence of transverse hole spacing

Figure 4.13 illustrates the influence of transverse hole spacing on the axial compressive behaviour of perforated GFRP tubes. The variation of transverse hole spacing was investigated by changing the number of holes around the tube transverse direction. The less the number of holes around tube transverse direction, the larger

the transverse spacing between holes. The perforated tubes with three and four holes around tube transverse direction were tested under axial compression while the other parameters were kept constant. Figure 4.13 (a) and (b) illustrate that the axial stiffness and the axial critical load increases significantly with the increase of transverse hole spacing. However, the corresponding deformations at axial critical load do not show significant differences. Compared to the test results presented in Sections 4.3.2.1-4.3.2.5, it can be inferred that increase of perforation around tube transverse direction can lead to a significant decrease in the performance of perforated GFRP tube under axial compression. However, increase of perforation around tube longitudinal direction may not significantly influence the performance. Therefore, it is recommended that with a fixed perforation area throughout the tube, the perforation along the transverse direction can be reduced while the perforation along the longitudinal direction can be increased in order to improve the axial compressive behaviour of perforated GFRP tubes.

4.3.2.6 Influence of hole reinforcement

Reinforcement can be applied around holes so that the axial compressive behaviour of perforated cylindrical shells may be improved (Almroth and Holmes 1972; Cervantes and Palazotto 1979; Toda 1983). In this study, 3 layers of CFRP sheet were wrapped around the holes to investigate whether this type of reinforcement could be effective in improving the performance of perforated GFRP tubes under axial compression. Figure 4.2 (c) and (d) provide the specific layout of reinforcement for both axially and diagonally perforated GFRP tubes. Figure 4.14 shows the axial load-axial deformation behaviour of perforated tubes with reinforced or unreinforced holes. Both reinforced and unreinforced perforated tubes show similar behaviour under axial compression. The performance improvement is not significant for perforated tubes with reinforced holes. Nevertheless, it may be reasonable to expect that CFRP wrapping around holes would be effective for perforated GFRP tubes subjected to internal pressure for which significant transverse tensile strain may occur.

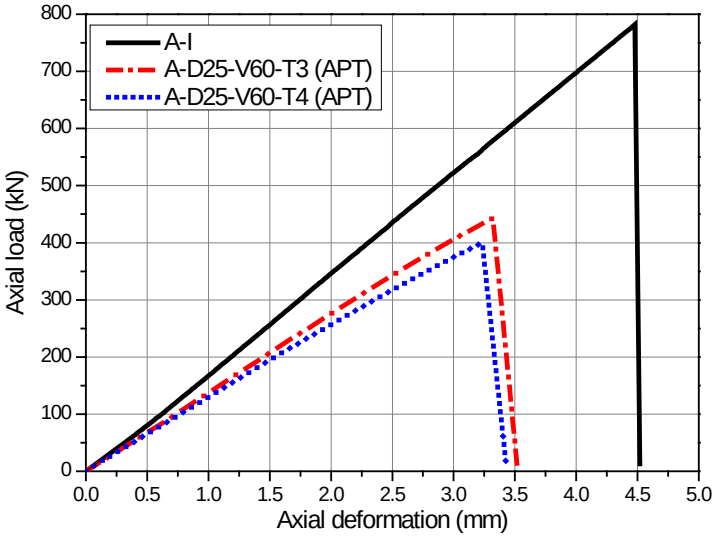

(a) Axial load-axial deformation behaviour of A-I, A-D25-V60-T3 (APT) and A-D25-V60-T4 (APT)

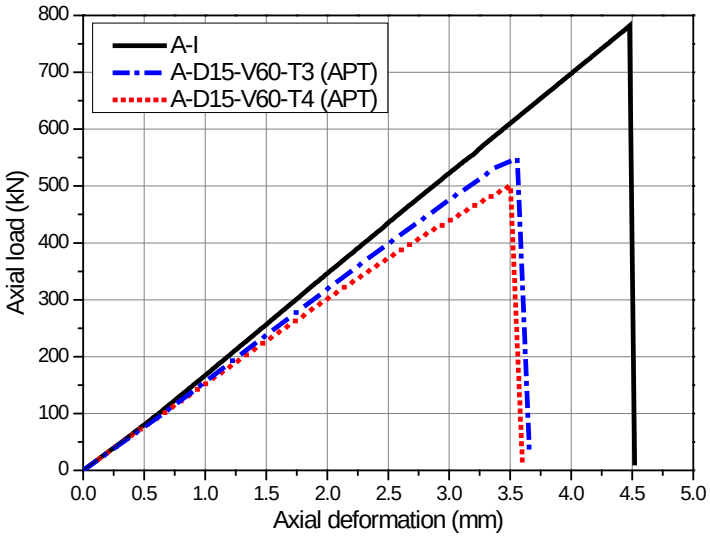

(b) Axial load-axial deformation behaviour of A-I, A-D15-V60-T3 (APT) and A-D15-V60-T4 (APT)

Figure 4.13 Influence of transverse hole spacing on the axial compressive behaviour of perforated GFRP tubes (Wang et al. 2015b)

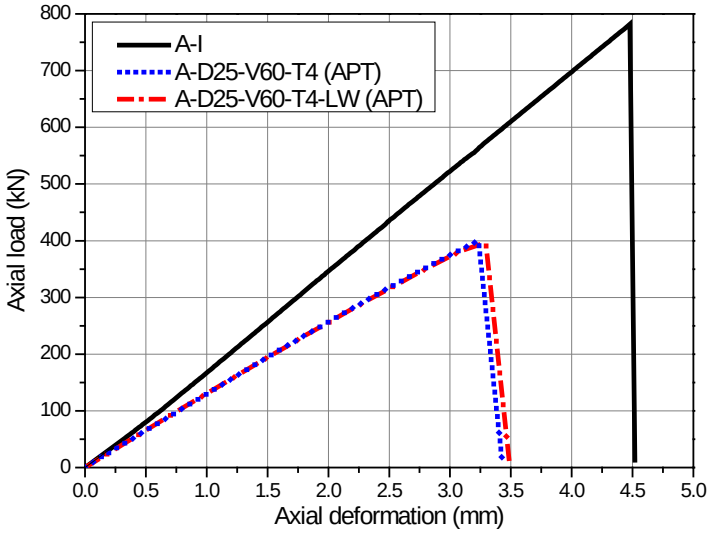

(a) Axial load-axial deformation behaviour of A-I, A-D25-V60-T4 (APT) and A-D25-V60-T4-LW (APT)

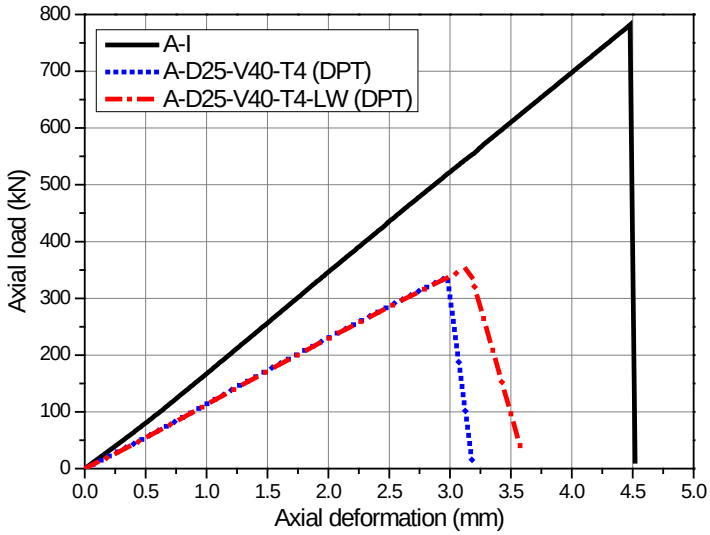

(b) Axial load-axial deformation behaviour of A-I, A-D25-V40-T4 (DPT) and A-D25-V40-T4-LW (DPT)

Figure 4.14 Influence of hole reinforcement on the axial compressive behaviour of perforated GFRP tubes (Wang et al. 2015b)

4.4 Development of design-oriented equations

This section aims to develop design-oriented equations to characterise the axial stiffness, axial critical load, and axial deformation capacity of perforated GFRP tubes under axial compression. The equations contain the main parameters that influence

the axial compressive behaviour of perforated GFRP tubes. The proposed equations were validated by the collected experimental database. For the development of design-oriented equations, few basic assumptions are adopted: (1) the major parts in resisting the axial compressive load are the vertical intact segment of the perforated GFRP tubes; (2) the influence of vertical hole spacing on the axial compressive behaviour is not significant; and (3) the axial deformation capacity is decreased because of the perforation. All the assumptions are in accordance with the experimental observations presented in Section 4.3.

4.4.1 Definitions of model parameters

Two parameters are introduced herein. The first parameter is perforation ratio, which is defined as the ratio between the sum of perforation length around tube transverse direction and the perimeter of the GFRP tube:

$$\nu = \frac{nd}{\pi\left(D_i + t_f\right)} \tag{4.1}$$

where ν is perforation ratio; D_i, d, and t_f are the inner diameter, hole diameter, tube thickness of GFRP tube, respectively; and n is the number of holes around tube transverse direction. The less perforation ratio ν, the more intact vertical segment without holes for perforated GFRP tubes.

A parameter ξ has been used to characterise the behaviour of perforated cylindrical shells under axial compression (Toda 1983; Gupta and Gupta 1993). In this study, the parameter ξ is used to investigate the axial compressive behaviour of perforated GFRP tubes. Since ξ is only suitable for perforated tubes with one hole, in order to make ξ suitable for perforated tubes with multiple holes, Equation 4.2 has been proposed herein:

$$\xi = \frac{n \cdot d}{2\sqrt{R_o t_f}} \tag{4.2}$$

where R_o is the outer radius of the tube.

4.4.2 Available experimental data

Taheri-Behrooz et al. (2012) investigated the axial compressive behaviour of perforated GFRP tubes. Details of the test data in Taheri-Behrooz et al. (2012) can be found in Table 4.4. The parameters in the database include the radius of GFRP tubes R_o, tube thickness t_f, perforation ratio ν, parameter ξ, axial stiffness ratio κ, axial critical load ratio η, and axial deformation ratio λ. It should be noted that all perforated tubes were diagonally perforated GFRP tubes in Taheri-Behrooz et al. (2012).

4.4.3 Proposal for axial stiffness ratio, κ

Based on Assumption (1), the axial stiffness of perforated GFRP tube is equal to the axial stiffness of intact vertical segment of perforated GFRP tube without holes. Therefore, the axial stiffness ratio κ between perforated GFRP tube and intact GFRP tube can be estimated according to Equation 4.3:

$$\kappa = 1 - \nu = \frac{\pi(D_i + t_f) - nd}{\pi(D_i + t_f)} \tag{4.3}$$

Figure 4.15 shows the axial stiffness ratio versus the perforation ratio from this study and Taheri-Behrooz et al. (2012). A linear relationship exists between the axial stiffness ratio and perforation ratio. Close agreements between the test data and prediction results can be observed in Figure 4.15. In addition, by using the proposed equation, a conservative prediction of axial stiffness ratio can be obtained. This may be due to the assumption that only the vertical intact part of the perforated GFRP tube carries the load. Therefore, the contribution from the vertical perforated part of GFRP tube is neglected.

Table 4.4 Summary of test results in Taheri-Behrooz et al. (2012)

No.	Radius of tubes R_o (mm)	Thickness t_f (mm)	Perforation ratio ν	ξ	Axial stiffness ratio κ	Axial deformation ratio λ	Axial critical load ratio η
1	53.15	2.2	0	0	1	1	1
2	53.15	2.2	0.174	0.462	0.874	0.742	0.650
3	53.15	1.5	0	0	1	1	1
4	53.15	1.5	0.175	0.560	0.816	0.741	0.642
5	30.2	2.2	0	0	1	1	1
6	30.2	2.2	0.316	0.613	0.919	0.825	0.760

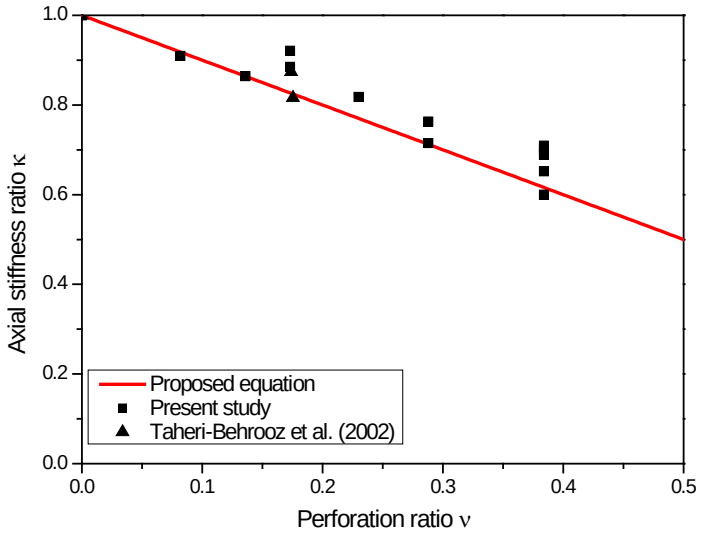

Figure 4.15 Prediction of axial stiffness ratio from perforation ratio (Wang et al. 2015b)

The accuracy of the prediction is quantified using two statistical indicators: mean square error (MSE) and average absolute error (AAE). These two indicators are determined by Equation 4.4 and Equation 4.5, respectively:

$$MSE = \frac{\sum_{i=1}^{N} \left(\frac{pre_i - exp_i}{exp_i} \right)^2}{N} \quad 4.4$$

$$AAE = \frac{\sum_{i=1}^{N} \left| \frac{pre_i - exp_i}{exp_i} \right|}{N} \quad 4.5$$

where *pre* is the prediction result, *exp* is the experimental result, and N is the total number of dataset.

The values of mean square error (MSE) and average absolute error (AAE) are only 0.4% and 4.7%, respectively. Hence, the proposed equation can predict the experimental behaviour with very good accuracy.

Axially perforated GFRP tubes and diagonally perforated GFRP tubes performed differently under axial compression. Therefore, it is not appropriate to adopt the same equations to predict the axial critical load as well as axial deformation capacity of perforated GFRP tubes with different perforation patterns. It has been proved in

this study that axially perforated GFRP tubes performed better than diagonally perforated GFRP tubes under axial compression. Therefore, experimental results on axially perforated GFRP tubes are used for the prediction of axial critical load as well as axial deformation capacity of the perforated GFRP tubes. Experimental results on diagonally perforated GFRP tubes (DPT) are excluded in the following section.

4.4.4 Proposal for axial critical load ratio, η

Due to the complex mechanism caused by perforation, few theoretical analyses have been conducted to predict the axial critical load of perforated cylindrical shells under axial compression (Almroth and Holmes 1972; Starnes 1972; Jullien and Limam 1998). Based on the analysis of available experimental results, it can be found that both the perforation ratio and parameter ξ will significantly affect the axial critical load of perforated GFRP tubes. The following equations are proposed based on the regression of existing experimental data to predict the axial critical load ratio of axially perforated GFRP tubes (APT) using perforation ratio and parameter ξ:

$$\eta = 0.953 - 1.226\nu \tag{4.6}$$

$$\eta = 0.967 - 0.158\xi \tag{4.7}$$

Figure 4.16 shows the axial critical load ratio versus the perforation ratio ν and Figure 4.17 shows the axial critical load ratio versus the parameter ξ. It can be seen that the axial critical load decreases with the increase of perforation ratio ν (parameter ξ). Hence, a linear relationship can be established. The comparison of mean square error (MSE) and average absolute error (AAE) for Equations 4.6 and 4.7 has been shown in Figure 4.18. It can be seen that the equations show good agreement with experimental results. Both the mean square error (MSE) and average absolute error (AAE) of Equation 4.6 were higher than those of Equation 4.7, which indicates that it is necessary to take the tube thickness into consideration for more accurate prediction of the axial critical load of perforated GFRP tubes. Nevertheless, for simplicity, Equation 4.6 can also be used with a satisfactory accuracy.

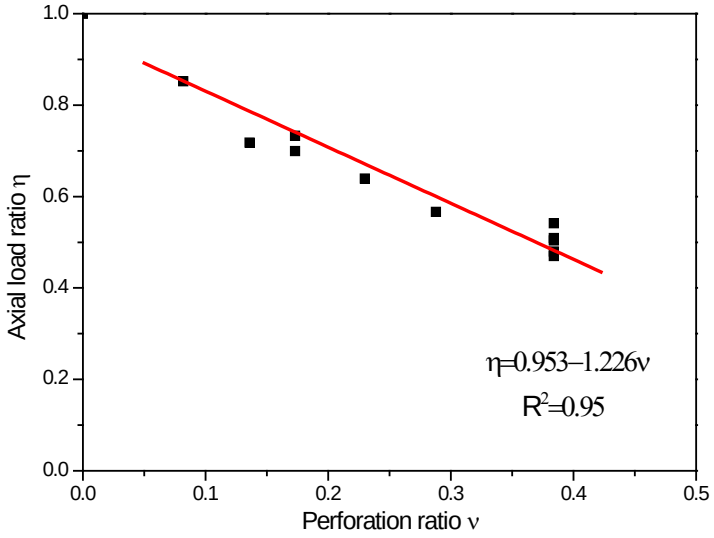

Figure 4.16 Prediction of axial critical load ratio from perforation ratio (axially perforated GFRP tubes) (Wang et al. 2015b)

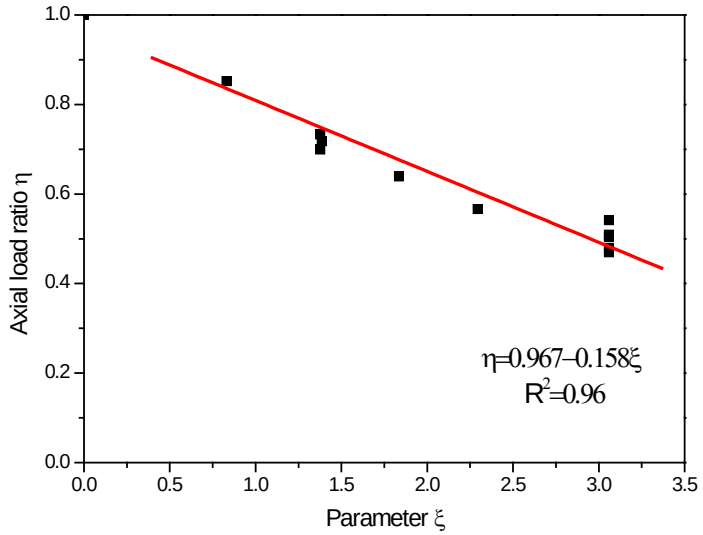

Figure 4.17 Prediction of axial critical load ratio from parameter ξ (axially perforated GFRP tubes) (Wang et al. 2015b)

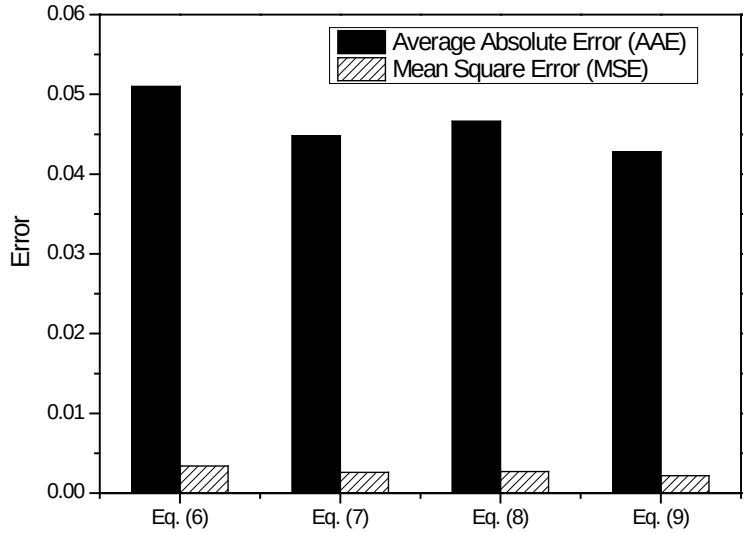

Figure 4.18 Error estimates of the proposed design-oriented equations (Wang et al. 2015b)

4.4.5 Proposal for axial deformation ratio, λ

Previously, attention was focused on the prediction of axial critical load of perforated cylindrical shells under axial compression, and none of the previous studies provided information for the prediction of axial deformation capacity of perforated cylindrical shells. Equations 4.8 and 4.9 are proposed to predict the axial deformation capacity for the axially perforated GFRP tubes (APT) based on a regression analysis of experimental results using perforation ratio ν and parameter ξ:

$$\lambda = 0.954 - 0.590\nu \quad 4.8$$

$$\lambda = 0.961 - 0.076\xi \quad 4.9$$

Figure 4.19 shows the axial deformation ratio versus perforation ratio ν, and Figure 4.20 shows the axial deformation ratio versus parameter ξ. A good correlation has been obtained between the predictions and experimental results. The comparison of mean square error (MSE) and average absolute error (AAE) for Equations 4.8 and 4.9 can be seen in Figure 4.18. Similar to the prediction of axial critical load, the prediction accuracy of axial deformation ratio is higher for equation developed based on parameter ξ (Equation 4.9). As a result, in order to get more accurate prediction, the influence of tube thickness should be taken into consideration.

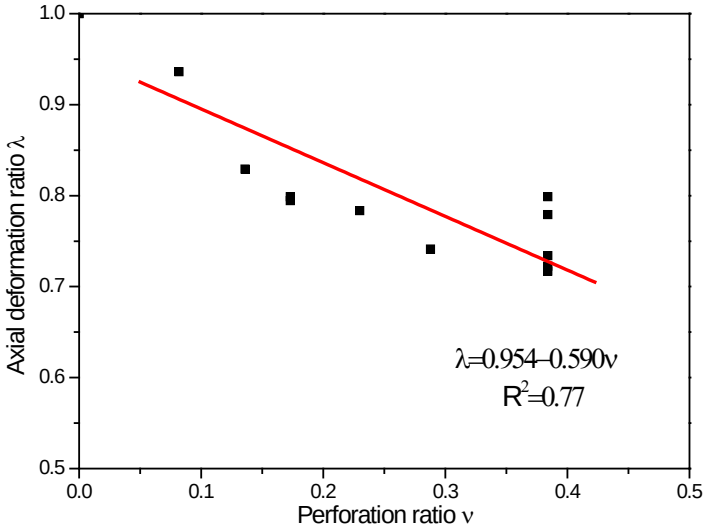

Figure 4.19 Prediction of axial deformation ratio from perforation ratio (axially perforated GFRP tubes) (Wang et al. 2015b)

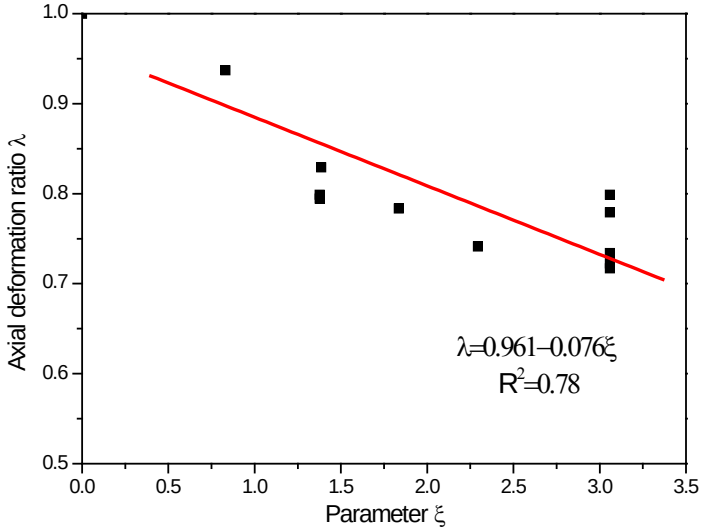

Figure 4.20 Prediction of axial deformation ratio from parameter ξ (axially perforated GFRP tubes) (Wang et al. 2015b)

In general, even though satisfactory prediction can be obtained by these equations, more test data is needed for perforated GFRP tubes with larger perforation ratio as well as with different tube thicknesses before proposing more general equations to predict the axial compressive behaviour of perforated GFRP tubes.

4.5 Conclusions

This chapter presents a comprehensive assessment of the parameters that may influence the axial compressive behaviour of perforated Glass Fibre Reinforced Polymer (GFRP) tubes. Design-oriented equations are developed to predict the axial compressive behaviour of perforated GFRP tubes. Based on the experimental and analytical studies, the following conclusions can be drawn:

(1) The key parameters controlling the axial compressive behaviour of perforated GFRP tubes are the hole diameter, tube diameter, perforation pattern, transverse hole spacing. Reducing the hole diameter or increasing the tube diameter as well as transverse hole spacing, the axial compressive behaviour of perforated GFRP tubes can be significantly improved. Axially perforated tubes (APT) perform better than diagonally perforated tubes (DPT) under axial compression;
(2) The influences of vertical hole spacing and hole reinforcement on the performance of perforated GFRP tubes under axial compression have been found not significant; and
(3) Design-oriented equations are developed for the prediction of axial stiffness, axial critical load and axial deformation capacity of perforated GFRP tubes under axial compression. The accuracies of the equations are verified by two statistical methods: average absolute error (AAE) and mean square error (MSE). The developed design-oriented equations can predict the axial compressive behaviour of perforated GFRP tubes with satisfactory accuracies.

In the following chapter, Type II FTRC column which consists of an inner concrete-filled FRP tube and an outer concrete component is investigated. Details of the experimental and analytical investigations are presented in Chapter 5.

5 BEHAVIOUR OF TYPE II FTRC COLUMNS UNDER AXIAL COMPRESSION

5.1 Introduction

In order to have an in-depth understanding of the axial compressive behaviour of the proposed Type II FTRC columns, an experimental program was carried out at the High Bay Civil Engineering Laboratory of the University of Wollongong, Australia. The experimental results have been presented and discussed. Afterwards, an analytical model has been developed to predict the performance of Type II FTRC columns under axial compression. The analytical model has been fully validated with experimental results. Finally, parametric analyses have been carried out to investigate the influences of different parameters on the axial compressive behaviour of Type II FTRC columns. The details of this study are presented in the following sections. For simplicity, the term “Type II FTRC column” is referred to as “FTRC column” in this chapter.

5.2 Experimental program

5.2.1 Design of experiment

A total of 16 concrete specimens with 150 mm in diameter and 300 mm in height were cast and tested under axial compression. The concrete specimens were divided into eight groups with two identical specimens in each group. One group of plain concrete specimens, two groups of FRP confined concrete specimens, and five groups of FTRC specimens were tested in this study. Plain concrete specimens and FRP confined concrete specimens were used mainly for comparison purpose to understand the behaviour of FTRC specimens. One layer and two layers of carbon FRP (CFRP) sheet were wrapped for FRP confined concrete specimens. For FTRC specimens, Glass FRP (GFRP) tubes with 6 mm thick and 77 mm inner diameter were used in this study. Polymer grid was chosen as the confinement of the outer concrete. Two types of polymer grid were used (Type A and Type B). The polymer grid was formed into tubular shape (e.g., tubular polymer grid) to provide confinement to the outer concrete. The diameter of the tubular grid was 133 mm. The clear concrete cover was 20 mm at the top and bottom of the specimen. The cross-

section view of FTRC specimen is shown in Figure 5.1. Details of the test matrix are presented in Table 5.1.

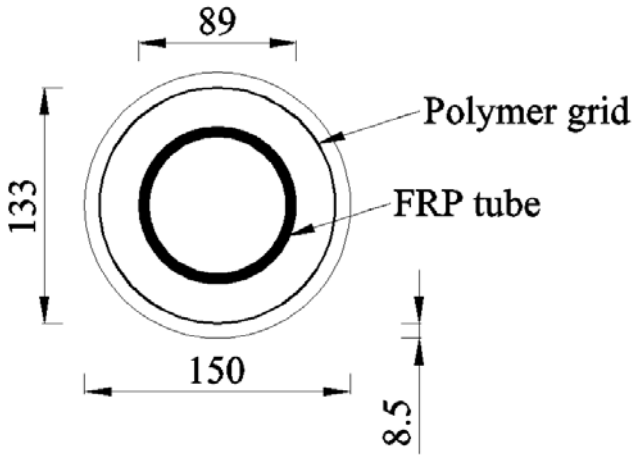

Figure 5.1 Cross-section view of Type II FTRC specimen (All units in mm)

Table 5.1 Test matrix in Chapter 5

Specimen	Inner confinement	Outer confinement	External confinement
P-(1, 2)	--	--	--
FC-1(1, 2)	--	--	1 layer CFRP
FC-2(1, 2)	--	--	2 layers CFRP
FTRC-0(1, 2)	GFRP tube	--	--
FTRC-1A(1, 2)	GFRP tube	1 layer Type A polymer grid	--
FTRC-2A(1, 2)	GFRP tube	2 layers Type A polymer grid	--
FTRC-1B(1, 2)	GFRP tube	1 layer Type B polymer grid	--
FTRC-2B(1, 2)	GFRP tube	2 layers Type B polymer grid	--

The labelling of concrete specimens has been carried out as: (a) “P” is used to identify plain concrete specimens; (b) “FC” represents FRP confined concrete specimens, and the number afterwards indicates number of CFRP layers; (c) “FTRC” indicates FTRC specimens; (d) “0” indicates no confinement was provided to the outer concrete of FTRC specimens; (e) “A” and “B” indicate types of polymer grid used for the confinement of the outer concrete of FTRC specimens, and the number before indicates the number of polymer grid layers. For instance, Specimen FC-1 indicates FRP confined concrete specimens wrapped with one layer of CFRP sheet. Specimen FTRC-1A indicates FTRC specimens for which the outer concrete was confined with one layer of Type A polymer grid.

5.2.2 Materials

The GFRP tubes used in this study were manufactured by Wagners CFT (2015). The mechanical properties of GFRP tubes provided by the manufacturers are listed in Table 3.5 in Chapter 3.

Two types of polymer grid were chosen as the confinement materials in this study (Figure 5.2). Type A polymer grid was square in shape (36 × 36 mm) and was manufactured from polypropylene (PP) fibres by Polyfabric Australia Pty Ltd (2015). Type B polymer grid was rectangular in shape (36 × 24 mm) and was manufactured from high modulus polyester fibres by Maccaferri Australia Pty Ltd (2015). These polymer grids have large tensile rupture strain together with excellent durability. In order to provide transverse confinement to the concrete, the polymer grid was formed into tubular shapes (e.g. tubular polymer grid) and held with plastic ties. Both Type A and Type B tubular grid had a diameter of 133 mm. The polymer grid was overlapped at an approximate length of 70 mm to ensure that the polymer grid would not be loosened or slid under axial load and to provide uniform confinement to the concrete core.

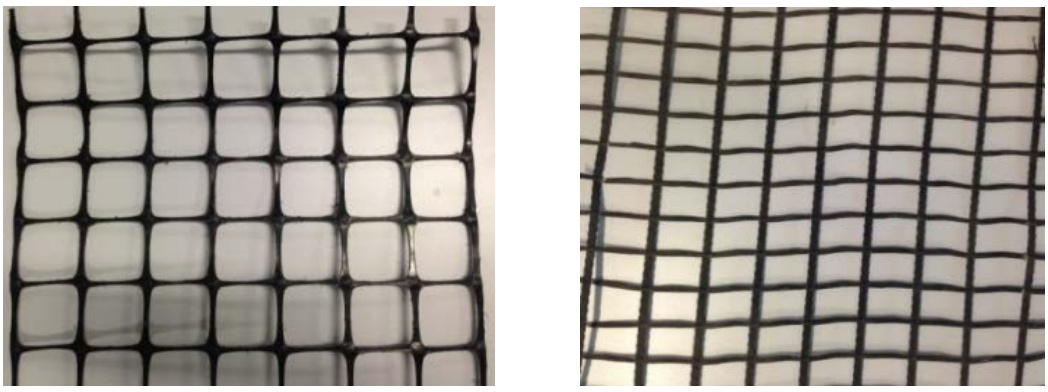

(a) Type A (b) Type B

Figure 5.2 Polymer grid (Wang et al. 2015a)

The carbon FRP (CFRP) sheet was manufactured by Nanjing Hitech Composites Co. (2015). The nominal thickness and width of each layer of CFRP sheet were 0.167 mm and 100 mm, respectively. According to the properties provided by the manufacturers, the ultimate tensile strength of CFRP sheet was 3400 MPa with a

tensile rupture strain of 0.017 mm/mm. Normal strength concrete with a design compressive strength of 32 MPa was used for casting the concrete specimens.

5.2.3 Preparation of concrete specimens

For FRP confined concrete specimens, the CFRP sheet was wrapped onto the specimens manually using a wet lay-up method. A mixture of epoxy resin and hardener at a ratio of 5:1 was used as the adhesive. Before wrapping of the first layer of CFRP, the adhesive was spread onto the surface of the specimen. After the first layer of CFRP was wrapped, the adhesive was spread onto the first layer of CFRP and the second layer was continuously wrapped. An overlap of 100 mm was maintained to prevent the premature debonding of CFRP. The epoxy resin was then left to cure for two weeks.

For FTRC specimens, GFRP tube and tubular polymer grid were placed into the mould before casting the concrete, as show in Figure 5.3. Strain gauges were longitudinally and transversely attached onto the mid-height of GFRP tubes to investigate the actual strain distributions. In order to ensure a 20 mm concrete cover at the top and bottom of the specimens, three tiny holes were drilled into the timber base as well as at the bottom of GFRP tubes. The holes were 10 mm in depth. Afterwards, three 40 mm long thin steel wires were inserted into the holes to support the GFRP tubes and to maintain 20 mm concrete cover. The steel wires were removed from the concrete specimens after curing of concrete. To ensure that the GFRP tube was in the middle of the mould, four thin steel wires were aligned symmetrically around the top end of GFRP tube. The steel wires were removed after casting of two thirds of the concrete. After casting of concrete, all the concrete specimens were kept wet during weekdays until the test date.

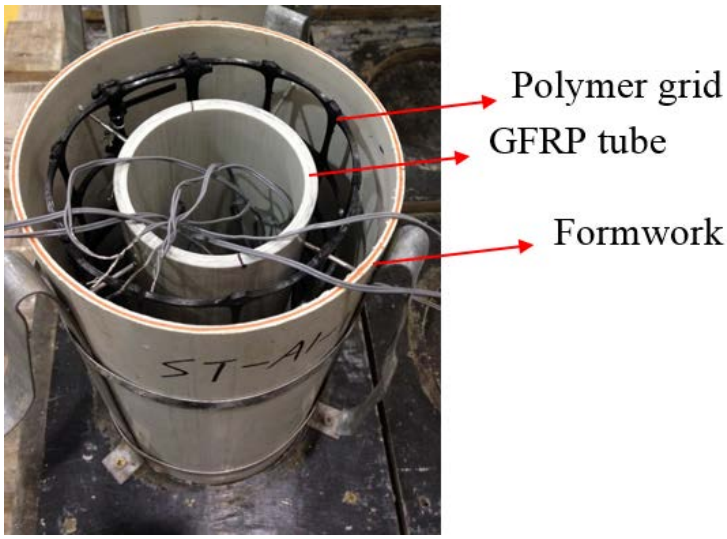

Figure 5.3 Formwork before casting

5.2.4 Preliminary tests

Concrete cylinders with 100 mm diameter and 200 mm height were tested for compressive strength at 28 days. The average compressive strength at 28 days was 35 MPa. The properties of CFRP sheet were determined by FRP coupon tests according to ASTM D7565/D7565M (2010). The average width of the coupons was 28.50 mm and the average maximum tensile force was 1200 N/mm. The recorded average ultimate tensile strain was 0.0172 mm/mm.

The GFRP tubes were tested under compression in accordance with GB/T 5350 (2005). Before testing, the tube was placed onto the loading plate to check whether there was any misalignment between the tube end and the bottom loading plate. If a slight misalignment was observed, the tube end was slightly smoothed using a belt sander until the misalignment was removed. The test was conducted at a rate of 0.3 mm/min. The average axial compressive strength of GFRP tube was 416 MPa with a corresponding axial strain of 0.0145. Due to the limitations of the experimental setup, the hoop tensile properties of the GFRP tubes could not be experimentally obtained. Therefore, the hoop tensile properties of the GFRP tubes provided by the manufacturers were used for subsequent analysis.

Tensile properties of the polymer grid were determined by testing one polymer grid strand using the Instron 8033 machine, as shown in Figure 5.4. Each end of the

polymer grid strand was embedded in steel clamps. The two steel plates were then tightened towards each other in order to fix the polymer grid. The total length of Type A polymer grid strand was 230 mm with a free length of 150 mm. The total length of Type B polymer grid strand was 158 mm with a free length of 102 mm. The displacement controlled test was carried out at a rate of 3 mm/min. The load and deformation data were recorded using an electronic data-logger connected to a computer for every two seconds. The recorded deformation was used to calculate the average tensile strain of the polymer grid. Three coupons were tested for each type of polymer grid. The axial tensile load-axial tensile strain curves of polymer grid have been shown in Figure 5.5. For Type A polymer grid, a nonlinear behaviour was observed, while for Type B polymer grid, a linear elastic behaviour was observed. The average ultimate tensile load per strand was approximately 1.43 kN for Type A polymer grid and 1.21 kN for Type B polymer grid. The average tensile strength was approximately 473 MPa with an elastic modulus of 6.5 GPa for Type A polymer grid, while the average tensile strength was 484 MPa with an elastic modulus of 5 GPa for Type B polymer grid.

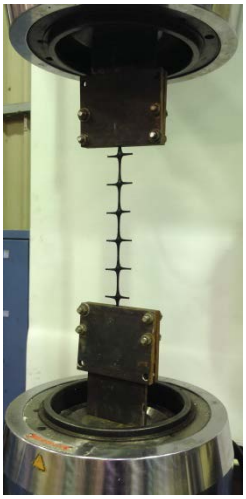

(a) Tensile test set up

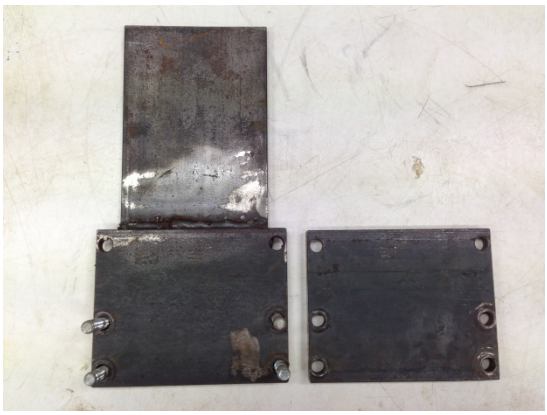

(b) Testing clamps

Figure 5.4 Polymer grid tensile test (Wang et al. 2015a)

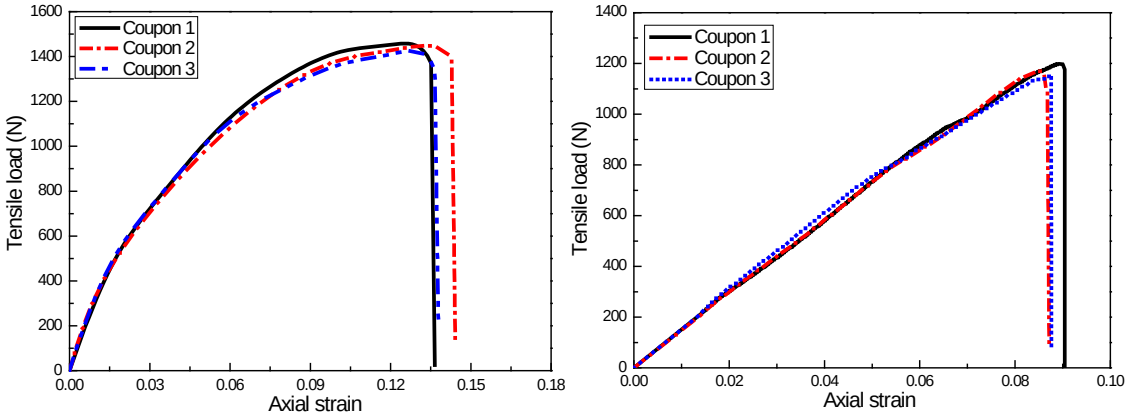

(a) Type A polymer grid (b) Type B polymer grid

Figure 5.5 Tensile load-axial strain curves of polymer grid (Wang et al. 2015a)

5.2.5 Instrumentation and test procedure

The Denison 5000 kN testing machine in the High Bay laboratory at University of Wollongong, Australia, was used for testing all the specimens. Before testing, all the specimens were capped at the top end with high strength plaster to ensure uniform load application. An additional layer of CFRP was wrapped at both ends of the specimens to prevent premature damage at the ends. Adequate care was taken to ensure that the specimens were placed at the centre of the testing machine. Axial deformations were measured using two Linear Variable Differential Transducers (LVDTs), which were mounted at the corners between the loading plate and supporting steel plate. The deformation readings from the two LVDTs were averaged to obtain representative results. The load and deformation data were recorded using an electronic data-logger connected to a computer for every two seconds. The displacement controlled tests were carried out at a rate of 0.5 mm/min.

5.3 Experimental results and analysis

5.3.1 Failure modes

Figure 5.6 shows the representative failure modes of tested specimens. FRP confined concrete specimens (FC-1, FC-2) failed in a brittle manner with rupture of CFRP sheet at the mid-height of specimens, which was followed by crushing and spalling of the concrete (Figure 5.6 (a)). For FTRC specimens, the concrete cover began to spall off when the unconfined concrete compressive strength was approached. Nevertheless, the specimens could still experience higher axial deformation after the

spalling of concrete cover. All the FTRC specimens finally failed due to the longitudinal rupture of GFRP tubes, which was accompanied by a loud noise. For Group FTRC-0 specimens, most of the outer concrete spalled off (Figure 5.6 (b)) since no confinement was provided to the outer concrete. For Groups FTRC-A and FTRC-B specimens, the spalling of outer concrete was effectively controlled because of the confinement provided by the polymer grid (Figure 5.6 (c)-(f)). The rupture of GFRP tubes resulted in a significant outward expansion of the FTRC specimens. For Groups FTRC-1B and FTRC-2B specimens, Type B polymer grid ruptured at the end of the test since the outward expansion of specimens was severe. However, for specimens of Groups FTRC-1A and FTRC-2A, Type A polymer grid did not rupture at the end of the test, which was because the tensile rupture strain of Type A polymer grid was considerably higher than that of Type B polymer grid.

(a) FC-1(1)

(b) FTRC-0(1)

(c) FTRC-1A(1)

(d) FTRC-2A(2)

(e) FTRC-1B(1)

(f) FTRC-2B (1)

Figure 5.6 Failure modes

5.3.2 Axial load-axial deformation behaviour

Figure 5.7 shows the axial load-axial deformation behaviour of Groups P(1), FC-1(1), FC-2(1), FTRC-0(1), FTRC-1A(1), and FTRC-2A(1) specimens. It is noted that the test results of two identical specimens in each group were quite similar to each other; therefore, only the test result from one specimen in each group was displayed. The test results of all FTRC specimens can be found in Section 5.4, in which all the test results were used to calibrate the accuracy of the proposed analytical model. It can be seen from Figure 5.7 that, up to yield load, all specimens showed similar behaviour (i.e., axial load increased with the increase in axial deformation). Afterwards, the axial load of Group P specimens decreased significantly and finally the specimen lost all the strength with a small deformation. Groups FC-1 and FC-2 specimens experienced a typical linear increase in axial load with increase in the axial deformation and finally failed in a brittle manner with the rupture of CFRP sheet. The ultimate load and the corresponding axial deformations were highly dependent on the number of layers of CFRP sheet. For Group FTRC-0 specimens, a considerable decrease in the axial load was observed after the yield load, which is attributed to the spalling of outer concrete. For Groups FTRC-1A and FTRC-2A specimens, the yield loads were less than those of Group FTRC-0 specimens, and no significant decrease in axial load was observed after the yield load. It can be explained that the existence of polymer grid interrupted the consistency of the outer concrete, which may have adversely influenced the casting quality of the outer concrete and resulted in a reduced yield load. Afterwards, the axial loads of the FTRC specimens was increased again because of the activation of confinement effect provided by GFRP tubes as well as the axial load carried by the GFRP tubes. Eventually, all the FTRC specimens failed due to the rupture of the GFRP tubes. Figure 5.8 shows the axial load-axial deformation diagram of Groups P(1), FC-1(1), FC-2(1), FTRC-0(1), FTRC-1B(1), and FTRC-2B(1) specimens (all the test results of FTRC specimens can be found in Section 5.4). Similar behaviour can be observed.

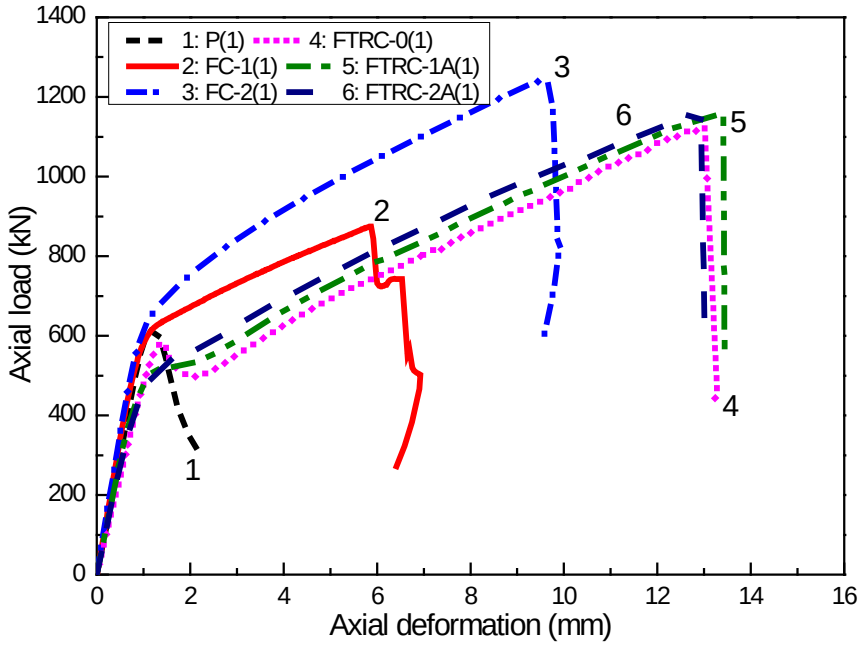

Figure 5.7 Axial load -axial deformation behaviour of Groups P(1), FC-1(1), FC-2(1), FTRC-0(1), FTRC-1A(1), and FTRC-2A(1) specimens

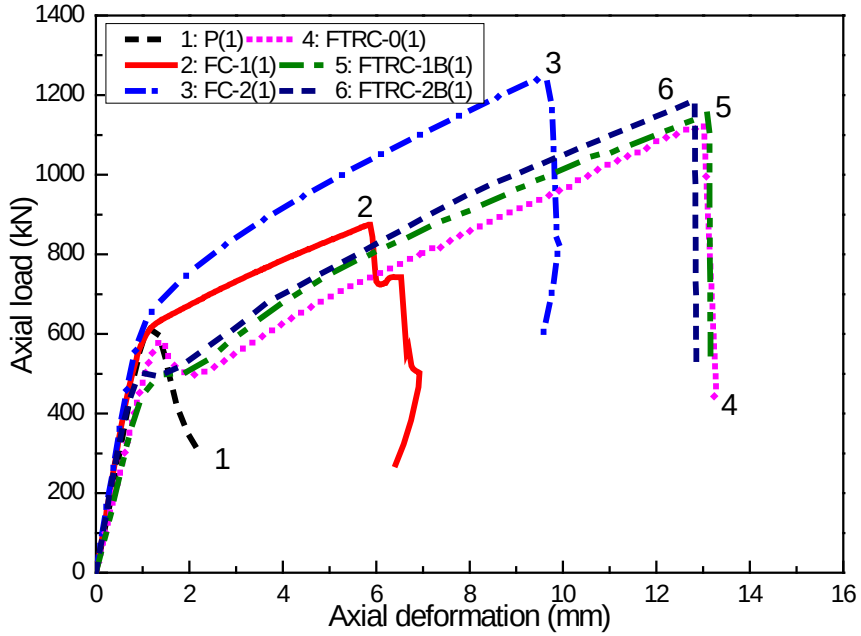

Figure 5.8 Axial load -axial deformation behaviour of Groups P(1), FC-1(1), FC-2(1), FTRC-0(1), FTRC-1B(1), and FTRC-2B(1) specimens

It can be seen from Figure 5.7 and Figure 5.8 that after the spalling of concrete cover, a much higher ultimate deformation can be achieved. This is beneficial for the safe design of concrete specimens: when the concrete cover began to spall off, more attention can be paid to evaluate the specimens to avoid catastrophic failure.

Moreover, by using polymer grid as confinement of outer concrete, the load carrying capacity of FTRC specimens was increased. The increase of axial load was higher if increased amount of polymer grid was applied. Nevertheless, the increase was not significant. This is attributed to the insufficient confinement provided by the polymer grid to the outer concrete due to its large openings as well as its lower tensile elastic modulus and lower tensile strength.

Table 5.2 summarizes the test results of all concrete specimens. The yield load, the ultimate load as well as the corresponding axial deformations have been presented. The ductility of the specimens (Cui and Sheikh 2010; Hadi et al. 2015) is calculated by Equation 3.1 in Chapter 3.

Table 5.2 Summary of test results

Specimen	Yield load (kN)	Corresponding axial deformation δ_y (mm)	Ultimate load (kN)	Corresponding axial deformation δ_u (mm)	Ductility μ
P(1)	613	1.180	613	1.180	1.000
P(2)	614	1.178	614	1.178	1.000
FC-1(1)	616	1.185	874	5.871	4.954
FC-1(2)	596	1.105	829	5.844	5.288
FC-2(1)	688	1.421	1240	9.431	6.637
FC-2(2)	652	1.451	1198	9.006	6.207
FTRC-0(1)	583	1.410	1124	13.011	9.228
FTRC-0(2)	590	1.170	1079	12.315	10.530
FTRC-1A(1)	521	1.473	1159	13.412	9.105
FTRC-1A(2)	515	1.299	1115	13.304	10.242
FTRC-2A(1)	535	1.527	1166	12.927	8.467
FTRC-2A(2)	478	1.544	1195	13.346	8.644
FTRC-1B(1)	492	1.381	1154	13.129	9.507
FTRC-1B(2)	528	1.444	1134	12.599	8.725
FTRC-2B(1)	555	1.400	1180	13.154	9.396
FTRC-2B(2)	502	1.128	1187	12.822	11.367

Note: The number within the bracket specifies the two identical specimens used in each group.

It can be seen from Table 5.2 that FTRC specimens show significant increase in both the ultimate load and the ductility compared to those of plain concrete specimens and FRP confined concrete specimens. All FTRC specimens possess much higher ultimate load and ductility than those of concrete specimens confined with 1 layer of CFRP sheet. The ultimate loads of FTRC specimens are slightly lower than those of specimens confined with two layers of CFRP sheet. However, the ductility is significantly higher. By applying polymer grid, the ultimate load has been increased slightly, while the ductility has not been increased since the failure of concrete specimens was dominated by the rupture of GFRP tubes.

5.3.3 Interaction between different constituent materials

In FTRC specimens, the interactions include the composite action between the FRP tube and inner concrete, the constraint to the FRP tube by outer concrete, and the confinement to the outer concrete by the polymer grid. The interaction may have few stages. At the first stage, the transverse expansion of FRP tube is larger than that of concrete due to the Poisson's ratio effect. According to the readings of strain gauges, the Poisson's ratio of FRP tube used in this study was 0.27. The Poisson's ratio was considered to be 0.20 for concrete. Therefore, the interaction between FRP tube and inner concrete does not exist, while the interaction between FRP tube and outer concrete exists. At this stage, the constraint to FRP tube by the outer concrete is not significant since all constituent materials are within the elastic state. At the second stage (especially after the unconfined concrete strength is reached), the transverse expansion of concrete becomes larger than that of FRP tube, and the confinement provided by the FRP tube to inner concrete is activated. Nevertheless, the interaction between FRP tube and outer concrete does not exist at this stage since the transverse expansion of outer concrete is more severe than that of FRP tube. The severe expansion of outer concrete is due to the insufficient confinement provided by the polymer grid. Therefore, the outer concrete cannot provide constraint to the FRP tube.

It has been reported that the transverse expansion of confined concrete depends significantly on the amount of confinement (Teng and Lam 2004). The concrete may

exhibit significant transverse expansion if less amount of confinement was provided. However, if the concrete was sufficiently confined, the transverse expansion can be significantly less. Therefore, if the inner concrete within the FRP tube is insufficiently confined (e.g., less amount of FRP) and the outer concrete is sufficiently confined, the transverse expansion of FRP tube may be larger than that of outer concrete component. Under such circumstances, the interaction between FRP tube and inner concrete as well as the interaction between FRP tube and outer concrete component may both exist. As a result, the outward expansion of FRP tube can be effectively constrained by the outer confined concrete, which may delay the rupture of the FRP tube.

5.4 Analytical model

In order to better understand the axial compressive behaviour of FTRC specimens, an analytical model has been developed in this section. Firstly, the stress-strain behaviours of different components (FRP tube, inner concrete, outer confined concrete, and cover concrete) of FTRC specimen have been described. Afterwards, an equation has been proposed to predict the load carrying capacity of FTRC specimens. Finally, the analytical results have been compared with experimental results to validate the accuracy of the analytical model.

5.4.1 Stress-strain behaviour of FRP tube

Due to the existence of axial stiffness, the mechanical behaviour of FRP tube is more complicated than that of FRP sheet for which the axial stiffness can be neglected (Chen et al. 2013). According to the mechanics of composite materials, the longitudinal compressive strength as well as transverse tensile strength of FRP tube can be determined as (Bank 2006):

$$\sigma_{f,l} = \frac{E_{f,l}}{1-\nu_1\nu_2}\varepsilon_{f,l} + \frac{\nu_1 E_{f,l}}{1-\nu_1\nu_2}\varepsilon_{f,t} \quad 5.1$$

$$\sigma_{f,t} = \frac{\nu_2 E_{f,t}}{1-\nu_1\nu_2}\varepsilon_{f,l} + \frac{E_{f,t}}{1-\nu_1\nu_2}\varepsilon_{f,t} \quad 5.2$$

where $\sigma_{f,l}$ and $\sigma_{f,t}$ are the longitudinal compressive stress and transverse tensile stress of the FRP tube, respectively; $\varepsilon_{f,l}$ and $\varepsilon_{f,t}$ are the corresponding strains; $E_{f,l}$

and $E_{f,t}$ are the longitudinal compressive and transverse tensile modulus of the FRP tubes; ν_1 and ν_2 are the longitudinal and transverse Poisson's ratios, respectively.

For FTRC specimens tested in this study, the GFRP tube is expected to fail if the longitudinal compressive strain of GFRP tube exceeded the longitudinal rupture strain $\varepsilon_{l,rup}$ which was recorded by the strain gauges during the test. In Section 5.5.4, parametric analyses have been conducted to investigate the influences of filament winding angles on the axial compressive behaviour of FTRC specimens. The failure modes of FRP tube can vary depending on the filament winding angles (Fam and Rizkalla 2001b). Therefore, it may be inappropriate to use the recorded longitudinal rupture strain $\varepsilon_{l,rup}$ to determine the failure of FRP tubes with different filament winding angles. Various failure criteria were proposed to predict the failure of FRP tube. Hinton et al. (2002) reported that the Tsai-Wu failure criterion performed better than other failure criteria. Therefore, the Tsai-Wu failure criterion has been used to predict the failure of FRP tube with different filament winding angles in Section 5.5.4 (Tsai and Wu 1971). The Tsai-Wu failure criterion can be expressed by Equation 5.3:

$$\left(\frac{1}{f_{t,t}}-\frac{1}{f_{t,c}}\right)\sigma_t+\left(\frac{1}{f_{l,t}}-\frac{1}{f_{l,c}}\right)\sigma_l+\frac{1}{f_{t,t}f_{t,c}}\sigma_t^2+\frac{1}{f_{l,t}f_{l,c}}\sigma_l^2+\frac{\tau_l^2}{\tau^2}-\frac{1}{\sqrt{f_{l,t}f_{l,c}f_{t,t}f_{t,c}}}\sigma_t\sigma_l=1 \quad (5.3)$$

where $f_{l,c}$ and $f_{t,c}$ are the longitudinal and transverse compressive strength of the FRP tube, respectively; $f_{l,t}$ and $f_{t,t}$ are the longitudinal and transverse tensile strength, respectively; and τ is the shear strength of the FRP tube.

5.4.2 Stress-strain behaviour of inner concrete

Many stress-strain models were proposed for FRP confined concrete (Ozbakkaloglu et al. 2013). During these models, the stress-strain model proposed by Lam and Teng (2003) is used to model the inner concrete since this model has been proved to be one of the most accurate stress-strain models (Ozbakkaloglu et al. 2013). Detailed expressions of Lam and Teng (2003) model can be found in Section 2.2.3 of Chapter 2.

5.4.3 Stress-strain behaviour of outer confined concrete and unconfined concrete

The strength of outer confined concrete is increased due to the confinement provided by the polymer grid. Currently, limited amount of research was carried out on the development of stress-strain models for the polymer grid confined concrete (Michael et al. 2005; Wang et al. 2015a). Wang et al. (2015a) proposed a stress-strain model to predict the peak strength and peak strain of polymer grid confined concrete specimens under axial compression. The model provides more accurate predictions of peak strength and peak strain than other available models (Wang et al. 2015a). However, the proposed stress-strain model cannot capture the full stress-strain behaviour of polymer grid confined concrete specimens under axial compression. According to Wang et al. (2015a), the stress-strain behaviour of polymer grid confined concrete is similar to that of steel reinforced concrete specimens. As a result, the stress-strain model proposed by Mander et al. (1988) is used to describe the full stress-strain relationship of polymer grid confined concrete. The stress-strain relationship for polymer grid confined concrete can be expressed by:

$$\sigma_c = \frac{xrf_{cc}^{'}}{r-1+x^r} \tag{5.4}$$

in which

$$x = \frac{\varepsilon_c}{\varepsilon_{cc}^{'}} \tag{5.5}$$

$$r = \frac{E_c}{E_c - \frac{f_{cc}^{'}}{\varepsilon_{cc}^{'}}} \tag{5.6}$$

where $f_{cc}^{'}$ is the peak compressive strength of polymer grid confined concrete; $\varepsilon_{cc}^{'}$ is the peak axial compressive strain at the peak compressive strength of confined concrete $f_{cc}^{'}$; E_c is the elastic modulus of the unconfined concrete, which can be calculated according to ACI 318 (2008):

$$E_c = 4730\sqrt{f_{cc}^{'}} \tag{5.7}$$

The peak strength and peak strain of polymer grid confined concrete can be calculated by Wang et al. (2015a):

$$\frac{f_{cc}^{'}}{f_{co}^{'}} = 1 + 0.0053\lambda_1 \tag{5.8}$$

$$\frac{\varepsilon_{cc}^{'}}{\varepsilon_{co}^{'}} = 1 + 0.0073\lambda_1 \tag{5.9}$$

in which

$$\lambda_1 = \frac{C_j}{\sqrt{f_{co}^{'}}} \tag{5.10}$$

The confinement modulus C_j can be defined as (Wang et al. 2015a):

$$C_j = -\frac{2k_e n A_g}{d_g(s_g + b_g)} E_g \tag{5.11}$$

where n, b_g, s_g, A_g and d_g are the number of polymer grid layers, width, spacing between transverse polymer grid, cross sectional area of the polymer grid, and the diameter of the polymer grid, respectively. k_e is the confinement effective coefficient which was firstly proposed by Sheikh and Uzumeri (1982), which can be expressed as:

$$k_e = \left(1 - \frac{s_g}{2d_g}\right)^2 \tag{5.12}$$

The stress-strain relationship of cover concrete is described using the model proposed by Mander et al. (1988) as well, which has been described above.

5.4.4 Load carrying capacity of FTRC specimens

The in-place concrete strength is generally lower than the compressive strength of concrete cylinders (ACI 318 2008; ACI 440.2R 2008). This difference is mainly attributed to the size effect, shape, and concrete casting quality. A reduction factor of 0.85 is suggested for steel RC columns by ACI 318 (2008). A similar reduction factor is suggested for FRP wrapped concrete columns by ACI 440.2R (2008) and for FRP bars reinforced concrete columns by Afifi et al. (2014). Therefore, a reduction factor of 0.85 is used to consider the strength reduction of in-place concrete in this study. The load carrying capacity of FTRC column can be calculated as the sum of axial loads carried by FRP tube, inner concrete, outer confined concrete, and concrete cover:

$$P = P_f + P_{ic} + P_{oc} + P_{cover} = \sigma_{f,l} A_f + 0.85\sigma_{ic} A_{ic} + 0.85\sigma_{oc} A_{oc} + 0.85\sigma_{cover} A_{cover} \quad 5.13$$

where P_f, P_{ic}, P_{oc} and P_{cover} are the axial loads carried by FRP tube, inner concrete, outer confined concrete, and concrete cover, respectively; $\sigma_{f,l}$, σ_{ic}, σ_{oc} and σ_{cover} are the axial compressive strengths of FRP tube, inner concrete, outer confined concrete, and outer unconfined concrete, respectively; and A_f, A_{ic}, A_{oc} and A_{cover} are their corresponding cross-section areas.

5.4.5 Comparisons between experimental and analytical results

The comparisons between experimental and analytical results are shown in Figure 5.9. It can be seen that the analytical results matched well with the experimental results. The analytical model overestimates the yield loads of FTRC specimens, which was mainly attributed to the premature spalling of concrete cover before the unconfined concrete strength was reached. In general, the analytical model predicts the axial load-axial strain behaviour of FTRC specimens with good accuracy due to the selection of appropriate stress-strain models for different components of FTRC specimens.

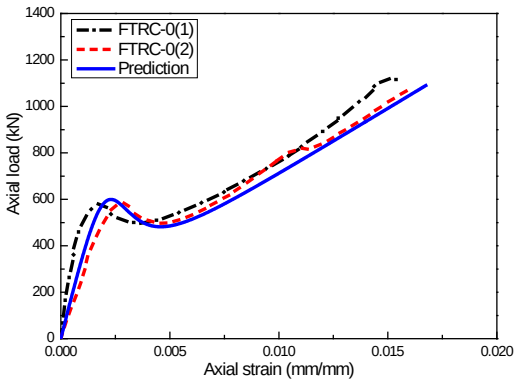

(a) Specimens FTRC-0

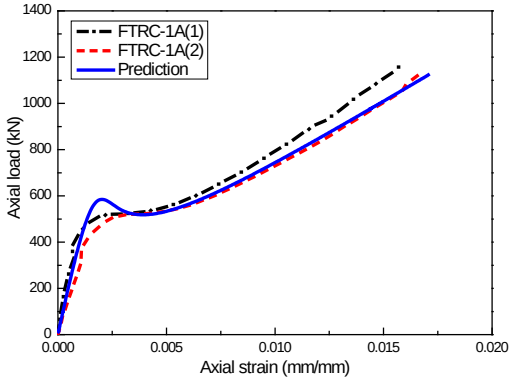

(b) Specimens FTRC-1A

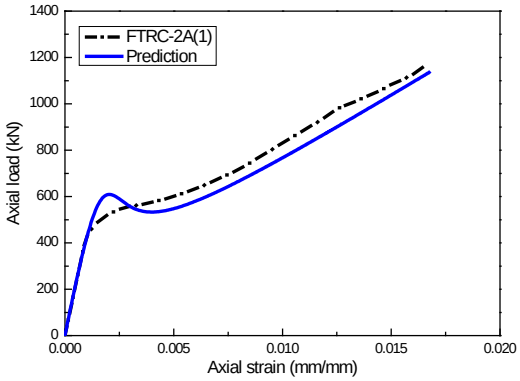

(c) Specimen FTRC-2A

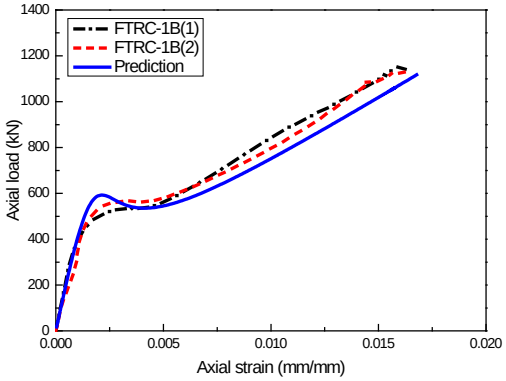

(d) Specimens FTRC-1B

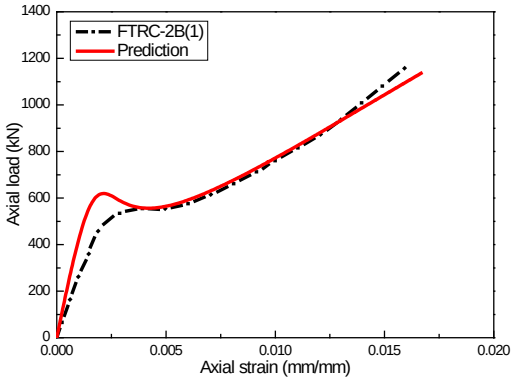

(e) Specimen FTRC-2B

Figure 5.9 Comparisons between experimental results and model predictions (Note: the strain gauges failed during the test for Specimens FTRC-2A(2) and FTRC-2B(2))

Figure 5.10 shows the analytical axial load-axial strain curves of Specimen FTRC-1A(2). The axial load carried by each component is shown as well. At the first stage (before Point A), nearly linear elastic behaviour can be observed for all components. At the second stage (Point A to Point B), the concrete cover began to spall off, which resulted in the loss of axial load. The strength of outer confined concrete was decreased with the increase of axial strain, although the decrease was much less than

that of concrete cover. In contrast, the strength of inner concrete was increased due to the confinement provided by the FRP tube, and the axial load carried by FRP tube also showed a linear increase with axial strain. The load reduction of outer concrete was higher than the load increase of inner concrete and FRP tube, which resulted in the overall decrease of axial load. At the third stage (Point B to Point C), with the increase of axial strain, the load increase of inner concrete and FRP tube became larger than the load reduction of outer concrete, which resulted in an overall increase of axial load until the rupture of GFRP tube (Point C). It is noted that the inner concrete-filled FRP tube carried a vast majority of the axial load of the specimen, and this proportion was even higher with the increase of axial strain. Considering a more ductile failure mode of FTRC specimens, it is important that the outer concrete carry a certain proportion of axial load before failure. Under this condition, even though the inner concrete-filled FRP tube lost all the strength after the sudden failure, the outer concrete component could still carry significant amount of axial load, which is essential to prevent the overall collapse of the specimens (Feng et al. 2015). To achieve this, the size of outer concrete can be increased and more confinement as well as additional longitudinal reinforcement can be applied for the outer concrete.

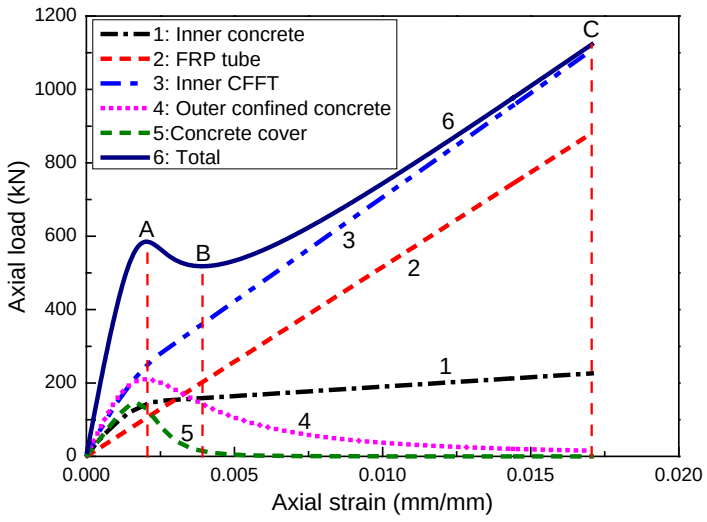

Figure 5.10 Load carried by each component of Specimen FTRC-1A

5.5 Parametric analyses

Parametric analyses have been carried out to investigate the influences of different parameters on the axial compressive behaviour of FTRC specimens. The influences of outer concrete strength, inner concrete strength, FRP tube thickness, filament winding angles of FRP tube, and amount of polymer grid have been analytically investigated. It is noted that Specimen FTRC-1A has been used as a reference specimen. All the parameters in the following analysis have been kept the same as the parameters in Specimen FTRC-1A, if not otherwise specified.

5.5.1 Influence of inner concrete strength

Four inner concrete strength grades have been considered (35 MPa, 45 MPa, 55 MPa, and 65 MPa). The outer concrete strength has been considered to be 35 MPa, and the FRP tube thickness is considered to be 4 mm. All other parameters have been kept constant. Figure 5.11 shows the axial load-axial strain behaviour of FTRC specimens with different inner concrete strengths. It is evident that the increase in the inner concrete strength can lead to significant increases in both yield load and ultimate load. The ultimate axial strain is not significantly affected by the inner concrete strength, as the failure of concrete specimens is dominated by the rupture of GFRP tube.

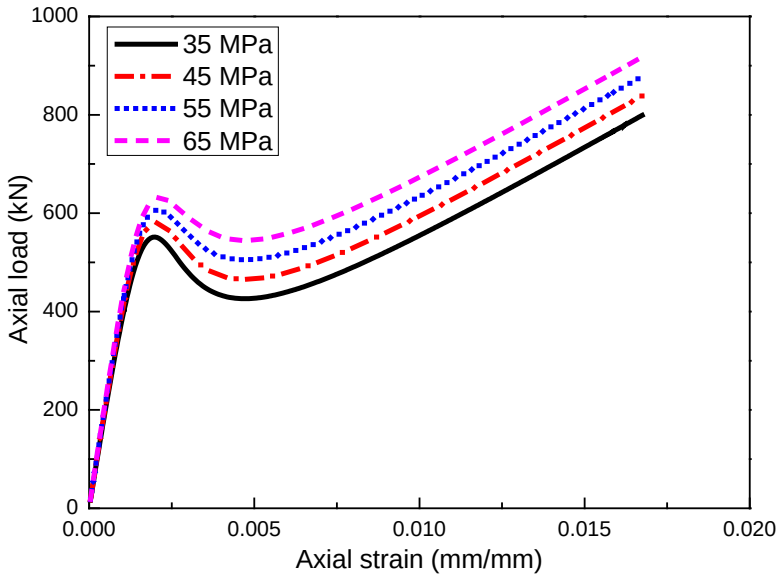

Figure 5.11 Axial load-axial strain behaviour of specimens for different inner concrete strength

5.5.2 Influence of outer concrete strength

The influence of outer concrete strength on the axial compressive behaviour of FTRC specimens has been investigated using four different concrete strength grades (35 MPa, 45 MPa, 55 MPa, and 65 MPa). The inner concrete strength has been considered to be 35 MPa. The FRP tube thickness is 4 mm. All other parameters have been kept constant. The axial load-axial strain behaviours of FTRC specimens with different outer concrete strength grades are shown in Figure 5.12. It is evident that by increasing the strength of outer concrete, the yield load can be significantly increased. However, the increase in the ultimate load and ultimate axial strain is insignificant. This insignificant effect is mainly due to that the outer concrete loses almost all the strength before the failure of concrete specimens since the confinement provided by the polymer grid is very low.

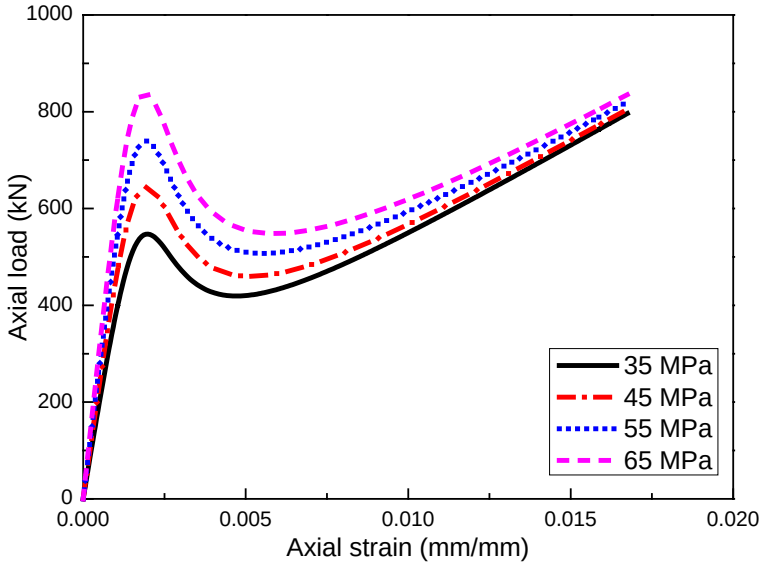

Figure 5.12 Axial load-axial strain behaviour of specimens for different outer concrete strength

5.5.3 Influence of FRP tube thickness

The influence of FRP tube thickness on the axial compressive behaviour of FTRC specimens has been investigated by changing the thickness of FRP tubes (3 mm, 4 mm, 5 mm, and 6 mm), while all other parameters have been kept constant. The axial load-axial strain behaviour of FTRC specimens with different FRP tube thickness is shown in Figure 5.13. It can be seen that by increasing the thickness of FRP tube, the

yield load is increased slightly. However, the ultimate load is increased significantly. The increase of axial load is higher with the increase of axial strain especially after the yield load. This can be explained that due to the linear properties of FRP tube, the axial load carried by the FRP tube increases linearly until failure. Therefore, the axial load difference for FRP tubes with different thicknesses becomes larger with the increase of axial strain.

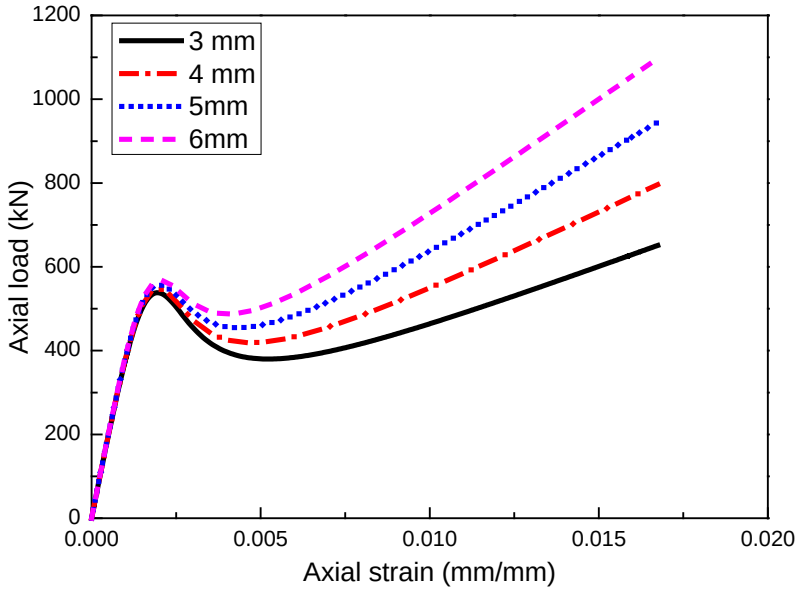

Figure 5.13 Axial load-axial strain behaviour of specimens for different FRP tube thicknesses

5.5.4 Influence of filament winding angle of FRP tube

The influence of filament winding angles on the axial compressive behaviour of FTRC specimens has been investigated by changing the filament winding angles of FRP tubes. Four different filament winding angles have been selected (±0°, ±30°, ±60°, and ±90°). It is noted that the angles are measured with respect to the longitudinal axial of the FRP tubes. The FRP tube thickness is considered 4 mm. All the other parameters have been kept constant. In order to determine the mechanical properties of FRP tube with different filament winding angles, the software "The laminator" has been used (The Laminator 2015). The Laminator was developed based on the classical laminate theory and provides a reasonable agreement with the test results (Mohamed and Masmoudi 2010a). The Tsai-Wu failure criterion has been used to predict the failure of FRP tube, as explained in Section 5.4.1.

The axial load-axial strain behaviour of FTRC specimens with FRP tubes having different filament winding angles is shown in Figure 5.14. It can be seen that FTRC specimen with FRP tube having all the fibres in the longitudinal direction (±0°) can achieve the highest yield load and ultimate load, although the ultimate axial strain is the lowest. With the increase of fibres in the transverse direction (±30°), the yield load is decreased, and the ultimate axial strain is increased. For FTRC specimens with FRP tubes having majority of fibres in the longitudinal direction (±0°, ±30°), the transverse tensile strength is relatively low and a transverse tensile rupture occurs. Therefore, the longitudinal compressive strength of FRP tube cannot be not fully utilized. However, for FRP tubes with majority of fibres along the transverse direction, longitudinal compressive rupture occurs before the transverse tensile strength of FRP tube can be fully utilized (±60°, ±90°) since the longitudinal compressive strength of the FRP tube is relatively low. Therefore, an optimum proportion of fibres in both longitudinal and transverse direction of FRP tube will significantly improve the performance of FTRC specimens under axial compression. It is also noted that the ultimate loads are higher for FTRC specimens having FRP tube with majority of fibres aligned in the longitudinal direction (±0°, ±30°). This can be explained that for concrete confined by very thick FRP tubes, the contribution of axial load by the FPR tube is more significant than the gain from the confinement of concrete. This observation can also be validated by Fam et al. (2003).

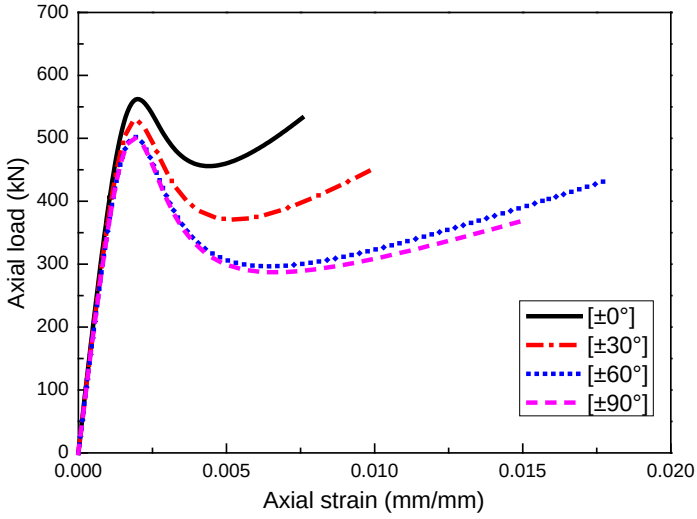

Figure 5.14 Axial load-axial strain behaviour of specimens for different filament winding angles of FRP tubes

5.5.5 Influence of amount of polymer grid

The influence of the amount of polymer grid has been investigated by changing the number of polymer grid layers (1 layer, 2 layers, 3 layers, and 4 layers). The strength of both inner and outer concrete is 35 MPa. The FRP tube thickness is 4 mm. All other parameters have been kept constant. It can be seen from Figure 5.15 that by increasing the amount of polymer grid, the yield load and ultimate load can be increased only slightly. This is due to the insufficient confinement provided by the polymer grid. Even though the yield load, ultimate axial load, and ultimate axial strain have not been increased, it is still necessary to apply more amount of polymer grid because the polymer grid can be effective in preventing the overall collapse of the concrete specimens when the tensile rupture strain of polymer grid is sufficiently high (e.g., Type A polymer grid) (Feng et al. 2015).

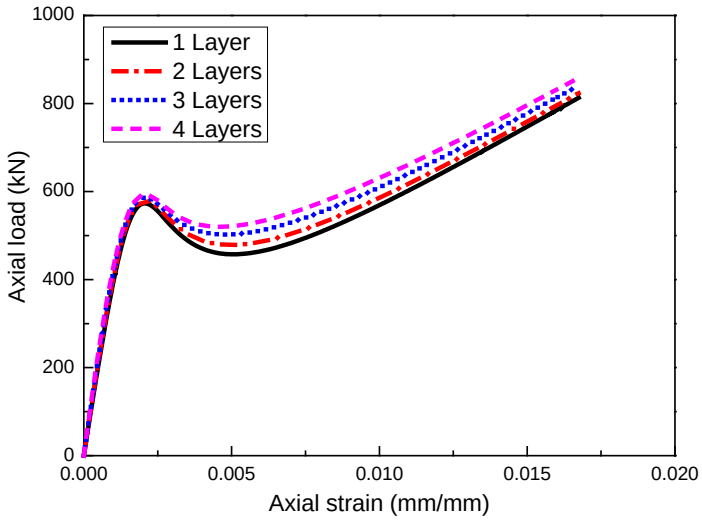

Figure 5.15 Axial load-axial strain behaviour of specimens for different amount (number of layers) of polymer grid

5.6 Conclusions

In this study, the axial compressive behaviour of FRP tube reinforced concrete (FTRC) columns has been experimentally investigated. An analytical model for the prediction of axial load-axial strain behaviour of FTRC columns has been developed and validated with experimental results. Moreover, parametric analyses have been

carried out to investigate the influences of different parameters on the axial compressive behaviour FTRC columns. The following conclusions can be drawn:

(1) FTRC columns can obtain considerable amount of strength and ductility under axial compression. The FRP tube not only provides confinement to the inner concrete but can also carry axial load. The polymer grid provides confinement to the outer confined concrete and prevents the overall collapse of FTRC columns. Moreover, after the spalling of the concrete cover, the FTRC columns can still carry substantial amount of axial load with a much higher axial deformation, which is beneficial for the safe design of concrete columns;
(2) The yield load of FTRC column can be increased by increasing the strength of inner concrete as well as the outer concrete. The ultimate axial load can be increased significantly by increasing the strength of inner concrete. However, the ultimate axial load cannot be significantly increased by increasing the strength of outer concrete;
(3) By increasing the FRP tube thickness, both the yield load and ultimate axial load can be increased. However, the increase is more significant for ultimate axial load. The filament winding angles of FRP tube can significantly influence the yield load, ultimate load, and ultimate axial strain of FTRC columns; and
(4) The polymer grid does not contribute significantly to the yield load, ultimate axial load, and ultimate axial strain of FTRC columns, since the confinement provided by the polymer grid is weak due to the large openings as well as its lower tensile properties. Nevertheless, the polymer grid is essential to prevent the overall collapse of FTRC columns.

Chapter 6 presented an extensive investigation on the axial compressive behaviour of concrete confined with polymer grid, which aims to better understand the behaviour of Type II FTRC columns under axial compression.

6 BEHAVIOUR OF CONCRETE CONFINED WITH POLYMER GRID UNDER AXIAL COMPRESSION

6.1 Introduction

In Type II FTRC column, polymer grid is chosen to provide confinement to the outer concrete. The polymer grid can be easily formed into a circular shape without sharp bends and hence the tensile capacity of the polymer grid can be used effectively (Hadi and Zhao 2011; Hadi et al. 2013). Moreover, the polymer grid can be easily embedded into the concrete prior to casting, and the thickness of concrete cover can be reduced due to the corrosion resistance property of polymer grid. For better understanding of the proposed Type II FTRC columns, the axial compressive behaviour of concrete confined with polymer grid needs to be extensively studied.

An experimental programme was conducted at the High Bay Civil Engineering Laboratory of the University of Wollongong, Australia. A total of 14 concrete specimens with 150 mm diameter and 300 mm height were prepared and tested under axial compression. Two types (Type A and Type B) of polymer grid with different mechanical properties were selected. Type A polymer grid (36 mm×36 mm) was manufactured from polypropylene fibres, while Type B polymer grid (36 mm×24 mm) was manufactured from high modulus polyester fibres. For each type of polymer grid, one layer, two layers, and three layers were used to investigate the influence of the amount of polymer grid confinement on the axial compressive behaviour of concrete specimens. The axial load-axial deformation behaviour of concrete specimens was investigated. The ductility, energy absorption capacity, and failure modes were critically studied as well. Finally, an analytical model was developed to predict the axial compressive behaviour of polymer grid confined concrete.

6.2 Experimental program

6.2.1 Materials

Type A polymer grid was square in shape (36 × 36 mm) and was manufactured from polypropylene by Polyfabric Australia Pty Ltd (2015). Type B polymer grid was rectangular in shape (36 × 24 mm) and was manufactured from high modulus polyester fibres by Maccaferri Australia Pty Ltd (2015). More details can be found in

Section 5.2.2 in Chapter 5. It was noted that the tubular polymer grid was overlapped at an approximate length of 70 mm to ensure that the polymer grid would not be loosened or slid and to provide uniform confinement to the outer concrete. The concrete specimens were made of normal strength concrete with a design compressive strength of 32 MPa.

6.2.2 Test Matrix

A total of 14 concrete specimens with 150 mm in diameter and 300 mm in height were cast and tested under axial compression. The concrete cover thickness was 8 mm, as shown in Figure 6.1. The specimens were divided into seven groups. Each group contained two identical specimens. The first group contained two plain concrete specimens without confinement. The specimens in the remaining six groups were confined with polymer grid. No longitudinal reinforcement was provided.

Table 6.1 lists the specimens tested in this study. The ratios of the thickness of tubular polymer grid (t) and the diameter of concrete core (d_g) are also presented in Table 6.1. The specimens have been named as: (a) "P" identifies plain concrete specimens used as reference specimens; (b) "G" represents concrete specimens confined with polymer grid; (c) "A" and "B" are used to indicate polymer grid types (Type A polymer grid and Type B polymer grid), and the number afterwards indicates the number of polymer grid layers (One, two, and three layers); (d) the last numbers "1" and "2" are used to distinguish between two nominally identical specimens in each group. For example, Specimen G-A1-1 indicates the first of the two identical concrete specimens that were confined with one layer of Type A polymer grid.

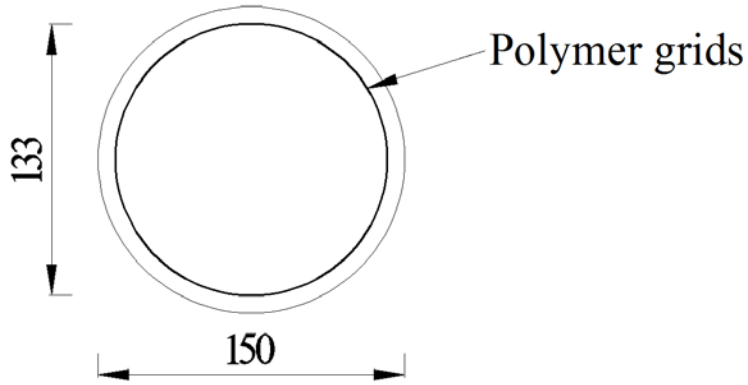

Figure 6.1 Cross-section view of concrete specimens (All units in mm)

Table 6.1 Test matrix in Chapter 6

Specimens	Types of polymer grid	Layers of polymer grid	t / d_g
P-(1,2)	-	-	-
G-A1-(1,2)	Type A	1 layer	0.015
G-A2--(1,2)	Type A	2 layers	0.030
G-A3-(1,2)	Type A	3 layers	0.045
G-B1-(1,2)	Type B	1 layer	0.005
G-B2-(1,2)	Type B	2 layers	0.009
G-B3-(1,2)	Type B	3 layers	0.014

Note: t indicates the thickness of tubular polymer grid and d_g indicates the diameter of the concrete core.

6.2.3 Casting of specimens

After the tubular grid was placed into the mould, concrete was mixed and cast. After casting, a wet hessian was placed over the specimens to prevent moisture loss. All the specimens were watered during weekdays until the test date. Before the axial compression test, both ends of the specimens were strengthened with 1 layer of CFRP sheet in order to prevent premature end failure during the test. The CFRP sheet was of 25 mm width with a nominal thickness of 0.167 mm as provided by the manufacturer. After the wrapping of CFRP sheet, all the specimens were capped at the top end with high strength plaster to ensure uniform load application during the test.

6.2.4 Preliminary tests

Three concrete cylinders with 100 mm in diameter and 200 mm in height were tested for concrete compressive strength on 28 days. The average compressive strength on 28 days was 35 MPa. The tensile properties of the polymer grid were determined by testing polymer grid strands using the Instron 8033 machine. The average tensile strength was approximately 430 MPa with an elastic modulus of 6.5 GPa for Type A polymer grid, while the average tensile strength was 464 MPa with an elastic modulus of 5 GPa for Type B polymer grid.

6.2.5 Instrumentation and test procedure

The Denison 5000 kN testing machine in the High Bay laboratory at University of Wollongong, Australia, was used for testing all the specimens. The concrete specimens were placed vertically on the bottom loading plate. Axial deformations were measured using two Linear Variable Differential Transducers (LVDTs), which were mounted at the opposite corners between the bottom loading plate and supporting steel plate. The deformation readings from the two LVDTs were then averaged to obtain representative results. The axial load and axial deformation data were recorded at every three seconds using an electronic data-logger connected to a computer. The displacement controlled tests were carried out at a rate of 0.5 mm/min.

6.3 Experimental results and discussion

6.3.1 Failure modes

The premature spalling of concrete cover for polymer grid confined concrete specimens was first observed during the test, which resulted in a lower axial peak load than that of plain concrete specimens. As the concrete cover thickness (8 mm) was less than the maximum aggregate size (10 mm) of the concrete, the integrity of the concrete cover was not satisfactory, which caused the premature spalling of concrete cover. Figure 6.2 shows the representative failure modes of polymer grid confined concrete specimens after tests. Progressive failure was observed for all polymer grid confined concrete specimens. As can be seen from Figure 6.2, the concrete core expanded outwards significantly. No polymer grid rupture was observed for Type A polymer grid confined concrete specimens. While for Type B

polymer grid confined concrete specimens, the rupture of polymer grid was significant, resulting in the failure of the specimens. Moreover, for concrete specimens confined with one layer of polymer grid, less amount of concrete core remained intact after failure. For concrete specimens confined with two and three layers of polymer grid, larger amount of concrete remained intact within the tubular grid after failure.

(a) G-A1-2 (b) G-B1-2 (c) G-A3-1 (d) G-B3-2

Figure 6.2 Representative failure modes of specimens (Wang et al. 2015a)

6.3.2 Axial load-axial deformation behaviour

Figure 6.3 (a) shows the axial load-axial deformation behaviour of Specimens P-1(2), G-A1-1(2), G-A2-1(2), and G-A3-1. The test data for Specimen G-A3-2 was lost during the test. It can be observed that all specimens showed similar behaviour before the peak load. After the peak load, all specimens showed significant decrease in load carrying capacity because of the strength reduction of concrete. Even though the lateral expansion of concrete is significant at this stage, the confinement effect provided by the polymer grid to the concrete core was marginal, as the amount of confinement provided by the polymer grid is low due to its large openings. For example, for Type A polymer grid, only 7.5% of the concrete core surface was covered by the transverse polymer grid. For Type B polymer grid, only 13% of the concrete core surface was covered by transverse polymer grid. In addition, the polymer grid used in this study had a lower tensile elastic modulus, which may further reduce the confinement effect of concrete specimens. After the drastic reduction in the axial load, the unconfined concrete specimens lost all the strength

and finally failed in a brittle manner with a small axial deformation. However, after the significant reduction in the axial load, the axial load-axial deformation behaviour of polymer grid confined concrete specimens became more and more gradual and finally became stable without any decrease in the load carrying capacity. This can be explained that after the drastic reduction of axial load, the lateral expansion of concrete core became more significant, and the confining pressure provided by the polymer grid became much higher. When the confining pressure reached a certain level, the axial load carried by the concrete core would not decrease and can be sustained up to a larger deformation. The axial load at the end of the test is highly dependent on the amount of polymer grid confinement. Specimen confined with three layers of Type A polymer grid reached an axial load of 230 kN at the end of the test, which is 40% of the peak load of unconfined concrete specimens. Axial loads of 180 kN and 130 kN were observed at the end of the test for concrete specimens confined with two layers and one layer of Type A polymer grid, respectively.

Notably, the deformation capacity of Type A polymer grid confined concrete specimens was much higher than that of unconfined concrete specimens, which is beneficial for the seismic design of concrete specimens where the deformation capacity is a very important issue (Sheikh et al. 2010; Sheikh and Légeron 2014). It should be noted that for all the concrete specimens confined with Type A polymer grid, the load carrying capacity was not fully exhausted at the end of the test (no occurrence of polymer grid rupture), which means that the confined concrete specimens might still carry some axial load with a larger axial deformation. In fact, the tests were stopped due to the deformation limit set in the computer programme for Type A polymer grid confined concrete specimens.

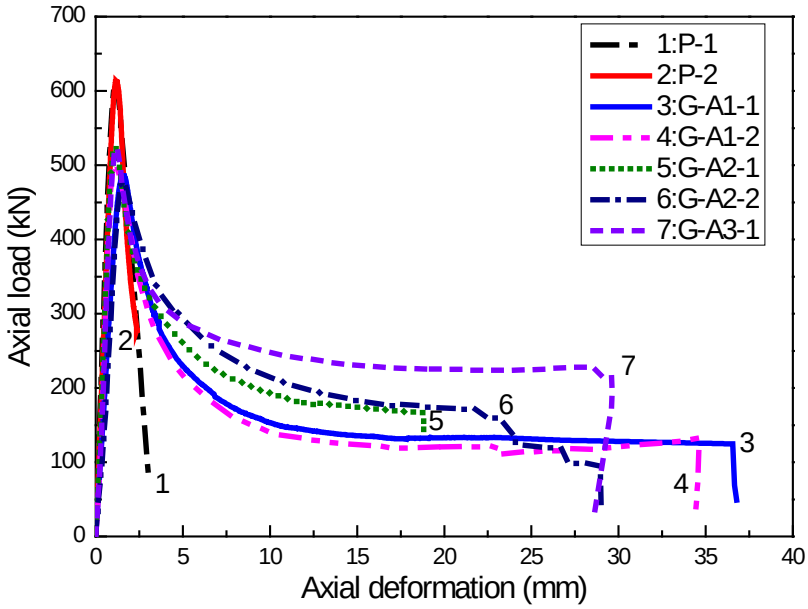

(a) Specimens confined with Type A polymer grid and unconfined concrete specimens

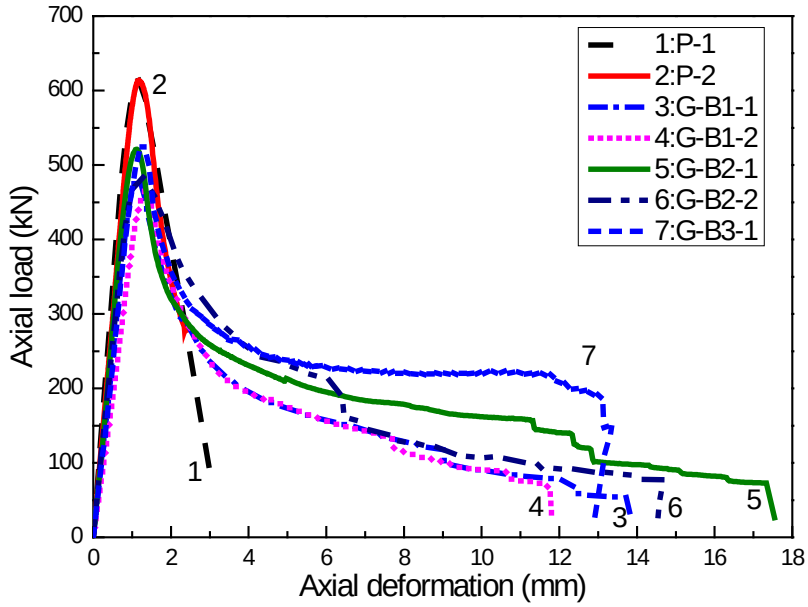

(b) Specimens confined with Type B polymer grid and unconfined concrete specimens

Figure 6.3 Axial load-axial deformation behaviour of concrete specimens (Wang et al. 2015a)

Figure 6.3 (b) shows the axial load-axial deformation behaviour of Specimens P-1(2), G-B1-1(2), G-B2-1(2), and G-B3-1. The test data for Specimen G-B3-2 was lost during the test. Similar axial compressive behaviour can be observed for all

polymer grid confined concrete specimens. Type B polymer grid confined concrete specimens possessed higher strength and deformation capacity than unconfined concrete specimens. Specimens confined with one layer and two layers of Type B polymer grid experienced a continuous decrease of axial load with the increase of axial deformation. Only specimen confined with three layers of Type B polymer grid experienced a constant axial load before the rupture of polymer grid. It is noted that the specimen confined with three layers of Type B polymer grid showed a smaller axial deformation at the end of the test, which may be due to the premature rupture of polymer grid caused by stress concentration. Moreover, it can be observed from Figure 6.3 that the peak loads of polymer grid confined concrete specimens were less than those of unconfined concrete specimens. This unexpected phenomenon can be attributed to the following reasons: (1) the consistency of concrete was interrupted because of the existence of polymer grid; (2) the premature spalling of concrete cover negatively reduced the peak load of polymer grid confined concrete specimens; and (3) the thickness of polymer grid (2 mm for Type A polymer grid and 0.6 mm for Type B polymer grid) cannot be neglected as it reduced the effective thickness of the concrete cover, which might have adversely influenced the load carrying capacity of the specimens.

Figure 6.4 shows comparisons between Type A polymer grid confined concrete specimens and Type B polymer grid confined concrete specimens. As can be seen in Figure 6.4, Type A polymer grid performed better in improving both the strength and deformation capacity of concrete specimens than Type B polymer grid. This may be attributed to the better material properties (higher ultimate tensile strain and higher tensile elastic modulus) of Type A polymer grid compared to those of Type B polymer grid.

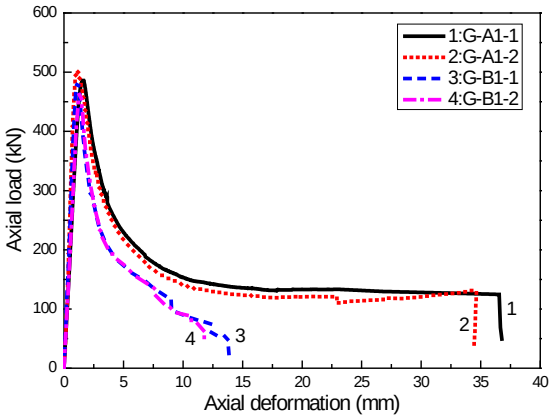

(a) Specimens G-A1-1(2) and G-B1-1(2)

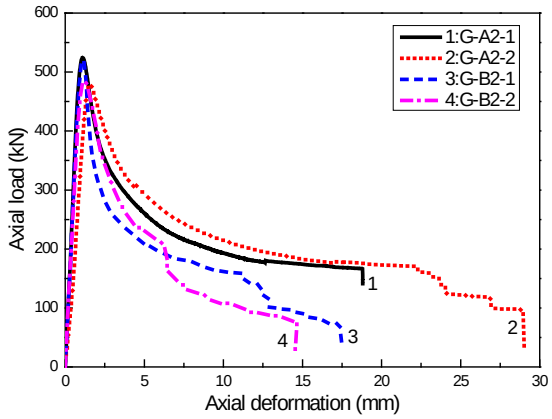

(b) Specimens G-A2-1(2) and G-B2-1(2)

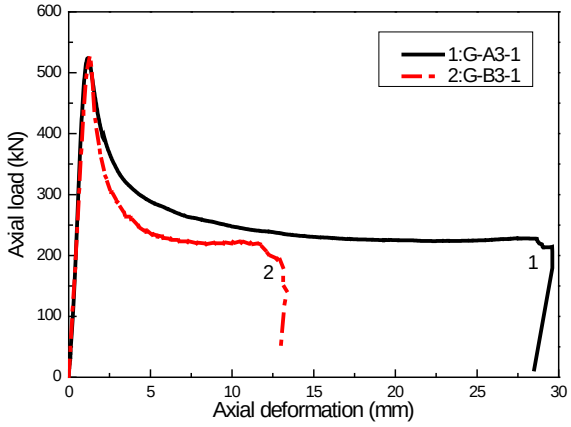

(c) Specimens G-A3-1 and G-B3-1

Figure 6.4 Comparisons between Type A and Type B polymer grid confined concrete specimens (Wang et al. 2015a)

6.3.3 Ductility and energy absorption capacity

The ductility was calculated to investigate the structural behaviour of polymer grid confined concrete. Two methods were used in this study to calculate the ductility of the specimens. In the first method, the ductility was defined as the ratio of the axial deformation at 15% drop of axial load and axial deformation at yield load. While in the second method, the ductility was defined as the ratio of the axial deformation at 50% drop of axial load and axial deformation at yield load. In this study, the definition of yield load suggested in Pessiki and Pieroni (1997) was adopted. The ductility of all concrete specimens is summarised in Table 6.2. As can be seen from Table 6.2, when the first method was used, the ductility of polymer grid confined

concrete did not show significant increase compared to that of plain concrete specimen. However, by using the second method, the ductility of polymer grid confined concrete specimen was significantly increased compared to the ductility of plain concrete specimen. Moreover, the ductility of Type A polymer grid confined concrete specimens was higher than the ductility of Type B polymer grid confined concrete specimens. Also, the ductility increases with the increase in the number of the layers of polymer grids.

The energy absorption capacity of the concrete specimen was calculated as the area under the axial load versus the axial deformation curve. For each concrete specimen, the energy absorption capacity at 15% drop in the peak axial load, at 50% drop in the peak axial load, and at failure (e.g., whole area of the axial load versus the axial deformation curve) was calculated. The energy absorbed by each specimen is shown in Table 6.2. In general, the energy absorbed by the polymer grid confined concrete and plain concrete was close to each other at 15% drop in the peak axial load. However, a significantly higher energy absorption capacity can be observed for polymer grid confined concrete than plain concrete at 50% decrease in the peak axial load and at failure. Concrete specimens confined with Type A polymer grid obtained higher energy absorption capacity than concrete specimens confined with Type B polymer grid. The energy absorption capacity can be significantly increased with the increase in the number of polymer grid layers. The highest energy absorption capacity can be observed for concrete specimens confined with three layers of Type A polymer grid.

Table 6.2 Test results in Chapter 6

Specimens	δ_y (mm)	P (kN)	δ_p (mm)	$\delta_{0.85p}$ (kN)	$\delta_{0.50p}$ (kN)	$\mu_{0.85p}$	$\mu_{0.50p}$	$W_{0.85P}$ (kN·mm)	$W_{0.50P}$ (kN·mm)	W (kN·mm)
P-1	0.882	614	1.178	1.549	2.293	1.756	2.560	241	604	1101
P-2	1.042	610	1.180	1.522	2.197	1.461	2.108	209	534	923
G-A1-1	1.209	486	1.563	2.180	4.538	1.803	3.754	272	897	6009
G-A1-2	0.930	503	1.106	1.853	3.994	1.992	4.295	268	846	5464
G-A2-1	0.857	523	1.106	1.644	4.963	1.918	5.791	239	1029	4505
G-A2-2	1.302	480	1.552	2.426	7.741	1.863	5.945	292	1447	5969
G-A3-1	0.947	524	1.177	1.712	7.587	1.808	8.012	221	1425	7837
G-A3-2	-	-	-	-	-	-	-	-	-	-
G-B1-1	0.963	482	1.130	1.514	2.937	1.572	3.050	169	564	2273
G-B1-2	1.097	467	1.355	1.692	3.044	1.542	2.775	161	545	2076
G-B2-1	0.926	521	1.109	1.414	2.948	1.527	3.184	170	585	3178
G-B2-2	0.963	485	1.198	1.913	4.334	1.987	4.501	282	893	2782
G-B3-1	1.111	525	1.265	1.550	3.763	1.395	3.387	184	720	3527
G-B3-2	-	-	-	-	-	-	-	-	-	-

Note: δ_y indicates axial deformation at yield load; P indicates peak load of concrete specimens; δ_p indicates axial deformation at peak load P; $\delta_{0.85p}$ indicates axial deformation at 85% post peak load; $\delta_{0.50p}$ indicates axial deformation at 50% post peak load; $\mu_{0.85p} = \delta_{0.85P} / \delta_y$; $\mu_{0.50p} = \delta_{0.50P} / \delta_y$; $W_{0.85P}$ indicates the absorbed energy before 85% post-peak load; $W_{0.50P}$ indicates the absorbed energy before 50% post-peak load; W indicates the whole absorbed energy before the failure of concrete specimens.

6.4 Modelling of stress-strain behaviour

Only a very limited research studies on the development of stress-strain models for predicting the axial compressive behaviour of polymer grid confined concrete is available (Saafi 2000; Michael et al. 2005; Bentayeb et al. 2008; Ding et al. 2011). The model proposed by Saafi (2000) was based on the regression analysis of the data in which all the confined concrete showed a strain-hardening response. Therefore, the model proposed by Saafi (2000) may not be appropriate to predict the stress-strain behaviour of polymer grid confined concrete with strain-softening response. Michael et al. (2005) adopted the strength model proposed for FRP confined concrete to predict the peak strength of polymer grid confined concrete. However, it is noted that due to the non-uniform nature of confinement in polymer grid confined concrete compared to that of fully FRP wrapped concrete, the stress-strain distribution of concrete core varies within the polymer grid. Therefore, it may not be suitable to directly adopt stress-strain models developed for FRP confined concrete. For the reliable use of polymer grid confined concrete, a more accurate model is required.

6.4.1 Confinement pressure and confinement modulus

For polymer grid confined concrete, only part of the concrete surface was covered with polymer grid. In order to study the confinement effect provided by the polymer grid, the equivalent thickness is used. The equivalent thickness is determined as an equivalent full coverage thickness of the transverse polymer grid. The equivalent thickness (t_{eq}) is calculated according to Equation 6.1:

$$t_{eq} = \frac{nb_g t_g}{s_g + b_g} = \frac{nA_g}{s_g + b_g} \tag{6.1}$$

where n, b_g, t_g, s_g and A_g are the number of polymer grid layers, width, thickness, spacing between transverse polymer grid, and the cross sectional area of the polymer grid, respectively.

Based on the strain compatibility condition, the effective lateral confining pressure acting on the concrete core is given by Equation 6.2:

$$f_{le} = \frac{2k_e t_{eq} f_g}{d_g} = \frac{2k_e f_g nA_g}{d_g (s_g + b_g)} \tag{6.2}$$

where f_{le} is the effective lateral confining pressure, d_g is the diameter of the concrete core, and f_g is the tensile strength of the polymer grid. k_e is the confinement effective coefficient which was proposed by Sheikh and Uzumeri (1982). The confinement effective coefficient k_e can be expressed as:

$$k_e = \frac{A_e}{A_c} = \left(1 - \frac{s_g}{2d_g}\right)^2 \tag{6.3}$$

where A_e and A_c are respectively the area of effectively confined concrete core and the cross-sectional area.

Confinement modulus significantly affects the performance of FRP confined concrete (Xiao and Wu 2000; Wu et al. 2006). Confinement modulus is defined as the ratio of the increment of confining pressure and lateral strain of concrete. For polymer grid confined concrete, the confinement modulus is calculated as:

$$C_j = -\frac{\Delta f_{le}}{\Delta \varepsilon_r} = -\frac{2k_e n A_g}{d_g(s_g + b_g)} \frac{\Delta f_g}{\Delta \varepsilon_r} \tag{6.4}$$

where C_j indicates confinement modulus, Δf_{le} indicates increments of confining pressure, $\Delta \varepsilon_r$ indicates the increments of transverse strain of concrete, and Δf_g indicates increments of tensile strength of polymer grid.

Using the deformation compatibility condition, the following equation can be established:

$$\varepsilon_r = \varepsilon_l \tag{6.5}$$

where ε_r indicates transverse strain of concrete and ε_l indicates transverse tensile strain of polymer grid.

For polymer grid with linear elasticity properties, $\Delta f_g / \Delta \varepsilon_l$ can be assumed to be equal to the tensile elastic modulus of polymer grid, E_g. Therefore, a constant confinement modulus can be defined:

$$C_j = -\frac{\Delta f_{le}}{\Delta \varepsilon_r} = -\frac{2k_e n A_g}{d_g(s_g + b_g)} E_g \tag{6.6}$$

Confinement modulus and confinement strength are related according to Equation 6.7:

$$f_{le} = -C_j \varepsilon_l \qquad 6.7$$

where the negative sign represents passive confinement.

6.4.2 Test database

The available experimental results are only a few (Saafi 2000; Michael et al. 2005; Wu et al. 2007; Bentayeb et al. 2008; Ding et al. 2011). In the present study, a database containing the test results of 32 concrete specimens were compiled. These 32 concrete specimens were reported in Saafi (2000), Michael et al. (2005), and Wu et al. (2007). All the specimens were circular in shape. In order to eliminate the influence of steel reinforcement, specimens with internal steel reinforcement were excluded. Among these specimens, 20 specimens experienced strain-hardening response, and 12 specimens experienced strain-softening response. Details of the test data are reported in Table 6.3. The parameters collected in the database include: specimen height H, diameter of concrete core d_g, unconfined concrete strength $f_{co}^{'}$, elastic modulus of concrete E_c, axial strain corresponding to unconfined concrete strength $\varepsilon_{co}^{'}$, elastic modulus of polymer grid E_g, tensile strength of polymer grid f_g, layers of polymer grid n, cross section area of polymer grid A_g, spacing between transverse polymer grid s_g, peak strength of polymer grid confined concrete f_{cp}, strain corresponding to peak strength ε_{cp}, strength at ultimate strain of polymer grid confined concrete f_{cu}, and ultimate strain of polymer grid confined concrete ε_{cu}. In this study, the ultimate strain is defined as the axial strain at the rupture of polymer grid. The database presented in this section is used to develop a new model for polymer grid confined concrete.

Table 6.3 Database compiled from previous studies

Source	Specimen	H (mm)	d_g (mm)	$f_{co}^{'}$ (MPa)	E_c (GPa)	ε_{co} (%)	E_g (GPa)	f_g (MPa)	n	A_g (mm^2)	s_g (mm)	Strain-hardening		Strain-softening			
												f_{cp} (MPa)	ε_{cp} (%)	f_{cp} (MPa)	ε_{cp} (%)	f_{cu} (MPa)	ε_{cu} (%)
Saafi (2000)	G1	421	192.4	35	30	0.15	43.0	930	1	36	25.4	61	1.6	-	-	-	-
Saafi (2000)	G2	421	192.4	35	30	0.15	43.0	930	1	36	38.1	54	1.2	-	-	-	-
Saafi (2000)	G3	421	192.4	35	30	0.15	43.0	930	1	36	54.4	49	1.1	-	-	-	-
Saafi (2000)	C1	421	192.4	35	30	0.15	225.0	1700	1	36	25.4	83	1.1	-	-	-	-
Saafi (2000)	C2	421	192.4	35	30	0.15	225.0	1700	1	36	38.1	66	0.8	-	-	-	-
Saafi (2000)	C3	421	192.4	35	30	0.15	225.0	1700	1	36	54.4	57	0.7	-	-	-	-
Michael et al. (2005)	Grid 1	304	133.4	47.8	-	-	64.5	695.5	2	6.88	45.7	-	-	58.8	0.28	-	-
Michael et al. (2005)	Grid 2	304	133.4	47.8	-	-	64.5	695.5	2	6.88	45.7	-	-	46.6	0.20	-	-
Michael et al. (2005)	Grid 3	304	133.4	47.8	-	-	64.5	695.5	2	6.88	45.7	-	-	56.8	0.26	-	-

Table 6.3 Continued

Michael et al. (2005)	Grid 4	304	139.7	47.8	-	-	64.5	695.5	2	6.88	45.7	-	-	49.6	0.28	-	-
Michael et al. (2005)	Grid 5	304	139.7	47.8	-	-	64.5	695.5	2	6.88	45.7	-	-	51.8	0.26	-	-
Michael et al. (2005)	Grid 6	304	139.7	47.8	-	-	64.5	695.5	2	6.88	45.7	-	-	53.7	0.28	-	-
Wu et al. (2007)	CR3-30-1	300	150	25.1	-	0.38	100.0	1400	1	4.4	30	27.8	1.134	-	-	-	-
Wu et al. (2007)	CR3-50	300	150	25.1	-	0.38	100.0	1400	1	4.4	50	-	-	27.4	0.46	23.3	0.97
Wu et al. (2007)	CR3-60	300	150	25.1	-	0.38	100.0	1400	1	4.4	60	-	-	26.2	0.40	22.3	0.93
Wu et al. (2007)	CR3-30-2	300	150	25.1	-	0.38	100.0	1400	2	4.4	30	37.2	1.4933	-	-	-	-

Note: H indicates specimen height; d_g indicates diameter of concrete core; $f_{co}^{'}$ indicates unconfined concrete strength; E_c indicates elastic modulus of concrete; ε_{co} indicates peak strain corresponding to unconfined concrete strength; E_g indicates elastic modulus of polymer grid; f_g indicates tensile strength of polymer grid; n indicates layers of polymer grid; A_g indicates cross section area of polymer grid; s_g indicates

spacing between transverse polymer grid; f_{cp} indicates peak strength of polymer grid confined concrete; ε_{cp} indicates peak strain of polymer grid confined concrete; f_{cu} indicates strength of grid confined concrete at ultimate strain; ε_{cu} indicates ultimate strain of polymer grid confined concrete at rupture of polymer grid.

6.4.3 Strain-hardening and strain-softening response

Stress–strain behaviour of polymer grid confined concrete includes either a strain-hardening response or a strain-softening response. Wu et al. (2006) as well as Lam and Teng (2003) suggested that strain-hardening or strain-softening response of FRP confined concrete depends mainly on confinement ratio $f_{le} / f_{co}^{'}$. Therefore, strain-hardening response or strain-softening response of polymer grid confined concrete was assumed to depend mainly on the confinement ratio $f_{le} / f_{co}^{'}$. Based on this assumption, a total of 28 data points were used to establish the relationship between the confinement ratio $f_{le} / f_{co}^{'}$ and λ ($= f_{cu} / f_{co}^{'}$), as shown in Figure 6.5 (a). A linear relationship can be established:

$$\lambda = 0.47 + 3.73 \frac{f_{le}}{f_{co}^{'}} \qquad 6.8$$

A boundary value of confinement ratio 0.142 between strain-hardening and strain-softening response can be determined from Equation 6.8. The boundary values between strain-hardening and strain-softening response for FRP confined concrete suggested by Wu et al. (2006), Lam and Teng (2003), and ACI 440.2R-08 (ACI 440.2R 2008) are 0.13, 0.07, and 0.08, respectively. All the above values for FRP confined concrete are less than that of polymer grid confined concrete.

In addition to confinement ratio $f_{le} / f_{co}^{'}$, the confinement stiffness ratio ρ_k, has been used in this study to evaluate the boundary value of adequate confinement. The confinement stiffness ratio ρ_k can be expressed as follows:

$$\rho_k = \frac{2 k_e E_g t_{eg}}{\left(f_{co}^{'} / \varepsilon_{co}\right) d_g} \qquad 6.9$$

The confinement stiffness ratio (ρ_k) represents the stiffness of polymer grid relative to the stiffness of concrete core. A total of 28 data points were used to establish the relationship between ρ_k and λ ($= f_{cu} / f_{co}^{'}$), as shown in Figure 6.5 (b). A linear relationship can be established:

$$\lambda = 0.44 + 32.24 \rho_k \qquad 6.10$$

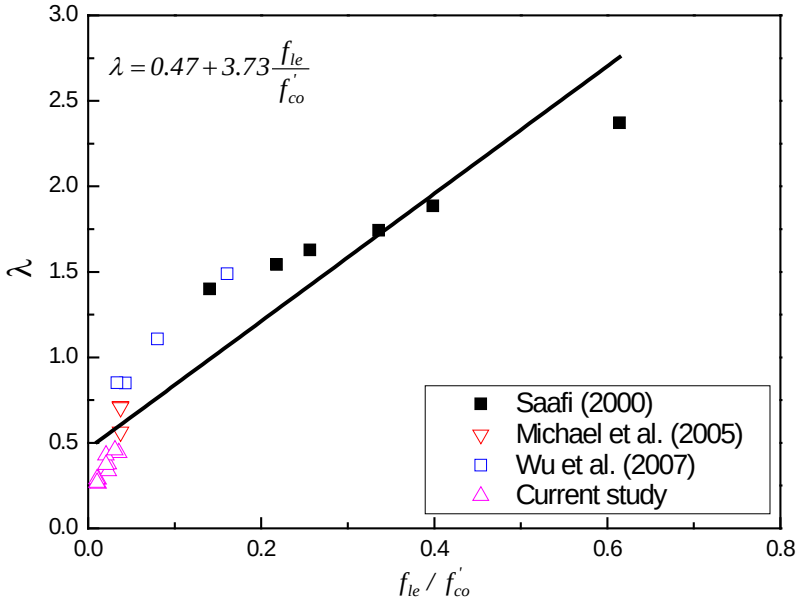

(a) Confinement ratio f_{le} / f'_{co} versus $\lambda (= f_{cu} / f'_{co})$

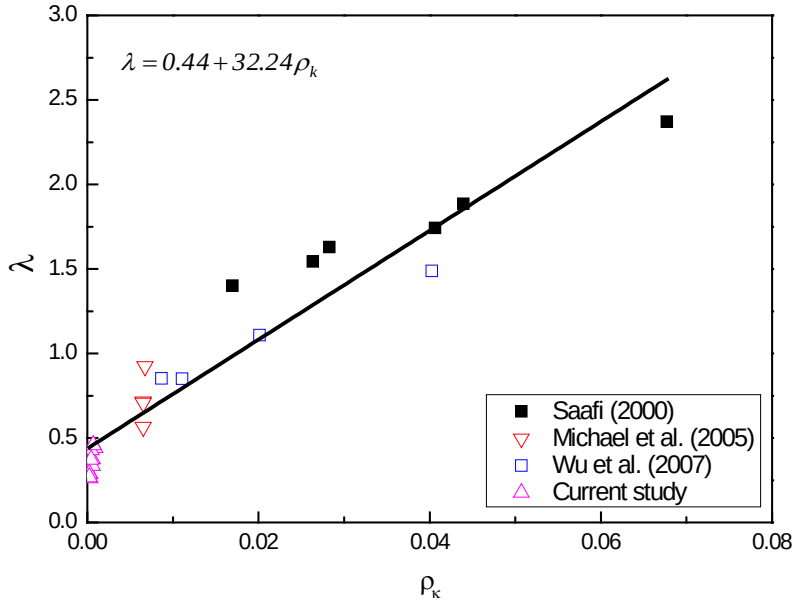

(b) Confinement stiffness ratio ρ_k versus $\lambda (= f_{cu} / f'_{co})$

Figure 6.5 Boundary value between strain-hardening and strain-softening response (Wang et al. 2015a)

The minimum ρ_k for adequate confinement of polymer grid confined concrete is 0.017. According to Teng et al. (2009), the minimum ρ_k for FRP confined concrete is 0.01. Rousakis (2013) also suggested that a minimum ρ_k of 0.01 is required for concrete columns confined with polypropylene fibre ropes (PPFRs). Based on the above discussions, it is apparent that for polymer grid confined concrete with strain-

hardening response, both the minimum confinement ratio $f_{le} / f_{co}^{'}$ and minimum confinement stiffness ratio ρ_k are higher than those of FRP confined concrete. Therefore, it is reasonable to expect that under the same $f_{le} / f_{co}^{'}$ or ρ_k , the confinement effectiveness would be less for polymer grid confined concrete than that of FRP confined concrete.

Since a strain-softening response is more likely to occur, more attention was paid on the polymer grid confined concrete with strain-softening response in this study. Therefore, the stress-strain model of polymer grid confined concrete with strain-hardening response was not considered for further analysis.

6.4.4 Peak strength and axial strain at peak strength

For polymer grid confined concrete with a strain-softening response, the peak strength reaches before the rupture of the polymer grid. This indicates that the tensile strength of polymer grid is not fully utilised when the peak strength is reached. Therefore, the peak strength of polymer grid confined concrete with a strain-softening response is independent of confinement ratio $f_{le} / f_{co}^{'}$. Wu et al. (2006) suggested that the ratio of confinement modulus to the concrete elastic modulus would significantly affect the peak strength and corresponding strain of FRP confined concrete with strain-softening response. Similarly, based on the analysis of existing experimental results, it is concluded that the peak strength and corresponding strain of polymer grid confined concrete are mainly dependent on the ratio of confinement modulus and elastic modulus of concrete (λ_0):

$$\lambda_0 = \frac{C_j}{E_c} \tag{6.11}$$

Since the elastic modulus of concrete has a direct relationship with $\sqrt{f_{co}^{'}}$ (ACI 318 2008), the factor λ_0 can be modified to λ_1 :

$$\lambda_1 = \frac{C_j}{\sqrt{f_{co}^{'}}} \tag{6.12}$$

Figure 6.6 (a) shows the relationship between λ_1 and η ($= f_{cp} / f_{co}^{'}$). A total of 18 available data points are used. The peak strength increases with the increase of factor

λ_1. Based on the interpretation of the test results in the present database, Equation 6.13 is proposed for the peak strength of polymer grid confined concrete with strain-softening response:

$$\eta = 1 + 0.0053\lambda_1 \qquad 6.13$$

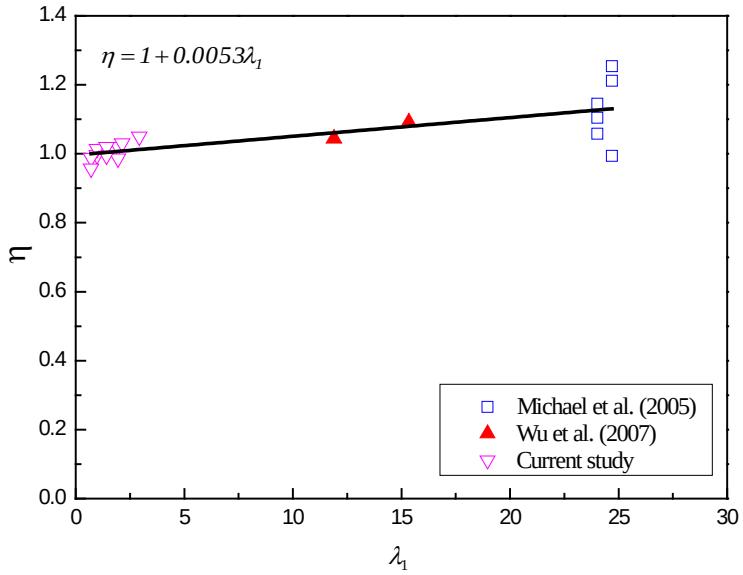

(a) Peak strength

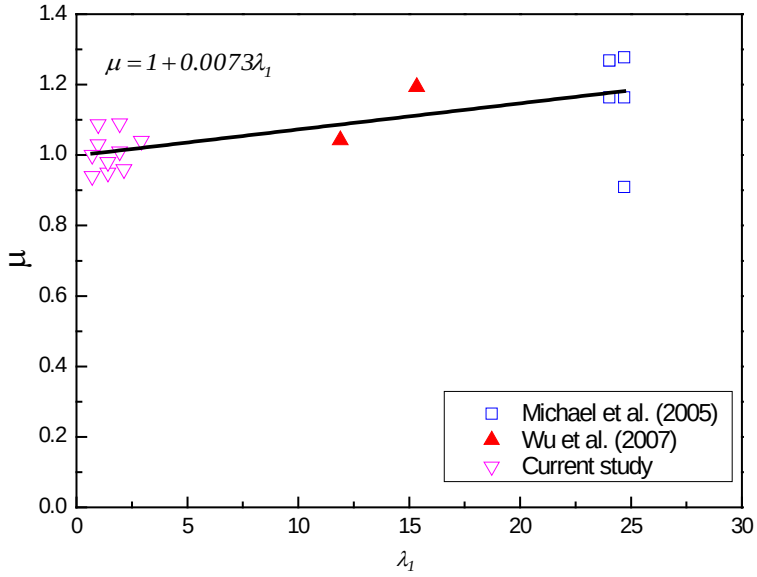

(b) Axial strain at peak strength

Figure 6.6 Prediction of peak strength and corresponding axial strain (Wang et al. 2015a)

In Figure 6.6 (a), the predictions of Equation 6.13 are compared with the present test database. Figure 6.6 (a) shows that the database are nicely scattered around the

predictions. Hence, Equation 6.13 well predicts the peak strength of polymer grid confined concrete.

Figure 6.6 (b) shows the relationship between λ_1 and μ ($=\varepsilon_{cp}/\varepsilon_{co}^{'}$). A total of 18 available data points are used. Similarly, the strain corresponding to peak strength increases with the increase of factor λ_1. Equation 6.14 is suggested to predict the peak strain of polymer grid confined concrete with strain-softening response:

$$\mu = 1 + 0.0073\lambda_1 \qquad 6.14$$

Figure 6.6 (b) shows that Equation 6.14 matches well with the present test results, which validates the accuracy of the equation.

6.4.5 Ultimate strain, and strength at ultimate strain

The ultimate state of polymer grid confined concrete is defined as the rupture of polymer grid. Hence, the strength at ultimate strain (rupture of polymer grid) depends mainly on the confinement ratio $f_{le}/f_{co}^{'}$. Equation 6.15 is proposed to predict the strength at ultimate strain for polymer grid confined concrete with a strain-softening response based on the regression analyses of 12 data points (Figure 6.7 (a)):

$$\lambda = 0.04 + 18.67\frac{f_{le}}{f_{co}^{'}} \qquad 6.15$$

where λ represents $f_{cu}/f_{co}^{'}$. It is noted that Equation 6.15 is only suitable for polymer grid confined concrete with strain-softening response. The accuracy of Equation 6.15 can be seen in Figure 6.7 (a). It can be observed that Equation 6.15 well predicts the experimental results presented in this study.

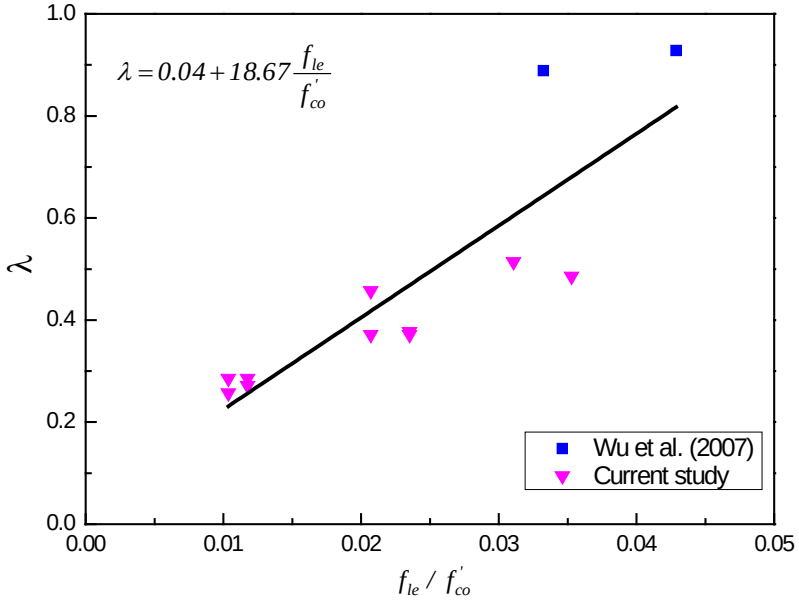

(a) Strength at ultimate strain

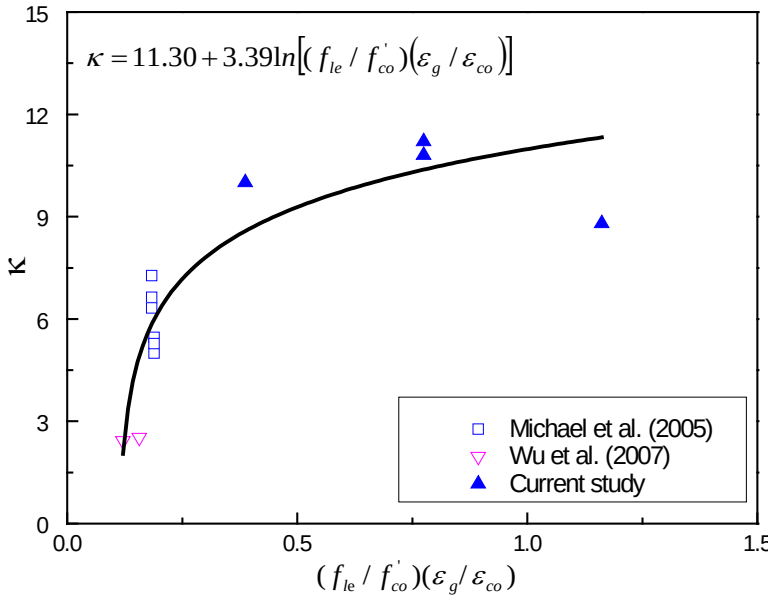

(b) Ultimate strain

Figure 6.7 Prediction of ultimate strain, and strength at ultimate strain (Wang et al. 2015a)

As for the ultimate strain, it is reasonable to assume that the ultimate stain depends mainly not only on the confinement ratio $f_{le} / f_{co}^{'}$, but also on the ratio between the ultimate strain of polymer grid and unconfined concrete strain $\varepsilon_g / \varepsilon_{co}^{'}$. For example, the confinement ratios $f_{le} / f_{co}^{'}$ for Specimens "Grid 4" in Michael et al. (2005), and "G-A3-1" as well as "G-B3-1" in this study are quite close to each other (0.0375,

0.0353, and 0.0311, respectively). However, the value of κ ($=\varepsilon_{cu}/\varepsilon_{co}^{'}$) for Specimen "Grid 4" is 5, which is much less than those for Specimens "A3-1" and "B3-1" (20 and 9.6, respectively). This difference is mainly attributed to the difference in the ultimate tensile strain between different polymer grids. Therefore, the ultimate tensile strain of polymer grid should also be taken into consideration. Equation 6.16 is proposed to predict the ultimate strain of polymer grid confined concrete specimens with strain-softening response:

$$\kappa = 11.30 + 3.39 ln\left[\frac{f_l}{f_{co}^{'}}\frac{\varepsilon_g}{\varepsilon_{co}^{'}}\right] \qquad 6.16$$

Figure 6.7 (b) shows the prediction of ultimate strain of polymer grid confined concrete specimens. It is apparent that Equation 6.16 can predict the ultimate strain with a reasonable accuracy.

6.4.6 Assessment of different models

Comparisons between previous models and the developed model have been presented herein. Summary of existing models has been shown in Table 6.4. It is noted that Saafi (2000) proposed two equations to predict the peak strength of concrete confined with polymer grid. Therefore, the prediction accuracy is evaluated for both equations proposed by Saafi (2000). The prediction accuracy of different models is quantified using two statistical indicators: mean square error (MSE) and average absolute error (AAE). Based on the two statistical indicators, the proposed model provides the best peak strength prediction, followed by the model proposed by Michael et al. (2005), as shown in Table 6.4. Similarly, the proposed model provides the best prediction for the strain at peak strength, followed by the model proposed by Michael et al. (2005), as shown in Table 6.4. The proposed model provides the most accurate predictions among available models, which is due to reasonably accurate interpretation of confinement mechanism and the use of a larger database for the development of the proposed model. Prediction comparisons for the strength at ultimate strain and ultimate strain have not been carried out since previous models did not provide predictions for these two parameters.

Table 6.4 Comparisons between different stress-strain models

Model	Peak strength			Axial strain at peak strength		
	Expressions	AAE (%)	MSE (%)	Expressions	AAE (%)	MSE (%)
Saafi (2000)	$f_{cp} = f_{co}^{'}(1+1.41(\frac{f_{le}}{f_{co}^{'}})^{0.57})$	12.5	3.3	$\varepsilon_{cp} = \varepsilon_{co}^{'}(1+(2+400\varepsilon_g)(\frac{f_{cp}}{f_{co}^{'}}-1))$	83.7	137.0
Saafi (2000)	$f_{cp} = f_{co}^{'}(1+1.54(\frac{f_{le}}{f_{co}^{'}})^{0.57})$	15.4	4.4	--	--	--
Ding et al. (2011)	$f_{cp} = f_{co}^{'}(1+1.09(\frac{f_{le}}{f_{co}^{'}})^{0.14})$	56.4	31.2	--	--	--
Michael et al. (2005)	$f_{cp} = f_{co}^{'}(1+2(\frac{f_{le}}{f_{co}^{'}}))$	6.3	0.6	$\varepsilon_{cp} = 1.8\frac{f_{cp}}{E_c}$	25.7	7.9
Proposed	$f_{cp} = f_{co}^{'}(1+0.0037\frac{f_{le}}{\varepsilon_g\sqrt{f_{co}^{'}}})$	3.6	0.3	$\varepsilon_{cp} = \varepsilon_{co}^{'}(1+0.005\frac{f_{le}}{\varepsilon_g\sqrt{f_{co}^{'}}})$	5.2	0.8

The proposed model considers the influences of several important factors including concrete properties, specimen size, polymer grid properties, and the amount of polymer grid. Even though satisfactory prediction results have be obtained, at present there is a lack of sufficient test data. More test data covering the influence of a wider range of parameters are needed for more accurate prediction of axial stress-axial strain behaviour of polymer grid confined concrete under axial compression. Such experimental and analytical investigations are the part of ongoing research studies by the author.

6.5 Conclusions

An experimental program has been carried out to investigate the axial compressive behaviour of concrete specimens confined with polymer grid. Based on test results from this study and the test results from previous studies, an analytical model has been developed. Therefore, the following conclusions can be drawn:

(1) All concrete specimens confined with polymer grid experience much higher deformation capacities, which is due to the excellent tensile strain capacity of polymer grid. The polymer grid cannot significantly increase the strength of concrete specimens, as the amount of confinement provided by the polymer grid is low due to its large openings as well as its lower tensile elastic modulus;
(2) Type A polypropylene fibres polymer grid is more effective in confining the concrete specimens compared to Type B polyester fibres polymer grid, which is due to better mechanical properties of Type A polymer grid. Both types of polymer grid are very cheap and available in the market;
(3) An analytical model has been developed for polymer grid confined concrete with strain-softening response under axial compression. The developed model can predict the axial compressive behaviour of polymer grid confined concrete with strain-softening response with good accuracy; and
(4) The preliminary test results presented in this study indicate that polymer grid may not be used as the primary confinement (e.g., steel ties or stirrups) of RC columns, which is mainly due to the inability of polymer grid to provide sufficient confinement. Moreover, since no longitudinal reinforcement was provided for the specimens tested in this study, the possibility of using polymer

grid to prevent the longitudinal steel bars from local buckling has not been investigated. However, the polymer grid can be placed between the primary confinement (e.g., steel ties or stirrups) and concrete surface to reduce the cover spalling and to some extent increase the strength and ductility of RC columns.

Chapter 7 concerns with the behaviour of FTRC columns under different loading conditions (concentric, eccentric, and four-point loadings). In addition to experimental investigation, an analytical incremental procedure has been developed to predict the performance of FTRC columns under various loading conditions.

7 BEHAVIOUR OF FTRC COLUMNS UNDER DIFFERENT LOADING CONDITIONS

7.1 Introduction

The behaviour of FRP tube reinforced concrete (FTRC) columns under concentric loading has been investigated in preceding chapters, while the behaviour of FTRC columns under eccentric loading and flexural loading has not been extensively investigated yet. It was revealed that the confinement of FRP to concrete is less effective for columns under eccentric loading and flexural loading (Fam et al. 2003; Yu et al. 2006; Wu and Jiang 2013). Therefore, an experimental program was conducted in this study to investigate the behaviour of FTRC members (240 mm in diameter and 800 mm in height) under different loading conditions. Furthermore, experimental and analytical interaction (*P*-*M*) diagrams were constructed to investigate the axial load and bending moment capacity of FTRC members.

7.2 Experimental program

7.2.1 Design of experiment

A total of 16 specimens with a length of 800 mm and a diameter of 240 mm were cast and tested under concentric, eccentric (25 mm and 50 mm), and four-point loadings. The specimens were divided into four groups with four specimens in each group. The first group (Group REF) was a reference group in which the four specimens were reinforced with steel helices and longitudinal steel bars (Figure 7.1 (a), (d)). The reinforcement consisted of 6N12 bars (12 mm deformed bars with a nominal tensile strength of 500 MPa) as longitudinal reinforcement and R10 bars (10 mm plain bars with a nominal tensile strength of 250 MPa) as transverse reinforcement in the form of helix with a pitch of 50 mm. The reinforcement ratio of specimens in Group REF was 1.5%. The second group (Group IT) contained four FRP tube reinforced concrete (FTRC) specimens which were reinforced with intact glass fibre-reinforced polymer (GFRP) tubes (Figure 7.1 (b), (e)). The GFRP tubes had an inner diameter of 167 mm with a thickness of 8 mm. The third group (Group ITG) contained four FTRC specimens reinforced with intact GFRP tubes. Moreover, two layers of polymer grid were embedded into the outer concrete (Figure 7.1 (c), (f)). The fourth group (Group PT) contained four FTRC specimens which were reinforced with perforated GFRP tubes (Figure 7.1 (b), (e)). The reinforcement ratio

of FTRC specimens in Groups IT, ITG, and PT was 9.7%. For the specimens in each group, the first specimen was subjected to concentric loading, while the second and the third specimens were subjected to eccentric loadings with 25 and 50 mm eccentricities, respectively. The fourth specimen was tested as a beam under four-point loading to evaluate the flexural behaviour. Table 7.1 shows the test matrix of the experiment. The notation of the specimens consists of two parts: the first part is REF, IT, ITG, or PT, which indicates the groups of the specimens. The second part is 0, 25, 50, or F, which indicates the loading conditions (0 indicates concentric loading; 25 indicates eccentric loading with 25 mm eccentricity; 50 indicates eccentric loading with 50 mm eccentricity; and F indicates four-point loading).

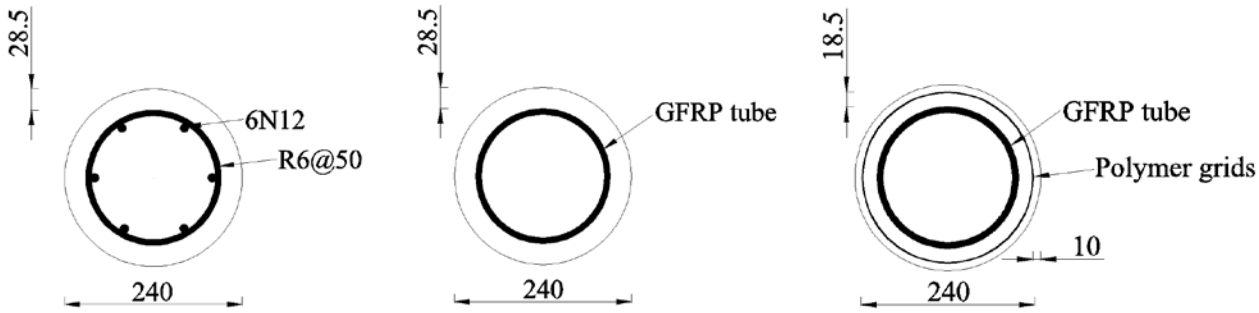

(a) Group REF (b) Group IT, PT (c) Group ITG

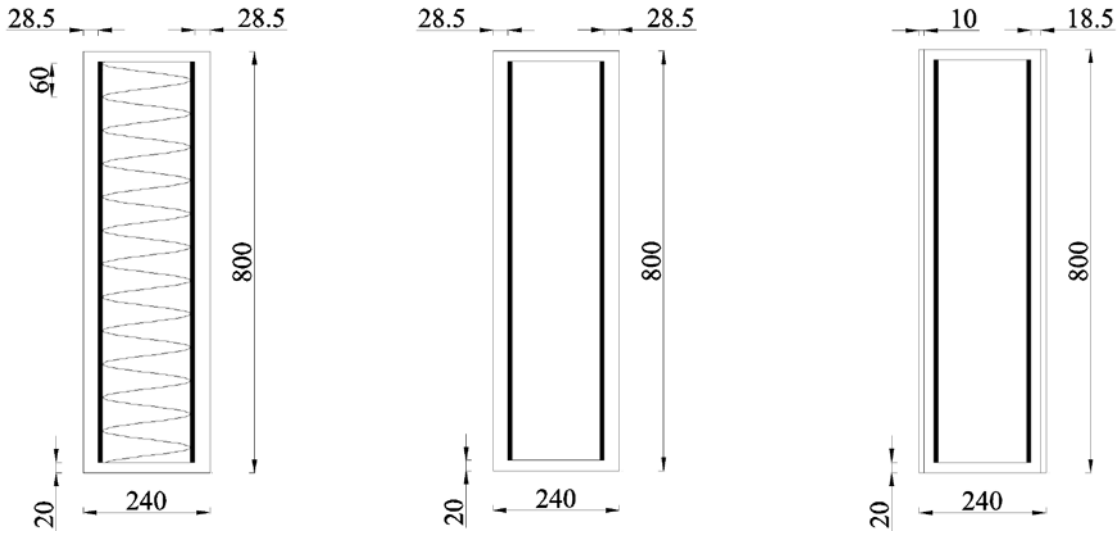

(d) Group REF (e) Group IT, PT (f) Group ITG

Figure 7.1 Details of test specimens

Table 7.1 Main test matrix

Specimen	Internal Reinforcement	Outer Confinement	Test Modes
REF-0	6N12 and R10@50 mm	--	Concentric
REF-25	6N12 and R10@50 mm	--	Eccentric, e=25 mm
REF-50	6N12 and R10@50 mm	--	Eccentric, e=50 mm
REF-F	6N12 and R10@50 mm	--	Flexural
IT	Intact GFRP tube	--	Concentric
IT-25	Intact GFRP tube	--	Eccentric, e=25 mm
IT-50	Intact GFRP tube	--	Eccentric, e=50 mm
IT-F	Intact GFRP tube	--	Flexural
ITG-0	Intact GFRP tube	2 layers of polymer grids	Concentric
ITG-25	Intact GFRP tube	2 layers of polymer grids	Eccentric, e=25 mm
ITG-50	Intact GFRP tube	2 layers of polymer grids	Eccentric, e=50 mm
ITG-F	Intact GFRP tube	2 layers of polymer grids	Flexural
PT-0	Perforated GFRP tube	--	Concentric
PT-25	Perforated GFRP tube	--	Eccentric, e=25 mm
PT-50	Perforated GFRP tube	--	Eccentric, e=50 mm
PT-F	Perforated GFRP tube	--	Flexural

7.2.2 Specimen preparation

The GFRP tubes were manufactured by Exel Composites Australia (2015) based in Boronia, Victoria, Australia. The GFRP tubes were made from vinyl ester resin

systems with E-glass fibre. The mechanical properties of GFRP tubes provided by the manufacturers are listed in Table 4.1 in Chapter 4. For the construction of perforated GFRP tubes, exact locations of the holes were marked before the perforation. Afterwards, a drill press machine with a circular drill bit was used to perforate the GFRP tubes. Three columns of holes were drilled onto each GFRP tube. The holes were symmetrically distributed along the tube circumference with a clear lateral spacing of 165 mm. 15 mm diameter circular holes were drilled. The clear vertical hole spacing was 60 mm.

The polymer grid was rectangular in shape (36 mm spacing in the longitudinal direction and 24 mm spacing in the transverse direction) and was manufactured from high modulus polyester fibres by Maccaferri Australia Pty Ltd (2015). In order to provide transverse confinement to the concrete cover, the polymer grid was formed into tubular shapes and held with plastic ties. The polymer grid was overlapped at an approximate length of 100 mm to ensure that the polymer grid would not be loosened or slid and to provide uniform confinement to the concrete cover.

The moulds for casting the specimens were made of PVC pipe with an inner diameter of 240 mm and a height of 800 mm. All the moulds were aligned vertically by a formwork made from timber. The concrete was supplied by a local concrete provider, and the nominal compressive strength was 32 MPa. Before pouring the concrete in the moulds, the steel reinforcement cages, GFRP tubes, and tubular polymer grids were placed into the moulds. After casting, all the specimens were covered with wet burlap on top to prevent moisture loss. All the specimens were kept wet during the weekdays until the test date.

7.2.3 Preliminary tests

Compressive tests of concrete cylinders on 28 days showed that the average compressive strength of the concrete was 35 MPa. The tensile properties of N12 deformed bars and R10 plain bars were tested in accordance with AS 1391 (2007) using the Instron 8033 testing machine. Based on the average results of tensile tests, the yield strength of N12 deformed bars was 440 MPa, and the yield strength of R10 plain bars was 400 MPa.

Tensile properties of the polymer grid were determined by testing polymer grid strand using Instron 8033 machine. More details can be found in Chapter 6 of this thesis. The average tensile strength of the polymer grid was 484 MPa with an elastic modulus of 5 GPa.

The GFRP tubes were tested under compression in accordance with GB/T 5350 (2005). More details can be found in Chapter 4 of this thesis. The average axial compressive strength of GFRP tube was 416 MPa with a corresponding axial strain of 0.0145. Due to the limitations of the experimental setup, the hoop tensile properties of the GFRP tubes could not be experimentally obtained. Therefore, the hoop tensile properties of the GFRP tubes provided by the manufacturers were used for further analysis.

7.2.4 Instrumentation and test procedure

The Denison 5,000 kN compression testing machine was used for testing all the specimens. For concentrically and eccentrically loaded column specimens, the specimen ends were capped with high-strength plaster to ensure uniform load distribution. In order to apply eccentric loading onto the column specimens, a set of loading heads were used (Figure 7.2). Axial deformations of the column specimens were measured using two Linear Variable Differential Transducers (LVDTs), which were mounted at the opposite corners between the bottom loading plate and the top steel plate of the Denison testing machine. In order to measure the lateral deflections for the eccentrically loaded column specimens, a laser triangulation was set up at mid-height of the column specimen. For the flexural test, a four-point loading system was manufactured, as shown in Figure 7.3. The four-point loading system was composed of a top rig and a bottom rig. The bottom rig was placed diagonally on the bottom loading plate of the Denison testing machine, and then the beam specimen was placed on the bottom rig. Afterwards, the top rig was placed on the beam specimen. The top plate of the Denison testing machine was adjusted to the top rig to apply load. A hole was drilled onto the middle of bottom rig and a laser triangulation was located underneath the bottom rig for the recording of midspan deflection of the beam specimens. All the tests were conducted as deflection controlled at a rate of 0.3 mm/min.

(a) adaptor plate

(b) steel plate with ball joint

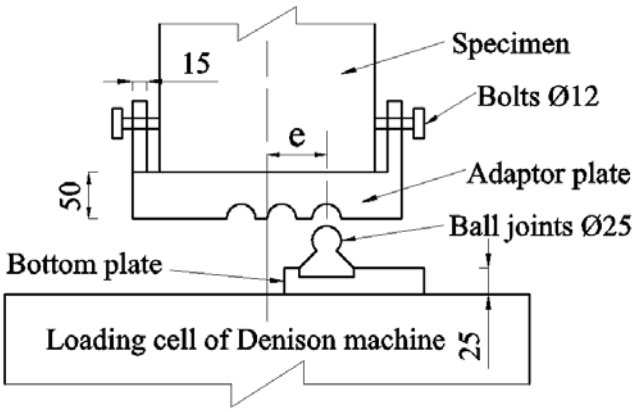

(c) loading system

Figure 7.2 Eccentric loading system (all units are in mm)

(a) bottom rig

(b) top rig

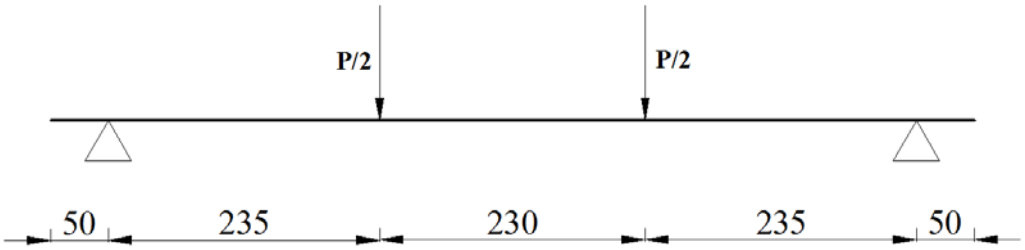

(c) Demensions of test set-up

Figure 7.3 Four-point loading system (all units are in mm)

7.3 Experimental results and discussions

7.3.1 Behaviour of specimens under concentric load

The failure modes of concentrically loaded specimens are shown in Figure 7.4. Specimen REF-0 failed gradually due to cover spalling and the buckling of longitudinal bars. Specimens IT-0 and ITG-0 failed suddenly due to the hoop rupture of GFRP tubes accompanied by a loud noise, while Specimen PT-0 failed due to the premature failure at the top end of the specimen. For Specimens REF-0 and IT-0, most of the concrete cover spalled off at the time of failure, while the spalling of concrete cover was effectively controlled by the polymer grid for Specimen ITG-0 (Figure 7.4 (c)).

(a) REF-0 (b) IT-0 (c) ITG-0 (d) PT-0

Figure 7.4 Failure modes of Specimens REF-0, IT-0, ITG-0, and PT-0

The yield load, ultimate load and the corresponding axial deformations of the specimens are shown in Table 7.2. In this study, the yield load was defined as the limit of elastic behaviour of specimens (Pessiki and Pieroni 1997): A best-fit line to the linear portion of the load–deformation curve was implemented. This line was then extrapolated to intersect with the maximum load before cover spalling. The load corresponding to this intersection was the yield load. Figure 7.5 shows the axial load-axial deformation behaviour of Specimens REF-0, IT-0, ITG-0, and PT-0. Similar behaviour has been observed before the yielding of Specimens REF-0, IT-0, and ITG-0. After the initial ascending branch, all specimens experienced load reductions due to the spalling of concrete cover. A continuous decrease of axial load was observed for Specimen REF-0. While for Specimens IT-0 and ITG-0, the axial load began to increase again since the confinement provided by the GFPR tube to the

concrete core was activated as well as the increased axial load carried by the GFRP tube. Even though higher ultimate loads can be observed for Specimens IT-0 and ITG-0, the axial deformations at ultimate loads were significantly less than that of Specimen REF-0. This phenomenon was attributed to the low hoop tensile properties of GFRP tubes. Therefore, Specimens IT-0 and ITG-0 failed due to the hoop tensile rupture of GFRP tubes before the axial compressive strength of GFRP tubes can be fully utilized. Similar behaviour was also observed by Fam and Rizkalla (2001a) and Bank (2013). Moreover, by comparing the axial load-axial deformation behaviour of Specimens IT-0 and ITG-0, it can be observed that there is no significant increase in load carrying capacity or deformation capacity due to the embedment of polymer grid into the concrete cover of Specimen ITG-0. This is because the confinement provided by the polymer grid to the concrete cover was weak due to its large openings as well as its lower tensile strength and tensile elastic modulus (Wang et al. 2015a).

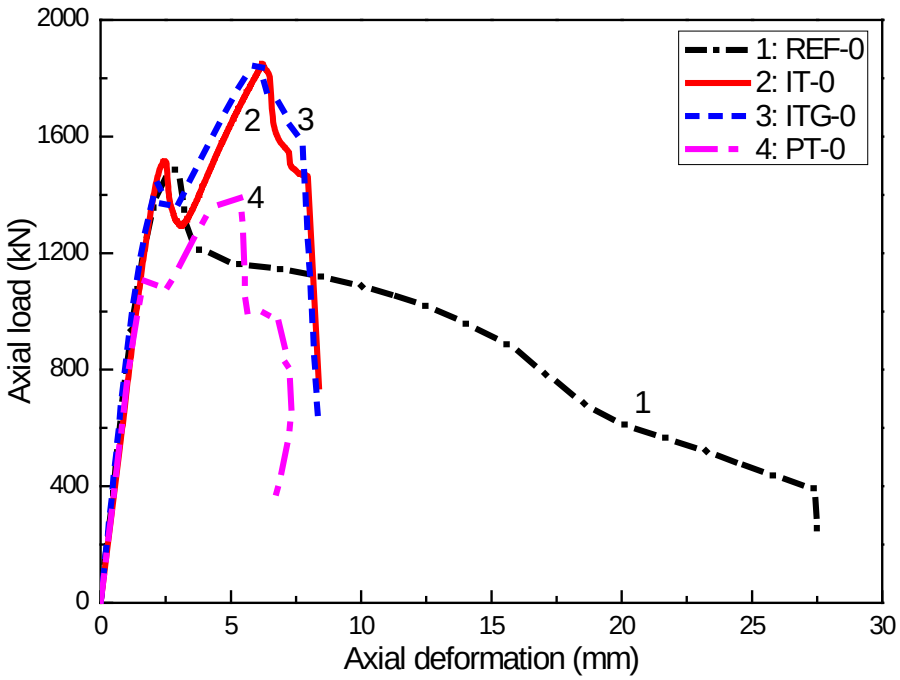

Figure 7.5 Axial load-axial deformation behaviour of specimens under concentric load

The confinement ratio (the ratio between the lateral confining pressure f_l and the unconfined concrete strength $f_{co}^{'}$) was used to investigate the strength improvement

of concrete. For Group REF specimens, the confinement ratio was calculated (Mander et al. 1988):

$$\frac{f_l}{f_{co}^{'}} = \frac{2k_e A_{ts} f_{yh}}{d_s s f_{co}^{'}} \tag{7.1}$$

where $k_e = (1 - s'/2d_s)/(1 - \rho_{cc})$ is the confinement effectiveness coefficient, A_{ts} is the area of transverse bars, f_{yh} is the yield strength of the transverse bars, s is the centre to centre spacing of neighbouring helices, s' is the clear spacing between neighbouring helices, d_s is the diameter of steel helices between bar centres, and ρ_{cc} is the ratio of total area of longitudinal reinforcement to the area of concrete core.

For Group IT and ITG specimens, the confinement ratio was calculated (Teng et al. 2009):

$$\frac{f_l}{f_{co}^{'}} = \frac{2t_f f_{t,t}}{D_{core} f_{co}^{'}} \tag{7.2}$$

where t_f is the tube thickness, $f_{t,t}$ is the hoop tensile strength of FRP tube, and D_{core} is the diameter of concrete core.

Table 7.2 Results of specimens tested under concentric and eccentric loadings

Specimen	Yield load (kN)	Axial deformation at yield load (mm)	Ultimate load (kN)	Axial deformation at ultimate load (mm)	Lateral deflection at ultimate load (mm)	Ductility
REF-0	1275	1.82	1486	2.83	--	1.87
IT-0	1405	2.05	1850	6.21	--	3.03
ITG-0	1271	1.70	1849	6.04	--	3.55
PT-0	1052	1.55	1415	5.26	--	3.39
REF-25	899	1.94	986	2.40	1.38	1.44
IT-25	1038	2.19	1474	6.70	5.14	3.06
ITG-25	1054	2.09	1558	7.06	4.95	3.38
PT-25	1002	2.24	1400	6.10	4.19	2.72
REF-50	653	2.02	696	2.45	2.32	1.47
IT-50	675	1.82	1038	9.36	7.31	5.14
ITG-50	680	2.09	1046	8.84	6.71	4.23
PT-50	686	1.92	915	9.64	5.69	2.96

The confinement ratio for specimens in Group REF was 0.16, and the confinement ratio for specimens in Groups IT and ITG was 0.137. For specimens in Group PT, the confinement ratio could not be obtained because the confinement provided by the perforated FRP tube was non-uniform and was difficult to be determined. Even though the confinement ratios were close to each other, the ultimate load of Specimen REF-0 was significantly less than those of Specimens IT-0 and ITG-0. This phenomenon was mainly attributed to that the load carried by FRP tube was significantly higher than the load carried by the longitudinal bars at ultimate load. According to the readings from strain gauges, Specimens IT-0 and ITG-0 failed at longitudinal compressive strains of 0.00645 and 0.00659, respectively. Therefore, the axial load carried by the FRP tube was calculated to be 808.5 kN and 825.0 kN, respectively ($P_f = E_{f,l}\varepsilon_{l,rup}A_f$, where $E_{f,l}$ is the longitudinal compressive elastic modulus of FRP tube, $\varepsilon_{l,rup}$ is the longitudinal compressive strain of FRP tube at failure, and A_f is the cross section area of FRP tube). However, the maximum axial load carried by longitudinal bars was calculated to be 298.6 kN ($P_{steel} = f_{yl}A_{ls}$, where f_{yl} and A_{ls} are the yield strength and the total area of longitudinal bars, respectively), and this load would further decrease because of the buckling of longitudinal bars after the spalling of concrete cover. Therefore, the ultimate load of REF-0 was significantly lower than those of Specimens IT-0 and ITG-0 even though the confinement ratios were similar.

For Specimens IT-0 and ITG-0, the increased load carried by the concrete core due to the FRP confinement was calculated ($P_u - P_f - f'_{co}A_{core}$, where P_u is the ultimate load of FTRC columns, and A_{core} is the area of concrete core). The increased loads carried by concrete core were 285.0 kN and 267.6 kN for Specimens IT-0 and ITG-0, respectively. Therefore, it can be seen that for Specimens IT-0 and ITG-0, the load contribution from the longitudinal compressive properties of FRP tube was more significant than the gain from the confinement of concrete.

7.3.2 Behaviour of specimens under eccentric load

The failure modes of Specimens REF-25, IT-25, ITG-25, and PT-25 are shown in Figure 7.6. Specimen REF-25 failed due to the crushing of concrete and local buckling of longitudinal bars in the compression region. Specimens IT-25, ITG-25, and PT-25 failed due to the rupture of GFRP tubes in the compression region with a loud noise, and no rupture was observed onto the GFRP tubes in the tension region.

(a) REF-25 (b) IT-25 (c) ITG-25 (d) PT-25

Figure 7.6 Failure modes of Specimens REF-25, IT-25, ITG-25, and PT-25

The behaviour of Specimens REF-25, IT-25, ITG-25, and PT-25 under eccentric loading is shown in Figure 7.7. For Specimen REF-25, the axial load decreased continuously after the initial ascending branch. While for FTRC specimens, the axial loads began to increase again after the initial load reductions, which was mainly attributed to that the axial load carried by GFRP tube was continuously increased. The axial stiffness of GFRP tube k_f was calculated to be 173.6 GPa·mm ($k_f = E_{f,l} A_f / L$, where $E_{f,l}$, A_f, and L are the longitudinal compressive elastic modulus, cross section area, and length of FRP tube, respectively), and the axial stiffness of longitudinal bars k_s can be calculated to be 178.6 GPa·mm ($k_s = E_s A_{ls} / L$, where E_s, A_{ls}, and L are the elastic modulus, total cross section area, and length of longitudinal bars, respectively). Even though the axial stiffness of FRP tube and longitudinal bars were close to each other, the longitudinal bars began to buckle after the spalling of concrete cover. Hence, the load carried by longitudinal bars was decreased. However, no buckling was observed for FRP tube, and the load carried by the FRP tube increased continuously with the increased of axial

deformation. Therefore, higher ultimate loads can be observed for FTRC specimens. Specimen ITG-25 obtained the highest ultimate axial load, followed by Specimens IT-25, PT-25, and REF-25. The performance difference between Specimens ITG-25 and IT-25 was not significant, which indicates that the polymer grid was not effective in increasing the load carrying capacity and deformation capacity of the specimens. For Specimen PT-25, the ultimate load was significantly lower than those of Specimens ITG-25 and IT-25 because the perforation caused strength reduction of the GFRP tube. Table 7.2 summarizes the test results of Specimens REF-25, IT-25, ITG-25, and PT-25. The yield loads of Specimens IT-25, ITG-25, and PT-25 were slightly higher than that of Specimen REF-25. The increases of the ultimate loads for Specimens IT-25, ITG-25, and PT-25 compared to the ultimate load of REF-25 were 49.5%, 58.0%, and 42.0%, respectively.

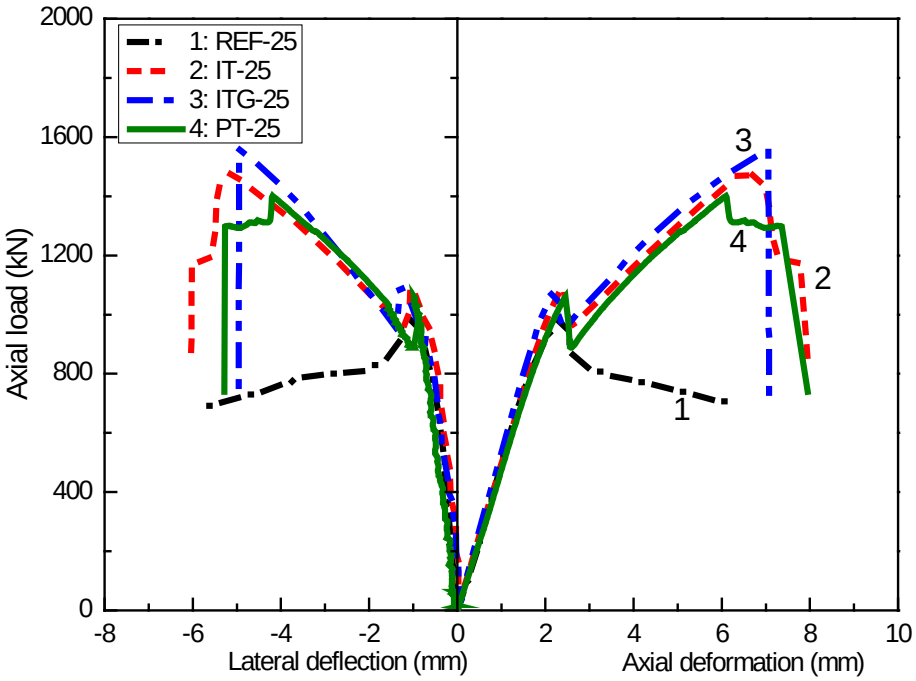

Figure 7.7 Axial load-axial deformation and axial load-lateral deflection behaviour of specimens under eccentric load (eccentricity, e=25 mm)

The behaviour of Specimens REF-50, IT-50, ITG-50, and PT-50 under eccentric loading is shown in Figure 7.8. Similar failure modes can be observed between specimens under 50 mm eccentric loading and specimens under 25 mm eccentric loading. The test results are summarized in Table 7.2. The increases of the ultimate loads of Specimens IT-50, ITG-50, and PT-50 compared to that of REF-50 were

49.1%, 50.3%, and 31.5%, respectively. The ultimate load of Specimen PT-50 was significantly less than that of Specimens IT-50 and ITG-50, which was due to the influence of perforation onto the GFRP tube.

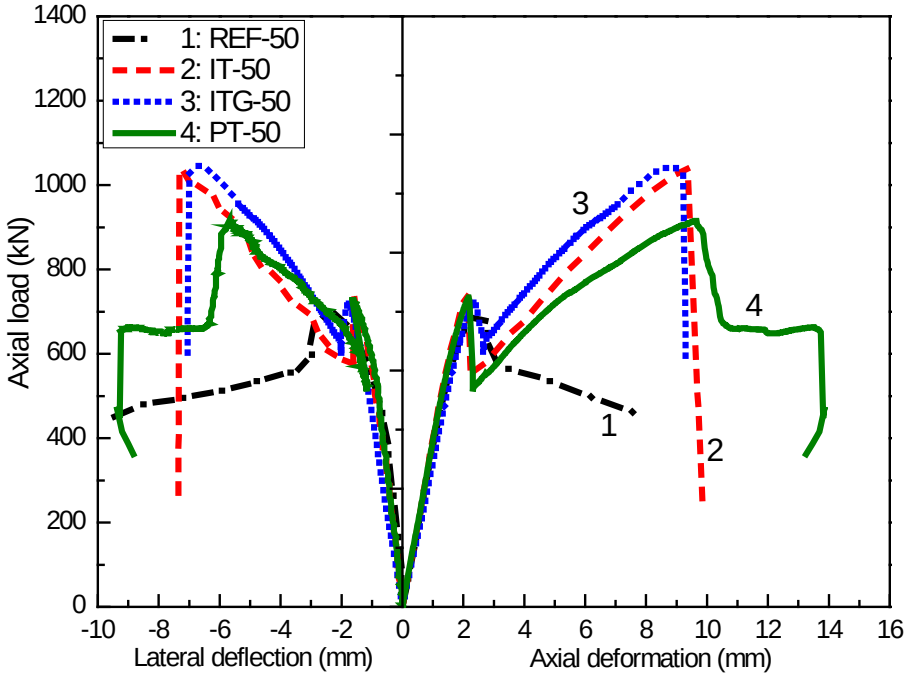

Figure 7.8 Axial load-axial deformation and axial load-lateral deflection behaviour of specimens under eccentric load (eccentricity, e=50 mm)

Moreover, it can be observed from Table 7.2 that for eccentrically loaded FTRC specimens, the axial deformations at ultimate loads were higher than the corresponding axial deformations for concentrically loaded FTRC specimens, and the axial deformations at ultimate loads increased with the increase of eccentricity. This can be explained by the fact that with the increase of eccentricity, the expansion of concrete core was less due to the existence of strain gradient. Therefore, the transverse tensile rupture of GFRP tube may occur with a higher axial strain. Moreover, it is observed that the lateral deflections of eccentrically loaded FTRC specimens were less than those of the corresponding axial deformations, which may be attributed to the high bending stiffness of FRP tubes ($E_{fl}I$, where E_{fl} is the longitudinal compressive elastic modulus of FRP tube, and I is the second moment of area). In this study, the bending stiffness of FRP tube can be calculated by $\pi D_o^4\left(1-\alpha^4\right)E_{fl}/64$, where α is the ratio between the inner diameter and outer

diameter of FRP tube, and D_o is the outer diameter of FRP tube. The bending stiffness of FRP tube was calculated to be 495469 Pa·m^4. Therefore, the FRP tubes can be effective in resisting the lateral deflections of eccentrically loaded FTRC specimens.

7.3.3 Flexural behaviour

The failure modes of beam specimens after test are shown in Figure 7.9. For Specimens IT-F, ITG-F, and PT-F, the failures were caused by the rupture of the GFRP tubes in the tension sides. Specimen REF-F failed due to the combination of flexural cracks and inclined shear cracks. This observation suggested that FRP tube was more effective in controlling the development of shear cracks (Mandal and Fam 2006). Almost all the concrete cover of Specimens IT-F and PT-F spalled off at the time of failure. Nevertheless, the failure mode of Specimen ITG-F indicates that the polymer grid can be effective in preventing the spalling of concrete cover.

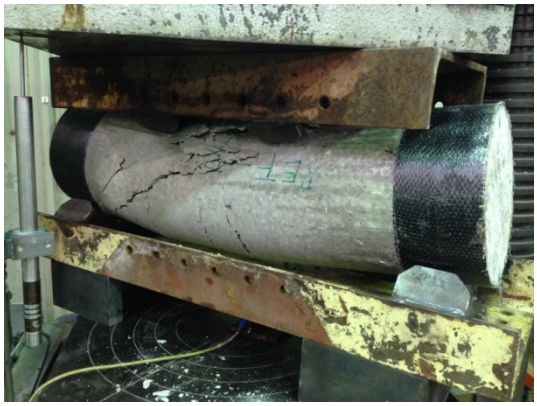

(a) REF-F

(b) IT-F

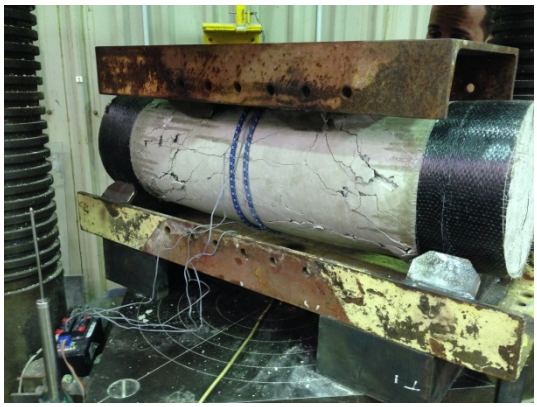

(c) ITG-F

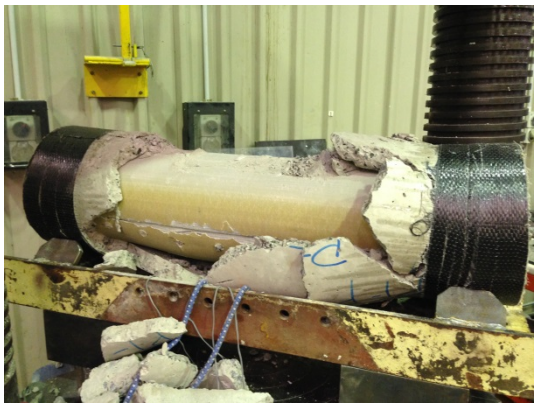

(d) PT-F

Figure 7.9 Failure modes of beam specimens

The test results of beam specimens are presented in Table 7.3. Figure 7.10 shows the load-midspan deflection behaviour of the tested specimens under four-point loading. At the initial stage, similar load-midspan deflection behaviour can be observed. Afterwards, load reductions can be observed for all specimens because of the spalling of the concrete cover. After these load reductions, the loads of all tested specimens fluctuated, which resulted in a redistribution and rearrangement of the forces within the specimens. For Specimen REF-F, a higher load was obtained even after the spalling of the concrete cover.

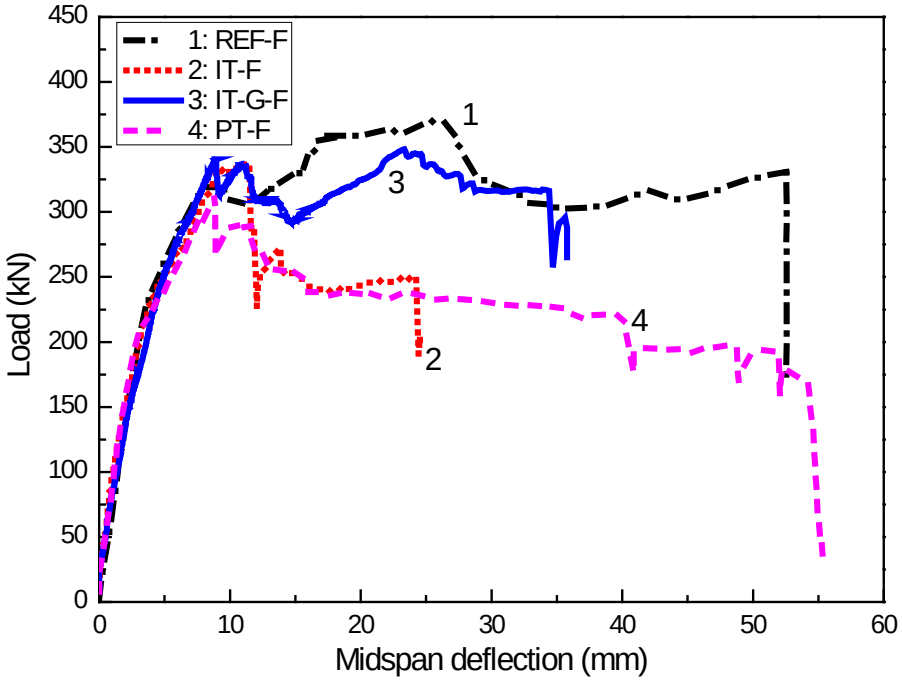

Figure 7.10 Load-midspan deflection behaviour of specimens under four-point loading

In order to obtain the theoretical bending moment capacity of Specimen REF-F with pure flexural failure, a rectangular stress block method suggested in AS 3600 (2009) was used. The theoretical bending moment capacity was found to be 27.5 kN·m, which was less than the experimental value (43.4 kN·m), as shown in Table 7.3. There might be two reasons for such behaviour: (1) Specimen REF-F failed due to the combined effect of flexural cracks and inclined shear cracks. Therefore, direct diagonal compression strut was developed in the concrete through the arching action, which resulted in an increase in the performance of concrete beam (Mohamed and Masmoudi 2010b; Pham et al. 2013); and (2) the confinement provided by the steel

helix is more effective than that provided by rectangular or square stirrups, which resulted in a higher bending moment capacity (Hadi and Schmidt 2002). For Specimens IT-F and PT-F, the FRP tube ruptured immediately after the spalling of concrete cover (the longitudinal compressive strains of FRP tube at rupture in the extreme compression fibre were 0.0025 and 0.0016, respectively), which resulted in sudden load reductions of the specimens. Therefore, the maximum load P_u was the same with the maximum load before cover spalling P_y, and hence the bending moment M_y (bending moment at P_y) was equal to M_u (bending moment at P_u). After these load reductions (from 337 kN to 227 kN for Specimen IT-F and from 311 kN to 266 kN for Specimen PT-F), Specimens IT-F and PT-F could still carry substantial amount of loads with increasing midspan deflection until failure. For Specimen ITG-F, the FRP tube ruptured at a longitudinal compressive strain of around 0.0045 in the extreme compression fibre. Therefore, Specimen ITG-F could be further loaded to obtain higher load and higher midspan deflection after the spalling of concrete cover.

Table 7.3 Results of specimens tested under four-point loading

Specimen	Maximum load before cover spalling P_y (kN)	Corresponding midspan deflection δ_y (mm)	Corresponding bending moment M_y (kN·m)	Maximum load P_u (kN)	Corresponding midspan deflection δ_u (mm)	Corresponding bending moment M_u (kN·m)
REF-F	322	8.48	37.8	369	25.56	43.4
IT-F	337	11.39	39.6	337	11.39	39.6
ITG-F	340	8.92	40.0	348	23.33	40.9
PT-F	311	8.86	36.5	311	8.86	36.5

Table 7.4 Analytical results of specimens IT-F and ITG-F

Specimen	M_y (kN·m)	$M_{y,CFFTs}$ (kN·m)	$M_{y,cover}$ (kN·m)	M_u (kN·m)	$M_{u,CFFTs}$ (kN·m)	$M_{u,cover}$ (kN·m)
IT-F	33.9	20.0	13.9	33.9	20.0	13.9
ITG-F	33.1	18.7	14.3	37.5	29.8	7.7

Note: M_y indicates the bending moment at the maximum load before cover spalling; $M_{y,CFFTs}$ and $M_{y,cover}$ indicates the bending moment carried by the inner CFFTs and concrete cover at the maximum load before cover spalling, respectively; M_u indicates the bending moment at the

maximum load; $M_{u,CFFTs}$ and $M_{u,cover}$ indicates the bending moment carried by the inner CFFTs and concrete cover at the maximum load, respectively.

7.3.4 Ductility capacity

The ductility of steel RC column can be calculated as the ratio of the axial deformation at the 85% post-ultimate load divided by the axial deformation at the yield load. However, the above definition of ductility was not applicable for FTRC columns. In this study, the ductility definition suggested by Cui and Sheikh (2010) was adopted to calculate the ductility of FTRC columns. According to Cui and Sheikh (2010), the ultimate load was defined as the load at the failure of FRP, while the same definition of yield load suggested by Pessiki and Pieroni (1997) was adopted.

The ductility of all column specimens is summarized in Table 7.2. It can be seen that FTRC columns obtained higher ductility than steel RC columns under both concentric and eccentric loadings, and the ductility of FTRC columns increase with the increase of eccentricity. It is noted that for Specimen REF-0, a considerable amount of axial deformation can still be observed after 85% post-ultimate load. Moreover, when the applied load changes from concentric loading to eccentric loadings of 25 mm and 50 mm, the decrease of axial loads of Group REF columns was 34.0% and 53.3%, respectively. The corresponding decreases in axial loads were 21% and 44%, respectively, for Group IT columns. While for Group ITG columns, the load decreases were 16% and 44%, respectively. For specimens under eccentric loading, the percentages of load reductions were less for FTRC columns than steel RC columns. Therefore, the FTRC columns are preferred to the steel RC columns especially under eccentric loadings.

7.4 Interaction diagram

Axial load-bending moment (*P-M*) interaction diagrams were constructed to investigate the axial load and bending moment capacity of the specimens. For eccentrically loaded specimens, the bending moment capacities considering the secondary moment were calculated by Equation 7.3:

$$M = P_u(e + \delta) \tag{7.3}$$

where P_u indicates ultimate axial load, e indicates loading eccentricity, and δ indicates lateral deflection at the ultimate load.

For beam specimens, the bending moment capacities were calculated by Equation 7.4:

$$M = \frac{P_u}{2} \cdot a \qquad 7.4$$

where P_u indicates ultimate load, and a is length of shear span (a =230 mm), as shown in Figure 7.3(c).

The experimental interaction diagrams are shown in Figure 7.11. The interaction diagrams indicate that FTRC specimens (Groups IT, ITG, and PT) outperformed the steel RC specimens in this study. The interaction diagrams of FTRC specimens can be divided into two parts. In the first part, the axial load increased with the increase of bending moment. While in the second part, the axial load increased with the decrease of bending moment. The interaction diagram of steel RC specimens (Group REF) was not as expected since the axial load increased with a continuous decrease of bending moment. This phenomenon was because Specimen REF-F failed due to a combination of flexural cracks and shear cracks (Figure 7.9 (a)). The shear cracks resulted in an arch action, which increased the bending moment capacity.

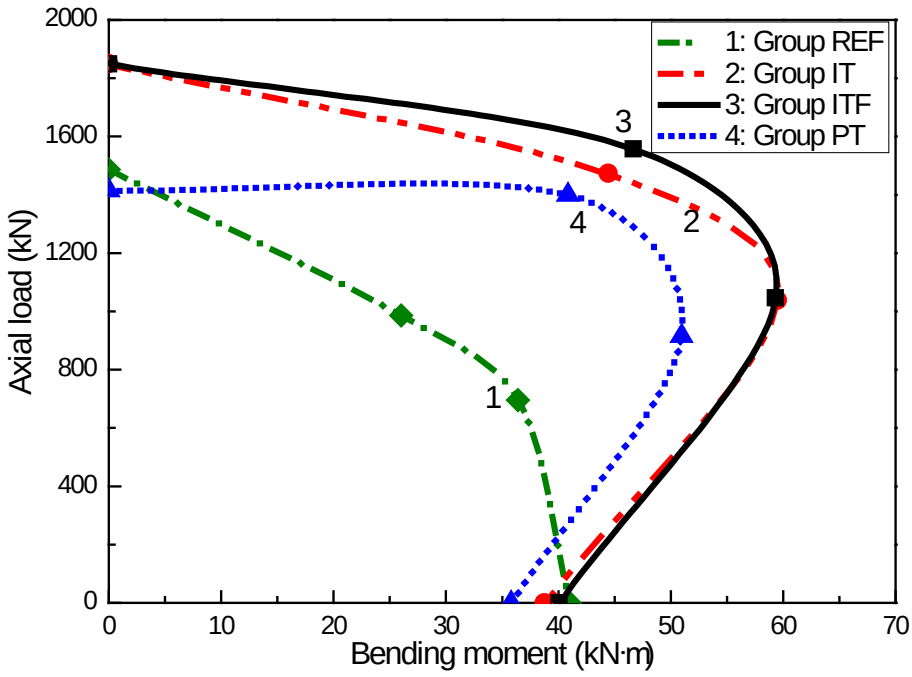

Figure 7.11 Experimental interaction (*P*-*M*) diagram

A numerical layer-by-layer approach was used to construct the analytical interaction diagrams of FTRC specimens (Fam et al. 2003; Yazici and Hadi 2009). The cross section of FTRC specimens was divided into finite small horizontal strips, as shown in Figure 7.12. In each layer, the area of FRP tube, concrete core, and concrete cover were calculated. With the plain section assumption, the strain in each strip was estimated and the axial stress of each component was calculated by the stress-strain models of different components. The calculated stresses are then integrated over the whole cross section area to obtain the resultant force and the resultant moment. In order to get more accurate prediction results, the width of these strips should be small enough. In this study, the width of these small strips was taken as 1 mm.

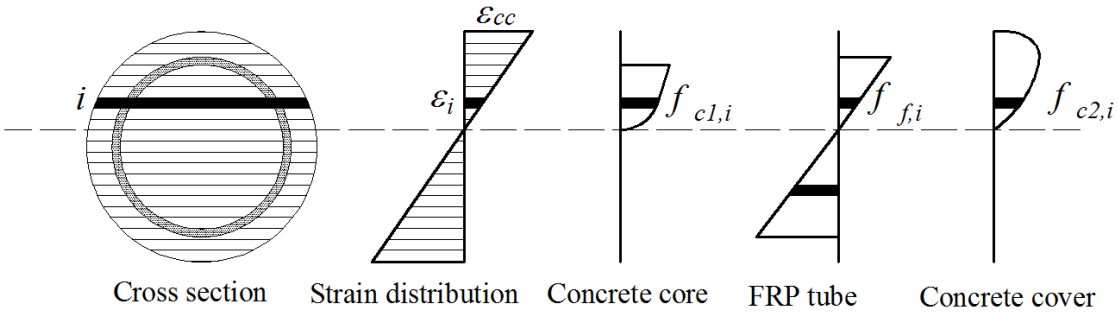

Figure 7.12 Strain and stress distribution of FTRC columns

A linear elastic stress-strain relationship was adopted in both longitudinal and transverse directions of FRP tubes. Different stress-strain models were adopted for the concrete core and concrete cover of FTRC specimens. It was observed that the confinement effect provided by polymer grid was insignificant. Therefore, the confinement effect of polymer grid was neglected in this analysis. The stress-strain model proposed by Popovics (1973) was adopted to simulate the concrete cover of FTRC specimens. Detailed descriptions of the stress-strain model proposed by Popovics (1973) can be found in Chapter 5 of this thesis. The stress-strain model proposed by Teng et al. (2009) was adopted for the concrete core of FTRC specimens subjected to concentric compression, and detailed descriptions of this model can be found in Chapter 2 of this thesis.

Moreover, in order to consider the reduced effectiveness of FRP confinement for concrete core subjected to eccentric loading and flexural loading, a variable confinement model was adopted to describe the stress-strain relationship of concrete

core under eccentric loading and flexural loading (Yu et al. 2010b; GB 50608 2012). This model is actually an extension of Teng et al. (2009) model. The only difference is the value of the slope of the second linear portion of the concrete stress-strain curve. For concrete under eccentric loading and flexural loading, the slope of the second linear portion of the stress-strain curve was calculated as:

$$E_{2ec} = E_2 \frac{D_o}{D_o + e} \tag{7.5}$$

where E_{2ec} is the slope of the second linear portion of the concrete stress-strain curve of FRP confined concrete under eccentric compression, E_2 is the slope of the linear second portion of the stress-strain curve of FRP confined concrete under concentric compression, D_o is the outer diameter of the CFFTs, and e is the eccentricity.

The above stress-strain models were adopted for the calculation of the interaction diagrams of FTRC specimens. The tensile stress carried by the concrete was neglected, and the actual longitudinal compressive strains at the extreme compression fibre of FRP tubes were used as the ultimate compressive strains. Figure 7.13 compares the experimental and analytical interaction diagrams of specimens in Groups IT and ITG. It can be seen that the analytical results are in good agreement with experimental results. The predication results underestimated the bending moment capacities of FTRC specimens subjected to both eccentric loading and flexural loading conditions. However, the predicated load carrying capacities fit well with the experimental values of FTRC specimens.

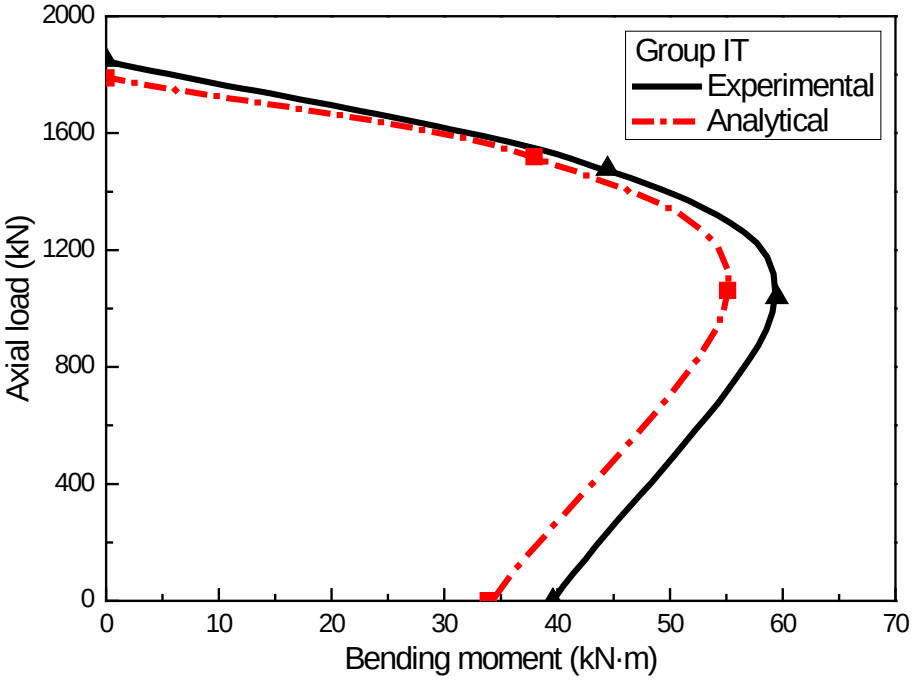

(a) *P-M* diagrams of Group IT specimens

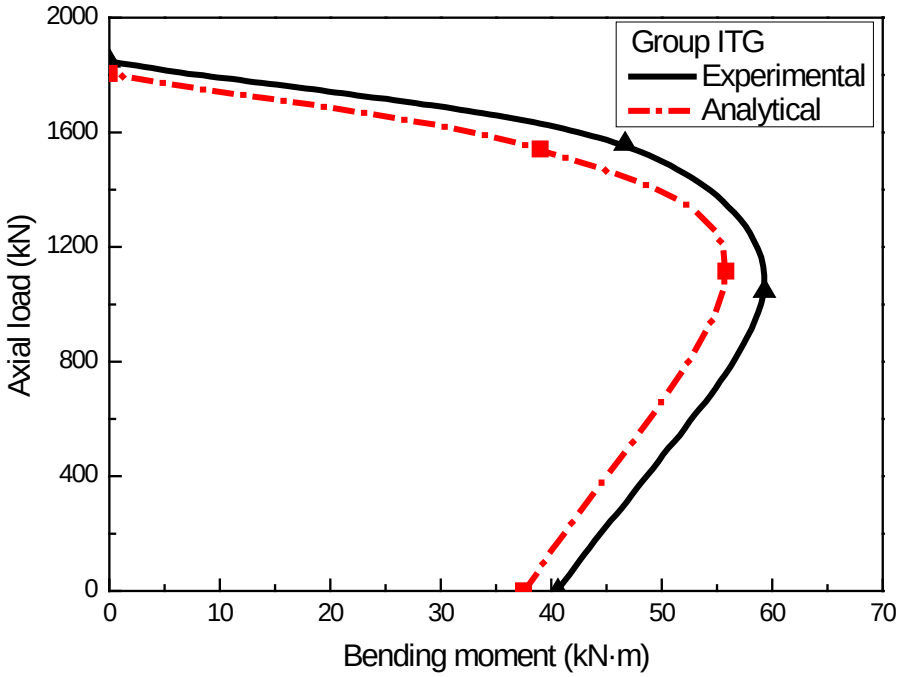

(b) *P-M* diagrams of Group ITG specimens

Figure 7.13 Comparison between analytical and experimental interaction *(P-M)* diagrams

For Specimens IT-F and ITG-F, the bending moment carried by each component (inner CFFTs and concrete cover) was investigated, as shown in Table 7.4. At the maximum load before cover spalling, the bending moment carried by concrete cover $M_{y,cover}$ was 14.3 kN·m for Specimen ITG-F, which was 43% of the bending moment

M_y (33.1 kN·m). However, at the maximum load, the bending moment carried by the concrete cover $M_{u,cover}$ was reduced to 7.7 kN·m, which was only 20% of the bending moment M_u. Even though the bending moment carried by the concrete cover was significantly reduced with the increase of longitudinal compressive strains, the bending moment carried by the inner CFFTs $M_{u,CFFTs}$ was increased (from 18.7 kN·m to 29.8 kN·m for Specimen ITG-F). Moreover, the increase in the bending moment carried by inner CFFTs was higher than the decrease in the bending moment carried by concrete cover. Therefore, a higher bending moment capacity M_u can be obtained for Specimens ITG-F after the spalling of concrete cover. In addition, the midspan deflection of Specimen ITG-F was predicted by using the proposed analytical model. Firstly, the moment-curvature response was calculated. Afterwards, the midspan deflection was calculated by using the moment-area method, as suggested in Mandal and Fam (2006). The ultimate midspan deflection for Specimen ITG-F was calculated to be 17.2 mm, which was close to the experimental value (23.3 mm). Therefore, the proposed model can also predict the midspan deflection of FTRC specimens with reasonable accuracy.

7.5 Conclusions

In this chapter, experimental and analytical investigations were carried out to study the behaviour of FRP tube reinforced concrete (FTRC) columns under different loading conditions. Based on these results, the following conclusions can be drawn:

(1) The axial load carrying capacities of FTRC specimens (Group IT, ITG, and PT) are higher than that of Group REF specimens under both concentric and eccentric loadings. The axial load carrying capacity of FTRC specimens is significantly reduced with the increase of eccentricity. Group ITG specimens achieved the highest load carrying capacities, followed by Groups IT, PT, and REF specimens;
(2) The ductility of FTRC specimens is higher than the ductility of Group REF specimens under both concentric and eccentric loading conditions. The ductility of FTRC specimens increases with the increase of load eccentricity;
(3) Among the four beam specimens (REF-F, IT-F, ITG-F, and PT-F), Specimen REF-F has the highest load carrying capacity, followed by Specimens ITG-F, IT-

F, and PT-F. The highest mid-span deflection is obtained by Specimen REF-F, followed by Specimens PT-F, ITG-F, and IT-F;

(4) Both experimental and analytical interaction diagrams of FTRC specimens are constructed. The analytical investigation can predict the load carrying capacity and bending moment capacity of FTRC specimens with good accuracy. It has been observed that a higher bending moment capacity may be obtained for FTRC specimens even after the spalling of concrete cover due to the increased bending moment carried by the inner CFFTs of FTRC specimens; and

(5) The above conclusions are based on the experimental investigations on 16 concrete specimens. Hence, more experimental investigations need to be conducted to fully validate the observed behaviour of FTRC specimens under different loading conditions. Moreover, the performance of FTRC specimens under harsh environments (e.g., aggressive freeze-thaw cycles in cold regions and extreme temperature conditions) need to be extensively investigated.

In Chapter 8, conclusions of this thesis are drawn. Moreover, recommendations for further research are also presented.

8 CONCLUSIONS

8.1 Introduction

This thesis has presented a systematic study into the basic structural behaviour of newly proposed FRP tube reinforced concrete (FTRC) columns. A large amount of experimental and analytical work has been presented in this thesis, which mainly aimed to investigate the following aspects: (1) use of perforated FRP tube in FTRC column (Type I FTRC column); (2) use of intact FRP tube and polymer grid in FTRC column (Type II FTRC column); and (3) the behaviour of both types of FTRC columns under different loading conditions.

8.2 Type I FTRC column

Chapters 3 and 4 presented the first part of the research program which was concerned with Type I FTRC column.

Chapter 3 presented an experimental study on the behaviour of Type I FTRC columns under axial compression. The FRP tube configurations (intact tube, axially perforated tube, and diagonally perforated tube) were the main test variables. In addition, numerical simulations have been carried out to assess the influence of tube perforations on the axial compressive behaviour of Type I FTRC columns. Based on the experimental and numerical results, the following conclusions can be drawn:

(1) Both intact and perforated FRP tubes are effective in improving the strength and the ductility capacity of Type I FTRC columns;
(2) Perforated GFRP tubes have been found to be effective in integrating concrete core with concrete cover. Moreover, axially perforated tubes have been found more effective than diagonally perforated tubes in increasing the strength and ductility of Type I FTRC columns; and
(3) The numerical simulations show that by reducing the hole diameter or increasing the vertical hole spacing, the performance of Type I FTRC columns can be significantly improved. Moreover, reduction of hole diameter is more effective than increase of vertical hole spacing.

For the better understanding of Type I FTRC columns reinforced with perforated FRP tubes, the axial compressive behaviour of perforated FRP tubes needs to be extensively investigated. Chapter 4 thus presented an experimental investigation on the influences of various parameters on the behaviour of perforated GFRP tubes under axial compression. The influences of hole diameter, vertical hole spacing, tube diameter, perforation pattern, transverse hole spacing, and hole reinforcement on the axial compressive behaviour of perforated GFRP tubes were experimentally investigated. In addition, design-oriented equations for the prediction of the axial stiffness, axial critical load and axial deformation capacity of perforated GFRP tubes under axial compression have been proposed. The following conclusions can be drawn:

(1) The hole diameter, tube diameter, perforation pattern, transverse hole spacing can significantly influence the performance of perforated GFRP tubes under axial compression. Reducing the hole diameter or increasing the tube diameter as well as transverse hole spacing can improve the performance of perforated GFRP tubes. Moreover, axially perforated tubes perform better than diagonally perforated tubes;
(2) Vertical hole spacing and hole reinforcement cannot significantly improve the performance of perforated GFRP tubes under axial compression; and
(3) The proposed design-oriented equations can predict the axial stiffness, axial critical load and axial deformation capacity of perforated GFRP tubes with satisfactory accuracies.

8.3 Type II FTRC column

Chapters 5 and 6 presented the second part of the research program which was concerned with the behaviour of Type II FTRC columns reinforced with FRP tube and polymer grid.

Chapter 5 presented the study on Type II FTRC columns under axial compression. The Type II FTRC column consists of an inner concrete-filled FRP tube, outer concrete confined with polymer grid, and concrete cover. A total of 16 specimens were cast and tested under axial compression. Specimens were divided into eight

groups, which included one group of plain concrete specimens, two groups of FRP confined concrete specimens, and five groups of FTRC specimens. For FRP confined concrete specimens, one layer and two layers of carbon FRP (CFRP) sheet were wrapped, respectively. For Type II FTRC specimens, GFRP tube was used to confine the inner concrete, and polymer grid was used to confine the outer concrete. In addition to experimental investigation, an analytical model has been developed. The following conclusions can be drawn:

(1) Considerable amount of strength and ductility can be obtained for Type II FTRC columns. The inner concrete-filled FRP tube carries most of the axial load, and the polymer grid provides confinement to the outer confined concrete and prevents the overall collapse of columns. FTRC columns can undergo a much higher axial deformation after the spalling of the concrete cover, which is beneficial for the safe design of concrete columns;
(2) By increasing the strength of inner and outer concrete, the yield load of Type II FTRC column can be increased. The ultimate axial load can be increased significantly by increasing the inner concrete strength. Nevertheless, by increasing the strength of outer concrete, the ultimate axial load cannot be significantly increased;
(3) Both the yield load and ultimate axial load can be increased by increasing the FRP tube thickness, and the increase is more significant for ultimate axial load. By changing the filament winding angles of FRP tube, the yield load, ultimate load, and ultimate axial strain of Type II FTRC columns can be varied significantly; and
(4) Since the confinement provided by the polymer grid is weak due to the large openings as well as its lower tensile properties, the polymer grid does not contribute significantly to the yield load, ultimate axial load, and ultimate axial strain of columns. Nevertheless, the polymer grid is essential to prevent the overall collapse of columns.

Chapter 6 presented a study on the behaviour of concrete confined solely with polymer grid under axial compression. Two types of polymer grid (Type A and Type B) with different mechanical properties were selected. For each type of polymer grid,

one layer, two layers, and three layers were used to investigate the influence of the amount of polymer grid confinement on the axial compressive behaviour of concrete specimens. Based on the analysis of test results in this study as well as test results from previous studies, an analytical model for polymer grid confined concrete was developed. The following conclusions can be drawn:

(1) Concrete specimens confined with polymer grid can experience considerable amount of axial deformation due to the excellent tensile strain capacity of polymer grid. However, the polymer grid does not significantly increase the strength of concrete specimens, as the amount of confinement provided by the polymer grid is low due to its large openings as well as its lower tensile elastic modulus;
(2) Type A polypropylene fibres polymer grid is more effective in confining the concrete specimens than Type B polyester fibres polymer grid;
(3) An analytical model has been developed for polymer grid confined concrete with strain-softening response under axial compression, and the predicted results matched well with the experimental results; and
(4) The polymer grid may not be able to act as the primary confinement (e.g., steel ties or stirrups) of RC columns. However, the polymer grid can be placed between the primary confinement and concrete surface to provide confinement to the outer concrete and to some extent increase the strength and ductility of columns.

8.4 FTRC columns under different loading conditions

Chapter 7 has provided an extensive investigation on the behaviour of FTRC columns under different loading conditions. Four groups of 16 specimens were cast and tested. Specimens in the first group (reference group) were reinforced with longitudinal steel bars and steel helices (Group REF). Specimens in the second group were reinforced with intact GFRP tubes (Group IT). Specimens in the third group were also reinforced with intact GFRP tubes. In addition, polymer grid was embedded into the outer concrete (Group ITG). Specimens in the fourth group were reinforced with perforated GFRP tubes (Group PT). From each group, one specimen was tested under concentric loading, one specimen under 25 mm eccentric loading,

one specimen under 50 mm eccentric loading, and one specimen under four-point loading. In addition, an incremental analytical procedure has been developed to predict the interaction diagram of FTRC columns. The following conclusions can be drawn:

(1) FTRC specimens (Group IT, ITG, and PT) can obtain higher load carrying capacities than Group REF specimens under both concentric and eccentric loadings. The load carrying capacity of FTRC specimens is significantly reduced with the increase of eccentricity. The highest load carrying capacities were observed for Group ITG specimens, followed by Groups IT, PT, and REF specimens;
(2) FTRC specimens obtain higher ductility than Group REF specimens under both concentric and eccentric loadings. The ductility of FTRC specimens increases with the increase of load eccentricity;
(3) The bending moment capacities and midspan deflections of FTRC beams are less than those of Group REF beam in this study;
(4) An incremental analytical procedure is developed to predict the interaction diagram of FTRC specimens. The analytical investigation can predict the load carrying capacity and bending moment capacity of FTRC specimens with good accuracy. Moreover, a higher bending moment capacity may be obtained for FTRC specimens even after the spalling of concrete cover due to the increased bending moment carried by the inner CFFTs of FTRC specimens.

8.5 Future research

This thesis has presented a systematic study on the basic structural behaviour of FTRC columns, which led to a good understanding of the newly proposed FTRC columns. More research studies, however, is still needed to be conducted in the future. Some of the issues that need further research are detailed below:

(1) More tests should be conducted to investigate the behaviour of FTRC columns under eccentric compressive loading and flexural loading;
(2) FTRC columns with other cross sections (i.e. non-circular sections for inner CFFTs and outer concrete component);

(3) Slenderness effect of FTRC columns;
(4) Addition of longitudinal rebars into the outer component of FTRC columns;
(5) The long-term durability of FTRC columns under harsh environments (e.g. freeze-thaw cycles and high temperature);
(6) The cyclic/seismic behavior of FTRC columns;
(7) Develop beam-column connections for FTRC system; and
(8) Propose design guidelines for the design of FTRC columns in practical application.

REFERENCES

ACI 318 (2008). "Building Code Requirements for Structural Concrete and Commentary." American Concrete Institute, Farmington Hills, MI.

ACI 440.1R (2006). "Guide for the design and construction of structural concrete reinforced with FRP bars." American Concrete Institutie, Farmington Hill, MI.

ACI 440.2R (2008). "Guide for the design and construction of externally bonded FRP systems for strengthening concrete structures." American Concrete Institute, Farmington Hills, MI.

Afifi, M. Z., Mohamed, H. M., and Benmokrane, B. (2014). "Strength and axial behavior of circular concrete columns reinforced with CFRP bars and spirals." *Journal of Composites for Construction*, 18(2).

Almroth, B. O., and Holmes, A. M. C. (1972). "Buckling of shells with cutouts, experiment and analysis." *International Journal of Solids and Structures*, 8(8), 1057-1071.

An, Y. F., and Han, L. H. (2014). "Behaviour of concrete-encased CFST columns under combined compression and bending." *Journal of Constructional Steel Research*, 101, 314-330.

An, Y. F., Han, L. H., and Roeder, C. (2014). "Flexural performance of concrete-encased concretefilled steel tubes." *Magazine of Concrete Research*, 66(5), 249-267.

An, Y. F., Han, L. H., and Zhao, X. L. (2013). "Experimental behaviour of box concrete-encased cfst eccentrically loaded column." *Magazine of Concrete Research*, 65(20), 1219-1235.

AS 1391 (2007). "Metallic materials-Tensile testing at ambient temperature." Australian Standard, Sydney, NSW, Australia.

AS 3600 (2009). "Concrete structures." Australian Standard, Sydney, NSW, Australia.

ASTM D3039/D3039M (2000). "Standard test method for tensile properties of polymer matrix composite materials." ASTM International, West Conshohocken, PA.

ASTM D695 (2002). "Standard test method for compressive properties of rigid plastics." ASTM International, West Conshohocken, PA.

ASTM D2290 (2012). "Standard test method for apparent hoop tensile strength of plastic or reinforced plastic pipe." ASTM International, West Conshohocken, PA.

ASTM D7565/D7565M (2010). "Standard test method for determining tensile properties of fibre reinforced polymer matrix composites used for strengthening of civil structures." ASTM International, West Conshohocken, PA.

Aydın, S., Yazıcı, H., and Baradan, B. (2008). "High temperature resistance of normal strength and autoclaved high strength mortars incorporated polypropylene and steel fibers." *Construction and Building Materials*, 22(4), 504-512.

Bank, L. C. (2006). *Composites for construcion: Structural Design with FRP Materials*, John Wiley & Sons, Hoboken, Newjersey.

Bank, L. C. (2013). "Progressive failure and ductility of FRP composites for construction: Review." *Journal of Composites for Construction*, 17(3), 406-419.

Becque, J., Patnaik, A. K., and Rizkalla, S. H. (2003). "Analytical models for concrete confined with FRP tubes." *Journal of Composites for Construction*, 7(1), 31-38.

Benmokrane, B., Chaallal, O., and Masmoudi, R. (1996). "Flexural response of concrete beams reinforced with FRP reinforcing bars." *ACI Structural Journal*, 93(1), 46-55.

Bentayeb, F., Ait Tahar, K., and Chateauneuf, A. (2008). "New technique for reinforcement of concrete columns confined by embedded composite grid." *Construction and Building Materials*, 22(8), 1624-1633.

Cervantes, J. A., and Palazotto, A. N. (1979). "Cutout Reinforcement of Stiffened Cylindrical Shells." *Journal of Aircraft*, 16(3), 203-208.

Chen, J. F., Li, S. Q., and Bisby, L. A. (2013). "Factors affecting the ultimate condition of FRP-wrapped concrete columns." *Journal of Composites for Construction*, 17(1), 67-78.

Chithra, R., and Thenmozhi, R. (2010). "Studies on prefabricated cage reinforced steel-concrete composite beams." *Asian Journal of Civil Engineering*, 12(1), 27-37.

Chithra, R., Thenmozhi, R., and Ravathi, M. C. (2011). "Flexural ductility of Prefabricated Cage reinforced steel - concrete composite beams." *Asian Journal of Civil Engineering*, 12(6), 719-729.

Cho, C. G., Kwon, M., and Spacone, E. (2005). "Analytical model of concrete-filled fiber-reinforced polymer tubes based on multiaxial constitutive laws." *Journal of Structural Engineering*, 131(9), 1426-1433.

Cole, B., and Fam, A. (2006). "Flexural load testing of concrete-filled FRP tubes with longitudinal steel and FRP rebar." *Journal of Composites for Construction*, 10(2), 161-171.

Cui, C., and Sheikh, S. A. (2010). "Experimental study of normal- and high-strength concrete confined with fiber-reinforced polymers." *Journal of Composites for Construction*, 14(5), 553-561.

Daniel, I. M., and Ishai, O. (1994). *Engineering Mechanics of Composite Materials*, Oxford University Press.

De Luca, A., Matta, F., and Nanni, A. (2010). "Behavior of full-scale glass fiber-reinforced polymer reinforced concrete columns under axial load." *ACI Structural Journal*, 107(5), 589-596.

Deitz, D. H., Harik, I. E., and Gesund, H. (2003). "Physical properties of glass fiber reinforced polymer rebars in compression." *Journal of Composites for Construction*, 7(4), 363-366.

Ding, L., Seliem, H. M., Rizkalla, S. H., Wu, G., and Wu, Z. (2011). "Behavior of concrete piles confined with CFRP grid." *American Concrete Institute, ACI Special Publication*, 189-205.

Exel Composites Australia (2015). "991 Mountain Highway, Boronia, Melbourne, VIC Australia. ." <http://www.exelcomposites.com.au/ >. (June, 2015).

Fam, A., Cole, B., and Mandal, S. (2007). "Composite tubes as an alternative to steel spirals for concrete members in bending and shear." *Construction and Building Materials*, 21(2), 347-355.

Fam, A., Flisak, B., and Rizkalla, S. (2003). "Experimental and analytical modeling of concrete-filled fiber-reinforced polymer tubes subjected to combined bending and axial loads." *ACI Structural Journal*, 100(4), 499-509.

Fam, A., Mandal, S., and Rizkalla, S. (2005). "Rectangular filament-wound glass fiber reinforced polymer tubes filled with concrete under flexural and axial

loading: Analytical modeling." *Journal of Composites for Construction*, 9(1), 34-43.

Fam, A., and Rizkalla, S. (2003). "Large scale testing and analysis of hybrid concrete/composite tubes for circular beam-column applications." *Construction and Building Materials*, 17(6–7), 507-516.

Fam, A. Z. (2000). "Concrete-filled fiber-reinforced polymer tubes for axial and flexural structural members." PhD thesis, The University of Manitoba, Winnipeg, Manitoba.

Fam, A. Z., and Rizkalla, S. H. (2001a). "Behavior of axially loaded concrete-filled circular fiber-reinforced polymer tubes." *ACI Structural Journal*, 98(3), 280-289.

Fam, A. Z., and Rizkalla, S. H. (2001b). "Confinement model for axially loaded concrete confined by circular fiber-reinforced polymer tubes." *ACI Structural Journal*, 98(4), 451-461.

Fam, A. Z., and Rizkalla, S. H. (2002). "Flexural behavior of concrete-filled fiber-reinforced polymer circular tubes." *Journal of Composites for Construction*, 6(2), 123-132.

Feng, P., Cheng, S., Bai, Y., and Ye, L. (2015). "Mechanical behavior of concrete-filled square steel tube with FRP-confined concrete core subjected to axial compression." *Composite Structures*, 123, 312-324.

Fisher, M. J., and Sezen, H. (2011). "Behavior of exterior reinforced concrete beam-column joints including a new reinforcement." *Structural Engineering and Mechanics*, 40(6), 867-883.

GB 50608 (2012). "Technical code for infrastructure application of FRP composites." China Architecture and Building Press, China.

GB/T 5350 (2005). "Test method for longitudinal compressive properties of fiber-reinforced thermosetting plastic pipe." Standardization Administration of China, China.

Gupta, N. K., and Gupta, S. K. (1993). "Effect of annealing, size and cut-outs on axial collapse behaviour of circular tubes." *International Journal of Mechanical Sciences*, 35(7), 597-613.

Hadi, M. N. S. (2006a). "Behaviour of FRP wrapped normal strength concrete columns under eccentric loading." *Composite Structures*, 72(4), 503-511.

Hadi, M. N. S. (2006b). "Comparative study of eccentrically loaded FRP wrapped columns." *Composite Structures*, 74(2), 127-135.

Hadi, M. N. S., Karim, H., and Sheikh, M. N. (2016). "Experimental investigations on circular concrete columns reinforced with GFRP bars and helices under different loading conditions." *Journal of Composites for Construction*, 04016009.

Hadi, M. N. S., Pham, T. M., and Lei, X. (2013). "New method of strengthening reinforced concrete square columns by circularizing and wrapping with fiber-reinforced polymer or steel straps." *Journal of Composites for Construction*, 17(2), 229-238.

Hadi, M. N. S., and Schmidt, L. C. (2002). "Use of helixes in reinforced concrete beams." *ACI Structural Journal*, 99(2), 191-198.

Hadi, M. N. S., Wang, W., and Sheikh, M. N. (2015). "Axial compressive behaviour of GFRP tube reinforced concrete columns." *Construction and Building Materials*, 81, 198-207.

Hadi, M. N. S., and Zhao, H. (2011). "Experimental study of high-strength concrete columns confined with different types of mesh under eccentric and concentric loads." *Journal of Materials in Civil Engineering*, 23(6), 823-832.

Han, L. H., and An, Y. F. (2014). "Performance of concrete-encased CFST stub columns under axial compression." *Journal of Constructional Steel Research*, 93, 62-76.

Han, L. H., An, Y. F., Roeder, C., and Ren, Q. X. (2015). "Performance of concrete-encased CFST box members under bending." *Journal of Constructional Steel Research*, 106, 138-153.

Han, L. H., Li, W., and Bjorhovde, R. (2014). "Developments and advanced applications of concrete-filled steel tubular (CFST) structures: Members." *Journal of Constructional Steel Research*, 100, 211-228.

Han, L. H., Liao, F. Y., Tao, Z., and Hong, Z. (2009). "Performance of concrete filled steel tube reinforced concrete columns subjected to cyclic bending." *Journal of Constructional Steel Research*, 65(8-9), 1607-1616.

Hinton, M. J., Kaddour, A. S., and Soden, P. D. (2002). "Evaluation of failure prediction in composite laminates: background to 'part B' of the exercise." *Composites Science and Technology*, 62(12–13), 1481-1488.

Ji, G., Li, G., Li, X., Pang, S.-S., and Jones, R. (2008). "Experimental study of FRP tube encased concrete cylinders exposed to fire." *Composite Structures*, 85(2), 149-154.

Ji, G., Ouyang, Z., and Li, G. (2009). "Experimental investigation into the interfacial shear strength of AGS-FRP tube confined concrete pile." *Engineering Structures*, 31(10), 2309-2316.

Ji, X., Kang, H., Chen, X., and Qian, J. (2014). "Seismic behavior and strength capacity of steel tube-reinforced concrete composite columns." *Earthquake Engineering and Structural Dynamics*, 43(4), 487-505.

Jiang, T., and Teng, J. G. (2007). "Analysis-oriented stress–strain models for FRP–confined concrete." *Engineering Structures*, 29(11), 2968-2986.

Jullien, J. F., and Limam, A. (1998). "Effects of openings of the buckling of cylindrical shells subjected to axial compression." *Thin-Walled Structures*, 31(1–3), 187-202.

Lam, L., and Teng, J. G. (2003). "Design-oriented stress–strain model for FRP-confined concrete." *Construction and Building Materials*, 17(6–7), 471-489.

Li, G., Torres, S., Alaywan, W., and Abadie, C. (2005). "Experimental study of FRP tube-encased concrete columns." *Journal of Composite Materials*, 39(13), 1131-1145.

Li, J., and Hadi, M. N. S. (2003). "Behaviour of externally confined high-strength concrete columns under eccentric loading." *Composite Structures*, 62(2), 145-153.

Liao, F. Y., Han, L. H., and Tao, Z. (2014). "Behaviour of composite joints with concrete encased CFST columns under cyclic loading: Experiments." *Engineering Structures*, 59, 745-764.

Lin, Y. J., Cheng, W. R., Xu, M., and Zuo, J. (2001). "Experimental study on limit values of axial compression ratios of SRC columns with circular steel tube." *China Civil Engineering Journal*, 34(6), 23-28 (In Chinese).

Maccaferri Australia Pty Ltd (2015). "22 Powers Road, Seven Hills, Sydney, NSW Australia." <http://www.maccaferri.com.au/afawcs0137304/Home.html/>. (Accessed on July, 2015).

Mandal, S., and Fam, A. (2006). "Modeling of prestressed concrete-filled circular composite tubes subjected to bending and axial loads." *Journal of Structural Engineering*, 132(3), 449-459.

Mander, J. B., Priestley, M. J., and Park, R. (1988). "Theoretical stress-strain model for confined concrete." *Journal of Structural Engineering (United States)*, 114(8), 1804-1826.

Michael, A. P., Hamilton, H. R., and Ansley, M. H. (2005). "Concrete confinement using carbon fiber reinforced polymer grid." *ACI Special Publication*, 230, 991-1010.

Mirmiran, A., and Shahawy, M. (1996). "A new concrete-filled hollow FRP composite column." *Composites Part B: Engineering*, 27(3-4), 263-268.

Mirmiran, A., and Shahawy, M. (1997). "Behavior of concrete columns confined by fiber composites." *Journal of Structural Engineering*, 123(5), 583-590.

Mirmiran, A., Shahawy, M., and Beitleman, T. (2001). "Slenderness limit for hybrid FRP-concrete columns." *Journal of Composites for Construction*, 5(1), 26-34.

Mirmiran, A., Shahawy, M., El Khoury, C., and Naguib, W. (2000). "Large beam-column tests on concrete-filled composite tubes." *ACI Structural Journal*, 97(2), 268-276.

Mirmiran, A., Shahawy, M., Samaan, M., El Echary, H., Mastrapa, J. C., and Pico, O. (1998). "Effect of column parameters on FRP-confined concrete." *Journal of Composite for Construction*, 2(4), 175-185.

Mirmiran, B. A., Shahawy, M., and Samaan, M. (1999). "Strength and ductility of hybrid frp-concrete beam-columns." *Journal of Structural Engineering*, 125(10), 1085-1093.

Mohamed, H. M., and Masmoudi, R. (2010a). "Axial load capacity of concrete-filled FRP tube columns: Experimental versus theoretical predictions." *Journal of Composites for Construction*, 14(2), 231-243.

Mohamed, H. M., and Masmoudi, R. (2010b). "Flexural strength and behavior of steel and FRP-reinforced concrete-filled FRP tube beams." *Engineering Structures*, 32(11), 3789-3800.

Mohamed, H. M., and Masmoudi, R. (2011). "Deflection prediction of steel and FRP-reinforced concrete-filled FRP tube beams." *Journal of Composites for Construction*, 15(3), 462-472.

Nanjing Hitech Composites Co., L. (2015). "Dongping Industrial Park, Lishui, Nanjing, Jiangsu Province, China." <http://www.hitechfrp.com/haituo/indexyw.asp/>. (Accessed on July, 2015).

Nanni, A., Rizkalla, S. H., Bakis, C., Conrad, J. O., and Abdelrahman, A. (1998). "Characterization of GFRP ribbed rod used for reinforced concrete construction." *Proceedings of the International Composites Exhibition*, 11-16.

Nie, J., Bai, Y., and Cai, C. S. (2008). "New connection system for confined concrete columns and beams. I: Experimental study." *Journal of Structural Engineering*, 134(12), 1787-1799.

Ozbakkaloglu, T. (2013a). "Axial Compressive behavior of square and rectangular high-strength concrete-filled FRF Tubes." *Journal of Composites for Construction*, 17(1), 151-161.

Ozbakkaloglu, T. (2013b). "Behavior of square and rectangular ultra high-strength concrete-filled FRP tubes under axial compression." *Composites Part B: Engineering*, 54(1), 97-111.

Ozbakkaloglu, T. (2013c). "Compressive behavior of concrete-filled FRP tube columns: Assessment of critical column parameters." *Engineering Structures*, 51, 188-199.

Ozbakkaloglu, T., Lim, J. C., and Vincent, T. (2013). "FRP-confined concrete in circular sections: Review and assessment of stress–strain models." *Engineering Structures*, 49, 1068-1088.

Pessiki, S., and Pieroni, A. (1997). "Axial load behavior of large-scale spirally-reinforced high-strength concrete columns." *ACI Structural Journal*, 94(3), 304-314.

Pham, T. M., Doan, L. V., and Hadi, M. N. S. (2013). "Strengthening square reinforced concrete columns by circularisation and FRP confinement." *Construction and Building Materials*, 49(0), 490-499.

Pham, T. M., and Hadi, M. N. S. (2013). "Strain estimation of CFRP-confined concrete columns using energy approach." *Journal of Composites for Construction*, 17(6), 04013001.

Polyfabric Australia Pty Ltd (2015). "5 Frost Road, Campbelltown, Sydney, NSW Australia. ." <http://www.polyfabrics.com.au/index-2.html/ >. (Accessed on July, 2015).

Popovics, S. (1973). "A numerical approach to the complete stress-strain curve of concrete." *Cement and Concrete Research*, 3(5), 583-599.

Rethnasamy, C., Rajagopal, T., and Muthuraj, H. (2013). "Bending behavior, deformability and strength analysis of Prefabricated Cage Reinforced Composite beams." *Construction and Building Materials*, 38, 482-490.

Rousakis, T. C. (2013). "Hybrid confinement of concrete by fiber-reinforced polymer sheets and fiber ropes under cyclic axial compressive loading." *Journal of Composites for Construction*, 17(5), 732-743.

Saafi, M. (2000). "Design and fabrication of FRP grids for aerospace and civil engineering applications." *Journal of Aerospace Engineering*, 13(4), 144-149.

Saafi, M., Toutanji, H. A., and Li, Z. (1999). "Behavior of concrete columns confined with fiber reinforced polymer tubes." *ACI Materials Journal*, 96(4), 500-509.

Sadeghian, P., Lai, Y. C., and Fam, A. (2011). "Testing and modeling of a new moment connection of concrete-filled FRP tubes to footings under monotonic and cyclic loadings." *Journal of Composites for Construction*, 15(4), 653-662.

Samaan, M., Mirmiran, A., and Shahawy, M. (1998). "Model of Concrete Confined by Fiber Composites." *Journal of Structural Engineering*, 124(9), 1025-1031.

Sezen, H., and Miller, E. A. (2011). "Experimental evaluation of axial behavior of strengthened circular reinforced-concrete columns." *Journal of Bridge Engineering*, 16(2), 238-247.

Sezen, H., and Shamsai, M. (2006). "Behavior of normal strength concrete columns reinforced with prefabricated cage system." *Proceedings of the Structures Congress and Exposition*, 74.

Sezen, H., and Shamsai, M. (2008). "High-strength concrete columns reinforced with prefabricated cage system." *Journal of Structural Engineering*, 134(5), 750-757.

Shamsai, M. (2006). "Prefabricated cage system for reinforcing concrete members." Ph.D. dissertation, Ohio State University, Columbus, Ohio.

Shamsai, M., and Sezen, H. (2005). "Fast and easy concrete construction using innovative steel reinforcement." *Construction Research Congress 2005: Broadening Perspectives - Proceedings of the Congress*, 635-644.

Shamsai, M., and Sezen, H. (2011). "Behavior of square concrete columns reinforced with Prefabricated Cage System." *Materials and Structures/Materiaux et Constructions*, 44(1), 89-100.

Shamsai, M., Whitlatch, E., and Sezen, H. (2007). "Economic evaluation of reinforced concrete structures with columns reinforced with prefabricated cage system." *Journal of Construction Engineering and Management*, 133(11), 864-870.

Sheikh, M. N., and Légeron, F. (2014). "Performance based seismic assessment of bridges designed according to Canadian Highway Bridge Design Code." *Canadian Journal of Civil Engineering*, 41(9), 777-787.

Sheikh, M. N., Tsang, H. H., McCarthy, T. J., and Lam, N. T. K. (2010). "Yield curvature for seismic design of circular reinforced concrete columns." *Magazine of Concrete Research*, 62(10), 741-748.

Sheikh, S., and Uzumeri, S. M. (1982). "Analytical model for concrete confinement in tied columns." *Journal of the Structural Division*, 108(ST12), 2703-2722.

Starnes, J. H. (1972). "Effect of a circular hole on the buckling of cylindrical shells loaded by axial compression." *AIAA Journal*, 10(11), 1466-1472.

Taheri-Behrooz, F., Esmaeel, R. A., and Taheri, F. (2012). "Response of perforated composite tubes subjected to axial compressive loading." *Thin-Walled Structures*, 50(1), 174-181.

Teng, J. G., Jiang, T., Lam, L., and Luo, Y. Z. (2009). "Refinement of a design-oriented stress-strain model for FRP-confined concrete." *Journal of Composites for Construction*, 13(4), 269-278.

Teng, J. G., and Lam, L. (2004). "Behavior and modeling of fiber reinforced polymer-confined concrete." *Journal of Structural Engineering*, 130(11), 1713-1723.

The Laminator. 2015. http://www.thelaminator.net/, version 3.7.

Toda, S. (1983). "Buckling of cylinders with cutouts under axial compression " *Experimental Mechanics*, 23(4), 414-417.

Tsai, S. W., and Wu, E. M. (1971). "General theory of strength for anisotropic materials " *Journal of Composite Materials*, 5, 58-80.

Vincent, T. O. a. T. (2014). "Axial Compressive Behavior of Circular High-Strength Concrete-Filled FRP Tubes." *Journal of Composite for Construction*.

Wagners CFT (2015). "339 Anzac Avenue, Toowoomba, QLD Australia." <http://www.wagnerscft.com.au/ >. (June, 2015).

Wang, W., Sheikh, M. N., and Hadi, M. N. S. (2015a). "Axial compressive behaviour of concrete confined with polymer grid." *Materials and Structures/Materiaux et Constructions*, 1-16.

Wang, W., Sheikh, M. N., and Hadi, M. N. S. (2015b). "Behaviour of perforated GFRP tubes under axial compression." *Thin-Walled Structures*, 95, 88-100.

WestSystem (2015). "http://www.westsystem.com/ss/typical-physical-properties/." (June, 2015).

Wong, Y. L., Yu, T., Teng, J. G., and Dong, S. L. (2008). "Behavior of FRP-confined concrete in annular section columns." *Composites Part B: Engineering*, 39(3), 451-466.

Wu, G., Lü, Z. T., and Wu, Z. S. (2006). "Strength and ductility of concrete cylinders confined with FRP composites." *Construction and Building Materials*, 20(3), 134-148.

Wu, G., Wu, Z. S., Luo, Y. B., and Jiang, J. B. (2007). "Aseismic performance of circular concrete columns confined with FRP grids." *Journal of Architecture and Civil Engineering*, 24(4), 39-44.

Wu, Y.-F., and Jiang, C. (2013). "Effect of load eccentricity on the stress–strain relationship of FRP-confined concrete columns." *Composite Structures*, 98, 228-241.

Xiao, Y., and Wu, H. (2000). "Compressive behavior of concrete confined by carbon fiber composite jackets." *Journal of Materials in Civil Engineering*, 12(2), 139-146.

Xie, T., and Ozbakkaloglu, T. (2015). "Behavior of steel fiber-reinforced high-strength concrete-filled FRP tube columns under axial compression." *Engineering Structures*, 90, 158-171.

Xu, L., and Liu, Y. B. (2013). "Concrete Filled Steel Tube Reinforced Concrete (CFSTRC) Columns Subjected to ISO-834 Standard Fire: Experiment." *Advances in Structural Engineering*, 16(7), 1263-1282.

Yazici, V., and Hadi, M. N. S. (2009). "Axial load-bending moment diagrams of carbon FRP wrapped hollow core reinforced concrete columns." *Journal of Composites for Construction*, 13(4), 262-268.

Yost, J. R., Gross, S. P., and Dinehart, D. W. (2001). "Shear strength of normal strength concrete beams reinforced with deformed GFRP bars." *Journal of Composites for Construction*, 5(4), 268-275.

Yu, T., Wong, Y. L., and Teng, J. G. (2010a). "Behavior of hybrid FRP-concrete-steel double-skin tubular columns subjected to eccentric compression." *Advances in Structural Engineering*, 13(5), 961-974.

Yu, T., Wong, Y. L., and Teng, J. G. (2010b). "Technical Papers: Behavior of Hybrid FRP-Concrete-Steel Double-Skin Tubular Columns Subjected to Eccentric Compression." *Advances in Structural Engineering*, 13(5), 961-974.

Yu, T., Wong, Y. L., Teng, J. G., Dong, S. L., and Lam, E. S. S. (2006). "Flexural behavior of hybrid FRP-concrete-steel double-skin tubular members." *Journal of Composites for Construction*, 10(5), 443-452.

Zhu, Z., Ahmad, I., and Mirmiran, A. (2005). "Effect of column parameters on axial compression behavior of concrete-filled FRP tubes." *Advances in Structural Engineering*, 8(4), 443-449.